



**INSTITUT FÜR
ENERGIETECHNIK UND
THERMODYNAMIK**
Institute for Energy Systems
and Thermodynamics

Master's Thesis

Performance Improvement of a High Specific Speed Mixed-Flow Pump by Means of Multi-objective Optimization

under the supervision of

Univ.Prof. Dipl.-Ing. Dr.-Ing. Christian Bauer
Projektass. Dipl.-Ing. Julian Unterluggauer, BSc
E302 - Institute of Energy Systems and Thermodynamics

submitted to the Faculty of Mechanical and Industrial Engineering
of Technische Universität Wien
for the degree of Diplom-Ingenieur (Dipl.-Ing.)

by

Franz Josef Johann Hahn, BSc
Matr.Nr. 01225338
Hauptstraße 55, A-3441 Freundorf

Freundorf, September 2018

.....
(Franz Josef Johann Hahn, BSc)

Statutory Declaration

This thesis is the result of my own work and includes nothing that is the outcome of work done in collaboration except as specified in the text.

It is not substantially the same as any that I have submitted, or, is being concurrently submitted for a degree or diploma or other qualification at Technische Universität Wien or any other University or similar institution except as specified in the text. I further state that no substantial part of my thesis has already been submitted, or, is being concurrently submitted for any such degree, diploma or other qualification at Technische Universität Wien or any other University or similar institution except as specified in the text.

Freundorf, September 2018

.....
(Franz Josef Johann Hahn, BSc)

Acknowledgements

My sincere gratitude goes to the advisor of this thesis, Univ.Prof. Dipl.-Ing. Dr.-Ing. Christian Bauer, for his guidance during the execution of the research. He not only hired me as part-time employee of his research group of the Institute for Energy Systems and Thermodynamics but also confirmed me to publish part of the findings of this thesis on the occasion of the forty year anniversary event of the conference *Vienna Hydro 2018 - 20th International Seminar on Hydropower Plants*.

I would like to offer my special thanks to Dipl.-Ing. Julian Unterluggauer. As my supervisor he introduced me to the application of CFD to hydraulic machinery and was always available to support me.

What I appreciated the most throughout executing this thesis were the countless discussions about special aspects of fluid-flow machinery with Ao.Univ.Prof. Dipl.-Ing. Dr.techn. Reinhard Willinger. They contributed to broaden my understanding of pumps and compressors.

I wish to acknowledge the help provided by Dipl.-Ing. Christoph Öttl for testing the developed optimization workflow in his project.

I would also like to thank Dr. Bernhard List, my supervisor in many internships with Voith Hydro. His fascination of hydraulic machinery encouraged me to choose this field of engineering for my master's thesis.

Most of all I would like to express my deepest gratefulness to my beloved parents, Veronika and Ing. Franz Hahn. They endured all my moods during my studies and nevertheless supported me in every possible way. God bless them.

Abstract

This thesis aims at establishing a workflow to improve the performance characteristics of a mixed-flow pump by means of multi-objective optimization. Starting from an existing model pump of former manufacturer *Riva Calzoni SpA*, the project is split into two main segments to enhance the original design to modern standards.

At first, the original pump was remodelled from ink drawings and then investigated with the help of analytical criteria and numerical simulations. The initial simulations lay in good agreement with the model test data. Throughout most of the operating range, the difference between the simulated head and efficiency and those of the model test was less than 2.5%. However, the simulations revealed massive flow separations along the diffuser vanes. Analytical criteria indicated that the maximum allowable blade loading of the vanes was clearly exceeded. In order to overcome this flaw the diffuser blades were lengthened and the hub diameter was increased. Moreover, the blade angles were adapted to the flow conditions. These measures led to an improvement of the pump efficiency by approximately 4%, a decline of swirl behind the diffuser and a reduction of the flow separation zone.

In the second part of the project emphasis was laid on additional improvements of the pump by means of optimization. Characteristic dimensions of the rotor and stator blades were chosen as design parameters. The optimization itself was conducted within the *Response Surface Optimization* module of *ANSYS Workbench 18.2*. Maximizing the pump efficiency at the design point was set as the primary objective. In order to keep computational costs at an affordable level, rotor and stator domain were optimized in two separated process cycles. The optimization resulted in a further efficiency gain of roughly 1% in the impeller but only one of 0.2% in the vaned diffuser, hence the additional optimization effort for the diffuser was not worth the computational costs.

In all, the peak efficiency of the existing model pump was increased by about 5%.

Kurzfassung

Das Ziel dieser Arbeit ist die Entwicklung eines Workflows zur Verbesserung der Leistungsdaten einer Halbaxialpumpe durch Anwendung multikriterieller Optimierung. Von einem bestehenden Modell des früheren italienischen Pumpenherstellers *Riva Calzoni SpA* ausgehend, ist diese Arbeit in zwei Schwerpunkte aufgeteilt.

Zuerst wurde die Originalpumpe anhand von Tusche-Zeichnungen nachgebildet und mittels analytischer Kriterien und CFD-Simulationen untersucht. Die Differenz zwischen den simulierten Werten von Druckzahl und Wirkungsgrad zu jenen des Modelltests betrug über weite Teile des Betriebsbereichs weniger als 2,5 %. Allerdings wurden massive Strömungsablösungen im Diffusor sichtbar, die auf eine zu große hydrodynamische Belastung der Beschaukelung zurückzuführen sind. Um dies zu kompensieren, wurden die Diffusorscheufeln verlängert, der Nabendurchmesser des Diffusors vergrößert und die Schaufelwinkel an die Strömung angepasst. Dies bewirkte eine Verbesserung des Wirkungsgrads um etwa 4 %, eine Reduktion des Restdralls stromab des Diffusors und eine Verkleinerung des Ablösegebiets.

Der zweite Teil der Arbeit befasst sich mit der Verbesserung von Rotor und Stator durch die Anwendung multikriterieller Optimierung, welche mit dem *Response Surface Optimization* Modul der *ANSYS Workbench 18.2* durchgeführt wurde. Dazu wurden charakteristische Abmessungen von Laufrad und Diffusor als Eingabegrößen vorgegeben und die Maximierung des Wirkungsgrades als Ziel der Optimierung festgelegt. Um die Rechenzeit und Lizenzkosten gering zu halten, wurden Rotor und Stator in zwei getrennten Zyklen optimiert. Diese ergaben eine weitere Wirkungsgradsteigerung von etwa 1 % im Laufrad, aber von weniger als 0,2 % im Diffuser. Der zusätzliche Aufwand für die Optimierung des Stators dieser Maschine ist daher nicht gerechtfertigt.

In Summe konnte der maximale Wirkungsgrad des bestehenden Pumpenmodells um rund 5 % erhöht werden.

Contents

1	Introduction	1
1.1	Motivation	1
1.2	Scope of work	3
2	Theory of centrifugal pump design and numerical methods	4
2.1	Fundamental principles	4
2.1.1	Energy conversion	4
2.1.2	Dimensionless quantities	8
2.1.3	Cordier diagram	10
2.2	Mixed-flow pumps	10
2.2.1	General	10
2.2.2	Performance characteristics	12
2.2.3	Applications	14
2.2.4	Acceptance tests	16
2.3	Design procedure	19
2.3.1	Reparametrization	19
2.3.2	Blade design	22
2.3.3	Meridional contour	26
2.4	Computational Fluid Dynamics	27
2.4.1	Navier-Stokes equations	27
2.4.2	Shear-Stress Transport model	28

2.4.3	Uncertainty estimation	29
2.5	Optimization	31
2.5.1	Design of Experiments	32
2.5.2	Response Surface Method	33
2.5.3	Optimization	34
3	Reference configuration	38
3.1	Model machine	38
3.2	Test rig	39
3.3	Model test data	40
4	Simulation setup	42
4.1	Computational domain	42
4.2	Boundary conditions and numerical scheme	44
4.3	Validation	46
5	Flow in the vaned diffuser	49
5.1	Assessment of the original diffuser	49
5.2	Design modifications	53
5.2.1	Leading edge	53
5.2.2	Axial length	54
5.2.3	Trailing edge	54
5.3	Suitable designs	55
5.3.1	Overview of design variants	55
5.3.2	Comparison of the reference configuration to the most suitable design	57
6	Optimization	64
6.1	Methodology	64
6.1.1	Workflow	64
6.1.2	Settings for the CFD loop	67

6.1.3	Settings for the optimization loop	67
6.2	Rotor optimization cycle	68
6.2.1	Parametrization	68
6.2.2	Objectives	70
6.2.3	Results	71
6.3	Stator optimization cycle	75
6.3.1	Parametrization	75
6.3.2	Objectives	76
6.3.3	Results	76
6.4	Performance characteristics	79
7	Conclusion	81
7.1	Outcome	81
7.2	Further research	82
	Bibliography	84
A	Tables and diagrams	89
A.1	Simulation setup	89
A.2	Analysis of the flow in the vaned diffuser	92
A.3	Optimization	93

Nomenclature

Identification of pump design versions

<i>Ref, Sim</i>	Simulation data of the original model pump <i>PS550</i>
<i>Ref, Test</i>	Test data of the original model pump <i>PS550</i> = reference configuration as presented in chapter 3
<i>I</i>	Simulation data of the configuration comprised of original rotor and optimized stator as presented in section 6.4
<i>II</i>	Simulation data of the configuration comprised of optimized rotor and optimized stator as presented in section 6.4

Abbreviations

BEP	Best efficiency point
CAD/-M/-x	Computer-aided design, - manufacturing, - technologies
CFD/-O	Computational Fluid Dynamics, Optimization in CFD
CV	Control Volume
DOE	Design of Experiments
EA	Evolutionary Algorithm
ER	Ellipse ratio
GA	Genetic Algorithm
GCI	Grid convergence method/index
GenAgg	Genetic Aggregation algorithm
IF	Interface
(G)OF	(Global) Objective Function
LE, TE	Leading/Trailing edge
LHS	Latin Hypercube Sampling
MOGA	Multi-objective Genetic Algorithm
NSE	Navier-Stokes equations
OL, PL	Overload, Part-load

Nomenclature

OSF	Optimal Space-Filling design
POF	Pareto-optimal frontier
RANS	Reynolds-averaged Navier-Stokes equations
RBNN	Radial Basis Neural Network
RS	Response Surface
SQP	Sequential Quadratic Programming

Physical Constants

g	Gravitational acceleration	m/s^2
-----	----------------------------	----------------

Latin Symbols

A	Area	m^2
B	Bernstein polynomial	
C_p	Pressure coefficient	
c	Absolute fluid velocity	m/s
D	Diffusion factor	1
d	Diameter	m
e	Specific energy	J/kg
H	Total head rise	m
h	Average cell height	m^2
i	Incidence angle	$^\circ$
l	(Chord) length	$\text{m}; \text{mm}$
\dot{m}	Mass flow rate	kg/s
N	Number of grid elements	1
$NPSH$	Net positive suction head	m
n	Rotational speed	rpm
n_q	Specific speed	rpm
P_{hydr}	Hydraulic power	W
P_{mech}	Mechanical power	W
p	Static pressure	Pa
p_{dyn}	Dynamic pressure	Pa
p_t	Total pressure	Pa
p_v	Vapour pressure	Pa
p^*	Normalized pressure	1
Q	Volume flow rate	m^3/s
R	Convergence ratio	1

Nomenclature

r	Radius	m
r, θ, z	Cylindrical coordinates (z =axial)	m
s	Spacing	m
t	Tip clearance; Time	mm; s
u	Circumferential velocity	m/s
V	Volume	m ³
w	Relative fluid velocity	m/s
x, y, z	Cartesian coordinates (z = vertical)	m
y^+	Dimensionless wall distance	1
$z_{R, S}$	Number of blades of rotor, stator	

Greek Symbols

α	Absolute flow angle	°
β	Relative flow angle	°
δ	Diameter coefficient; Deviation angle	1; °
η	Efficiency	1
θ	Deflection angle; with subscript B: Camber angle	°; °
λ	Power coefficient	1
μ	Dynamic viscosity; Exaggeration factor	Pa s; 1
ρ	Density	kg/m ³
σ	Speed coefficient; Solidity	1
τ	Wall shear stress	Pa
ϕ	Flow coefficient; Spare variable	1
ψ	Head coefficient	1
ω	Angular velocity; Total pressure loss coefficient	1/s; 1

Vectors and Tensors

\vec{b}	Bezier-point
\vec{c}	Vector of absolute velocity
\vec{f}	Vector of body forces
\vec{x}	Position vector
\mathbf{T}	Stress tensor

Subscripts

ax	Axial
B	Blade

Nomenclature

<i>Cav</i>	Cavitation
<i>c</i>	Core
<i>eff</i>	Effective
<i>h, s</i>	Hub, Shroud
<i>hydr</i>	Hydraulic
<i>i, m, o</i>	Inner, Mean, Outer streamline - in spanwise direction: 0, 0.5, 1
<i>m</i>	Meridional
<i>max</i>	Maximum
<i>mcs</i>	Measurement cross-section
<i>mech</i>	Mechanical
<i>opt</i>	Optimal
<i>R, S</i>	Rotor, Stator
<i>rec</i>	Recirculation
<i>ref</i>	Reference
<i>Sep</i>	Separation
<i>sim</i>	Simulation
<i>t</i>	Total
<i>test</i>	Model test
<i>th</i>	Theoretical
θ	Circumferential
0	Quantity at shut-off
0, 1, ... 6	Calculation stations, see figures 2.1 and 3.1
1, 2, 3	Indices for mesh refinement: fine, medium, coarse

Chapter 1

Introduction

1.1 Motivation

After two big slumps in 2008 and 2014, the worldwide centrifugal pump consumption has recovered to a solid 40 billion US\$ with an expected annual growth rate of around five percent according to Oxford Economics in cooperation with Europump and the Hydraulic Institute [45]. Persistence Market Research expects the centrifugal pump market to reach an all time high of almost 50 billion US\$ by the end of 2024 [46]. Market analysis by Future Market Insights indicate that mixed-flow and axial pumps account for up to ten percent of the prospering global pump market [21]. Albeit the oil and gas sector remains the largest pump purchasing industry with an approximated market share of 20%, the main reasons for the upward tendency in the global market are the tremendous investments in infrastructure, sanitation, water and wastewater management in the Middle East and in Asian countries [46]. Mixed-flow pumps are particularly suitable in those growing fields. Furthermore a recently published forecast by The McIlvane Company is interesting. It estimates for 2019 that over 40% of the purchase in the pump market will be conducted for the purpose of replacing or upgrading old plants and systems [42].

Because of the steadily increasing demand, not only the whole centrifugal pump market but especially the niche for mixed-flow pumps is becoming more and more attractive for manufacturers of hydraulic machinery that were previously not concentrating their efforts on this specific type of pump. To keep up with the key market players, which currently are KSB AG, Flowserve Corporation,

Grundfos, Xylem Inc. to name some of them, new competitors are in urgent need of developing adequate design processes. They require design tools that allow them to make precise and reliable predictions of the pump characteristics and yet are quick and easy to operate. However, unlike centrifugal and axial pumps, the design method for mixed-flow pumps is not fully developed and there is an urgent need for improvement [39]. In fact, Bing et al. [9] state in their recent work on analysing loss mechanisms of mixed flow pumps that at present numerical flow simulation is the most widely used method for performance prediction of this type of machinery. The reasons therefore lie in the design of the twisted blade profiles whose mathematical description is much more difficult than those of radial or axial impellers, and in the complex dynamics of rotor and stator interaction. This made it much more difficult to find analytical correlations for performance prediction and even today, depending on their specific speed n_q , mixed-flow impellers are still designed according to guidelines for radial ($n_q < 50$) or axial machines ($n_q > 150$). But especially for high specific speed mixed-flow pumps, as for axial propellers, prominent design guidelines, such as the slip factor correlations for centrifugal pumps, become questionable due to the low number of blades [25]. On that account, many developments of modern mixed-flow pumps are still based on the evolution of existing machine layouts with proven performance characteristics as only few methods for the prediction of performance of mixed-flow pumps have been developed so far.

A much more promising approach, however, seems to be the implementation of modern computer aided engineering tools, namely computational fluid dynamics (CFD) and optimization. The combination of the latter two, optimization in computational fluid dynamics (CFD-O), states the beginning of a new era in turbomachinery development. Instead of relying on empirical data and correlations which are very costly to acquire, besides new competitors in the mixed-flow pump market usually do not have access to them, it has now become possible to generate good pump designs even with limited resources. Therefore, the motivation for this thesis is to demonstrate how CFD-O can be implemented in the design procedure of mixed-flow pumps in a way, so that only minor modification of the existing process is needed. This means that the whole process has to be structured in a way that allows its execution on a typical workstation within a reasonable amount of time.

1.2 Scope of work

Based on the motivational statements mentioned above the main goal of the thesis is to provide a workflow of how to reparametrize and optimize an existing pump at restricted expenses. Therefore this thesis focuses on the following key aspects:

1. Remodelling of the existing mixed-flow pump of *Riva Calzoni S.p.A.* on the basis of 2D-drawings (=reference configuration)
2. Assessment of the reference configuration by
 - (a) Analytical criteria
 - (b) Numerical flow simulation with *ANSYS CFX*
3. Optimization of the existing pump with focus on the performance at the best efficiency point (BEP)
 - (a) Detection of geometrical parameters with significant influence on performance characteristics
 - (b) Definition of adequate parameter range according to analytical criteria
 - (c) Set up the Design of Experiments (DoE)
 - (d) Definition of Objective Functions (OF)
 - (e) Execution of the actual Optimization
4. Comparison of the reference configuration against the optimized design

Chapter 2

Theory of centrifugal pump design and numerical methods

The intention of this chapter is to provide a compact introduction in some fields relevant to the hydraulic development of mixed-flow pumps. It starts with a section dealing with the fundamental principles and classification of turbomachinery and is continued by a basic overview and a discussion of the strengths and weaknesses of this type of mixed-flow pumps. Also a few exemplary applications are shown. Then criteria relevant to the design procedure are presented and a brief summary of the numerical methods for solving the Navier-Stokes equations to simulate the flow field is given. The chapter is closed with a more detailed section describing the various steps in the optimization process.

2.1 Fundamental principles

2.1.1 Energy conversion

In a pump with the working fluid assumed to be incompressible, the important flow variables are the static pressure p and total pressure p_t , the volume flow rate Q and the total head rise H . The hydraulic power P_{hydr} , the mechanical power P_{mech} and the efficiency η are of further relevance. Before these integral terms can be introduced the coordinate system and the flow velocities have to be defined.

Velocity triangles

In a fluid-flow machinery a cylindrical coordinate system with r as the radial, $r\theta$ as the circumferential and z as the axial coordinate axis is used for describing quantities in the absolute frame of reference, so that the magnitude of the absolute velocity can be expressed as

$$c = \sqrt{c_r^2 + c_\theta^2 + c_z^2} = \sqrt{c_m^2 + c_\theta^2} \quad (2.1)$$

However, a much more catchy method is to analyse the flow field within the blades along stream surfaces, as proposed by Wu [59]. The point of view is changed to a relative frame of reference which is stationary to the blades hence the flow appears as steady. Then the absolute velocity

$$\vec{c} = \vec{u} + \vec{w} \quad (2.2)$$

is composed of the circumferential velocity \vec{u} of the rotor and of the velocity \vec{w} relative to the blade row¹. The angle between the absolute velocity c and the circumferential direction is identified as absolute flow angle α (also referred to as swirl angle). The angle between the relative velocity w and the circumferential direction is denoted as relative flow angle β . Also shown in figure 2.1 is the definition of the supplementary angles β_1^+ and β_2^+ which is common in the design of hydraulic machinery.

Flow rate

The volume flow rate Q through a control surface can be calculated as follows

$$Q = \int_{\vec{A}} \rho \vec{c} \cdot d\vec{A}, \quad (2.3)$$

\vec{c} being the absolute fluid velocity and \vec{A} the normal vector to the surface. Applied to a turbomachinery stage with the premise of a one-dimensional steady state flow ($\vec{c} \rightarrow c_m = \text{const.}$) equation (2.3) can be simplified to $Q = c_m \cdot A$, whereby A represents the area perpendicular to the flow direction.

¹For convenience, vector symbols are omitted in the following.

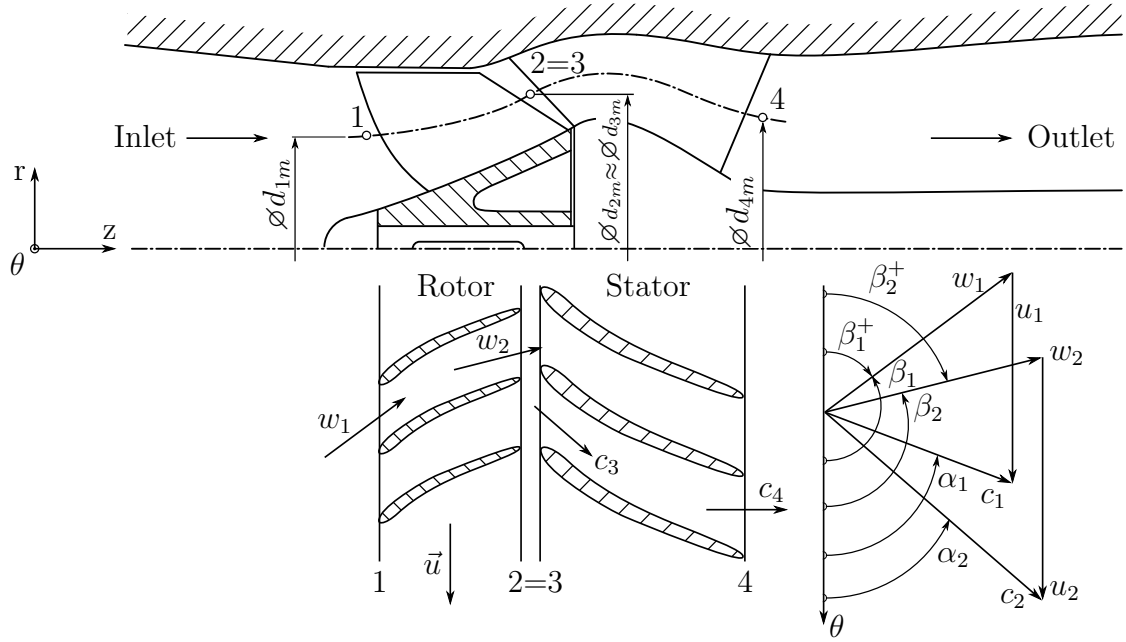


Figure 2.1: Meridional contour and velocity triangles of a mixed-flow pump

Total head rise

Starting from *Euler's equation of motion* for one dimensional, steady, inviscid flows

$$\frac{1}{\rho} dp + c dc + g dz = 0 \quad (2.4)$$

Bernoulli's equation which corresponds to the specific energy e of the fluid can be obtained by integration in stream direction:

$$\frac{p}{\rho} + \frac{c^2}{2} + gz = e = \text{const.} \quad (2.5)$$

Multiplying equation (2.5) by the density transforms Bernoulli's equation into its pressure form

$$p + \frac{\rho}{2} c^2 + \rho g z = p_t + \rho g z = \text{const.} \quad (2.6)$$

in which the total pressure is given as

$$p_t = p + \frac{\rho}{2} c^2 \quad (2.7)$$

Analogously the total head rise H of a pump is defined as the difference in total pressure between inlet and outlet added by the geodetical difference $\Delta z =$

$z_{Outlet} - z_{Inlet}$.

$$H = \frac{\Delta p_t}{\rho g} + \Delta z = \left[\frac{p_t}{\rho g} + z \right]_{Inlet}^{Outlet} \quad (2.8)$$

In case only the rotor shall be assessed, then the formula for the head needs to be evaluated between calculation stations one and two.

$$H_R = \left[\frac{p_t}{\rho g} + z \right]_1^2 \quad (2.9)$$

Hydraulic power

Interpreting the total head rise as specific energy $Y = g \cdot H$ leads to the hydraulic power

$$P_{hydr} = \dot{m} \cdot Y = \rho Q g H , \quad (2.10)$$

\dot{m} being the mass flow rate.

Torque on blade row

The torque exerted by the flow on the blade row is calculated by *Euler's turbomachinery equation* which can be gained from the balance of moment of momentum. A detailed derivation of the moment of momentum can be looked-up in many textbooks, e.g., Schobeiri [49]. For the following definitions, only the final result displayed in equation (2.11) for steady flow is of practical interest.

$$\vec{T} = \int_{\vec{A}_2} \rho \cdot (\vec{r}_2 \times \vec{c}_2) \cdot (\vec{c}_2 \cdot d\vec{A}) - \int_{\vec{A}_1} \rho \cdot (\vec{r}_1 \times \vec{c}_1) \cdot (\vec{c}_1 \cdot d\vec{A}) \quad (2.11)$$

Applied to incompressible and inviscid flow, assuming that the flow follows the blades smoothly without slip and the velocity distribution at the inlet and exit of the blade passages is fully uniform, the one-dimensional form of *Euler's turbomachinery equation* in the notation for pumps can finally be expressed as

$$T = \rho Q \cdot (r_2 c_{2\theta} - r_1 c_{1\theta}) = \rho Q \cdot (r_2 c_2 \cos \alpha_2 - r_1 c_1 \cos \alpha_1) \quad (2.12)$$

Mechanical power

The mechanical power consumed by the pump is calculated by

$$P_{mech} = T \cdot \omega = \rho Q \cdot (u_2 c_{2\theta} - u_1 c_{1\theta}) = \rho Q \cdot \Delta (uc_\theta) \quad (2.13)$$

whereby ω is the angular velocity of the rotor.

Efficiency

Finally, the efficiency of the pump results in

$$\eta = \frac{P_{hydr}}{P_{mech}} = \frac{g \cdot H}{\Delta (uc_\theta)} \quad (2.14)$$

If only the impeller is considered, then its efficiency can be written as

$$\eta_R = \frac{g \cdot H_R}{\Delta (uc_\theta)} \quad (2.15)$$

2.1.2 Dimensionless quantities

The most prominent quantity for the classification of hydraulic machinery is the specific speed

$$n_q = n \cdot \frac{\sqrt{Q}}{H^{\frac{3}{4}}} \quad (2.16)$$

which is computed with the rotational speed n , the volume flow rate Q and the total head rise H . To achieve correct results for n_q which is typically given in rpm, n must be inserted in rpm, Q in m³/s and H in m.

Throughout this thesis design points are expressed in non-dimensional form. The volume flow rate Q , the total head rise H and the mechanical power P_{mech} are replaced by the flow coefficient ϕ

$$\phi = \frac{4 \cdot Q}{d_{2o}^3 \cdot \pi^2 \cdot n} \quad (2.17)$$

the head coefficient ψ

$$\psi = \frac{2 \cdot g \cdot H}{d_{2o}^2 \cdot \pi^2 \cdot n^2} \quad (2.18)$$

and the power coefficient λ

$$\lambda = \frac{8 \cdot P_{mech}}{d_{2o}^5 \cdot \pi^4 \cdot n^3 \cdot \rho} \quad (2.19)$$

respectively². In these definitions Q , H and P_{mech} are non-dimensionalized with the maximum diameter of the impeller outlet d_{2o} , its rotational speed n and the density ρ of the fluid. All quantities must be inserted in coherent SI units.

The speed coefficient σ

$$\sigma = \frac{\phi^{\frac{1}{2}}}{\psi^{\frac{3}{4}}} = n \cdot \frac{\sqrt{Q}}{(2 \cdot g \cdot H)^{\frac{3}{4}}} \cdot 2 \cdot \sqrt{\pi} \quad (2.20)$$

and the diameter coefficient δ

$$\delta = \frac{\psi^{\frac{1}{4}}}{\phi^{\frac{1}{2}}} = d_{2o} \cdot \sqrt[4]{\frac{2 \cdot g \cdot H}{Q^2}} \cdot \frac{\sqrt{\pi}}{2} \quad (2.21)$$

provide a different way to identify a design point uniquely.

Individual pressure quantities (static or total) are normalized by an artificially built dynamic pressure $\rho/2 \cdot u_{2o}^2$:

$$p^* = \frac{2 \cdot p}{\rho u_{2o}^2} \quad (2.22)$$

For the scaling of static pressures differences the pressure coefficient

$$C_p = \frac{\Delta p}{p_{dyn}} \quad (2.23)$$

and for the scaling of pressure losses, the total pressure loss coefficient

$$\omega = \frac{\Delta p_t}{p_{dyn}} \quad (2.24)$$

are introduced. Within these two equations, the dynamic pressure is evaluated as the difference between total and static pressure at the accordant calculation station.

²The head of the rotor H_R is expressed in non-dimensional form as ψ_R analogue to equation (2.18).

2.1.3 Cordier diagram

Both, speed coefficient and diameter coefficient play an important role in the theory of fluid-flow machinery. Cordier [15] calculated diameter and speed coefficients for a large number of fluid-flow machines in service and plotted the results in a logarithmic diagram which presents a single relationship $\delta = f(\sigma)$ [58]. Later contributions to Cordier's theory by Casey et al. [13] or Willinger et al. [58] suggest that there is not only a single Cordier-band, but rather a set of curves at which all design points of a fluid-flow machine are located depending on their flow and head coefficients. The Cordier diagram itself and the position of the *PS550* model pump on the Cordier curve are presented in the appendix (figure A.2).

2.2 Mixed-flow pumps

2.2.1 General

Mixed-flow pumps belong to the group of centrifugal pumps which are the most widely used pump type in the world [32, 45]. The main purpose of any pump is to increase the fluid pressure from inlet to outlet by transferring mechanical energy of the impeller to the fluid. The impeller (rotor) always works in combination with a guide mechanism (stator) that can be either a volute or an annular diffuser (with or without vanes), depending on the specific speed³ of the pump. The mechanical energy of the rotor causes an acceleration of the working fluid within the impeller blades and the fluid enters the guide mechanism with increased velocity, thus with a high dynamic pressure. In the stator component the fluid is decelerated and the dynamic pressure is converted into the desired static pressure rise.

Figure 2.2 gives a survey of the different impeller designs depending on their specific speed. the guide mechanism is indicated by a light blue color. Definitions of the variables used in figure 2.2 are given in section 2.1. It can be seen that mixed-flow pumps combine features of both, centrifugal and axial pumps. They are able to achieve significantly higher heads of up to 100 m per stage compared to a maximum of around 15 m for axial pumps, while at the same time they are more compact and lightweight than centrifugal pumps at comparable flow rates. This derives

³For a definition of the specific speed refer to 2.1.2

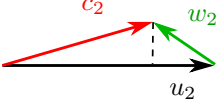
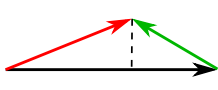
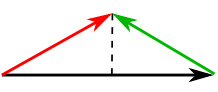
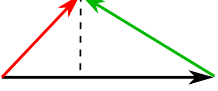
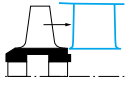
n_q in rpm	Impeller type		Velocity triangle at impeller outlet	$H_{st,opt}$ in m	ψ_{opt}	δ_{opt}	η_{opt} in %
10 - 30	Centrifugal	HP		800 (1200)	1 - 1.2	5 - 15	40 - 88
30 - 50		MP		400	0.9	3.5 - 5.0	70 - 92
50 - 100		LP		60	0.65	2.0 - 3.5	60 - 88
80 - 160	Mixed-flow			20 - 100	0.4 - 1.0	1.5 - 1.8	70 - 90
150 - 400	Axial			2 - 15	0.1 - 0.4	1.2 - 1.8	70 - 88

Figure 2.2: Classification of pumps (HP = high pressure, MP = medium p., LP = low p.; st = stage), modified from [11, 24, 36]

from the fact that most mixed-flow pumps have a vaned diffuser which has a smaller diameter than an otherwise installed volute casing. For $n_q > 60$ mixed-flow pumps are superior to centrifugal pumps, because the flow at the impeller outlet is more uniform [24]. An additional benefit of mixed-flow pumps is that they have a higher suction capability than axial pumps [12]. Their impeller may be shrouded for rotors with lower n_q or unshrouded for rotors with higher n_q . Furthermore, there are mixed-flow pumps with adjustable rotor blades to expand the operating range. Multi-stage mixed-flow pumps are used as vertical bore-hole pumps for water supply, which require, for economic reasons, the smallest possible diameter [24]. Like centrifugal pumps low specific speed mixed-flow pumps have a single or double volute casing, whereas in high specific speed mixed-flow pumps the rotor is followed by a vaned diffuser.

2.2.2 Performance characteristics

Two of the most distinct features of mixed-flow pumps compared to radial pumps are the much steeper head curve which may even be saddle-shaped, thus unstable at certain flow rates and the power curve with negative slope, as can be seen in figure 2.3. The high power consumption of mixed-flow and axial pumps at a flow rate of $Q = 0$ in relation to the power consumption at their best efficiency point (BEP) is the reason why those machines are not started against a closed valve, which would overload the drive motor [12]. A thorough explanation of the underlying physical principles is given in Gülich [24] and will be summarized in the following paragraph.

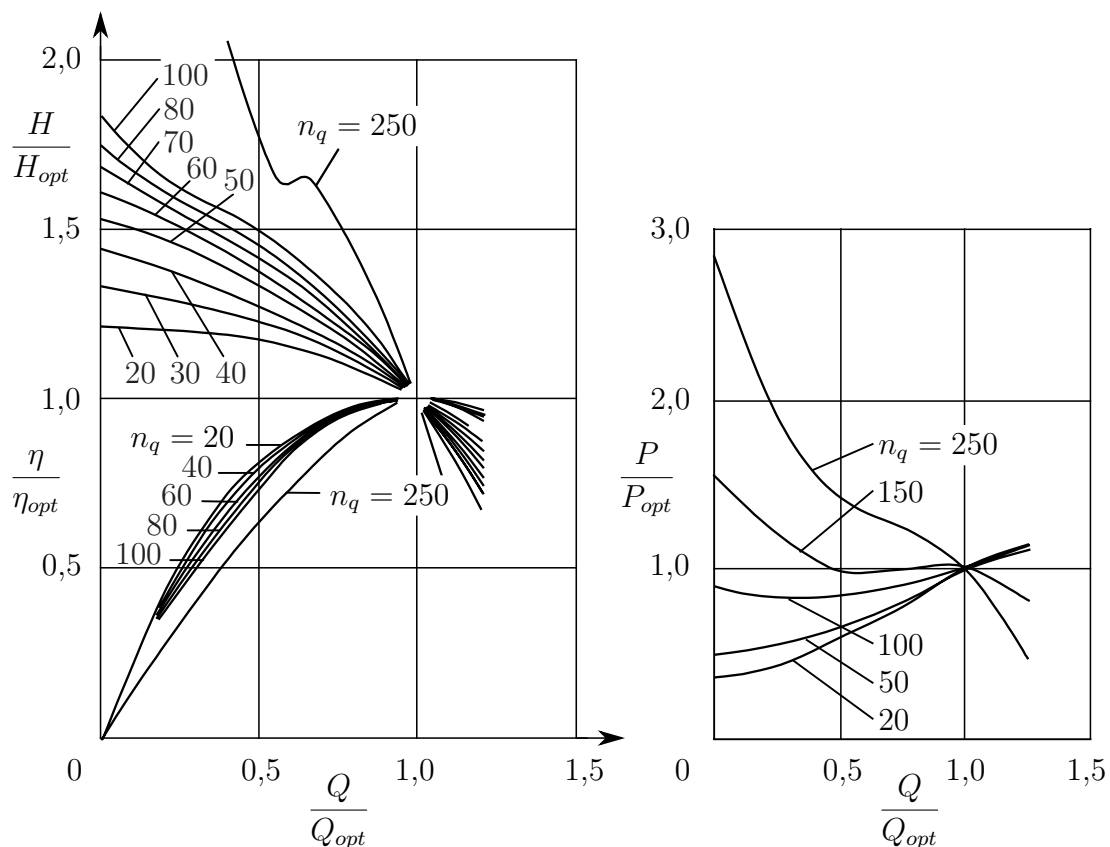


Figure 2.3: Characteristic curves for various specific speeds n_q (rpm), modified from [24]

The reason for the steep head curve of pumps with high n_q is that in those machines flow phenomena such as backflow and recirculation lead to a bigger head rise at zero flow rate.

According to Euler, the theoretical head rise

$$H_{th} = H_u + H_w + H_c = \frac{u_2^2 - u_1^2}{2g} + \frac{w_1^2 - w_2^2}{2g} + \frac{c_2^2 - c_1^2}{2g} \quad (2.25)$$

can be divided into three components $H_u + H_w + H_c$. H_c is the portion of the head which is caused by the acceleration of the absolute flow in the impeller. In the diffuser it will be turned into a static pressure rise. The deceleration of the relative velocity w between impeller inlet and outlet accounts for H_w . The reason for H_u are the centrifugal forces, a result of the rotation of the impeller.

At lower flow rates recirculation sets in, so that the outer part of the inlet cross section of the impeller is blocked. This causes the streamlines to enter the impeller at a smaller diameter $d_{1,\text{eff}}$ and in turn relates to a higher centrifugal head rise H_u . In fact, the recirculation raises the theoretical head by

$$H_{rec} = \frac{u_2^2}{2g} \cdot \left(\frac{d_{1m}^2}{d_{2m}^2} - \frac{d_{1,\text{eff}}^2}{d_{2m}^2} \right) \quad (2.26)$$

which results in a centrifugal head rise of

$$H_{u,\text{eff}} = H_u + H_{rec} = \frac{u_2^2 - u_{1,\text{eff}}^2}{2g} \quad (2.27)$$

Equations (2.26) and (2.27) show that a stronger recirculation, which blocks a higher amount of the inlet cross section and so moves the streamlines even more towards lower diameters $d_{1,\text{eff}}$, finally leads to a bigger head rise. The effect of recirculation grows with the flow rate declining until it reaches its maximum at $Q = 0$ (figure 2.4 left). According to equation (2.26) the recirculatory head rise H_{rec} increases with the square of the relation between inlet diameter d_{1m} and outlet diameter d_{2m} . As d_{1m}/d_{2m} converges to one with rising specific speed n_q , H_{rec} becomes larger as well. The diagram to the right of figure 2.4 depicts the centrifugal head rise $H_{u,\text{opt}}$ at BEP and at zero flow rate $H_{u,0}$. The difference between those two quantities corresponds to the recirculatory head rise $\Delta H_{rec,0}$ at $Q = 0$. It is proportional to the specific speed and responsible for the steepness of the head curve of mixed-flow and axial pumps towards shut-off.

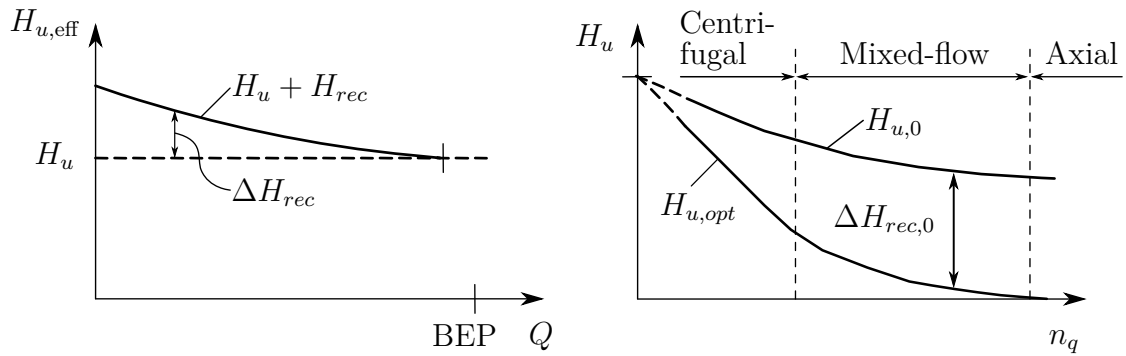


Figure 2.4: left: Effect of recirculation at impeller inlet on centrifugal head rise; right: Impact of n_q on centrifugal head rise, modified from [24]

2.2.3 Applications

As mentioned before, mixed flow pumps are best for pumping large amounts of water against low to medium heads. This makes them suitable for a wide range of applications such as:

- Cooling water pumps for thermal power plants
- Water pumps for irrigation in agriculture
- Sea water intake pumps for desalination plants
- Sewage and waste water treatment
- Urban water management
- Shipyard pumps [23]
- Process pumps in the chemical industry, food industry or pulp and paper industry
- Marine waterjet propulsion [27]
- Feeder pumps for rocket fuel systems [16]

Vertical Pumps

Two typical examples of the mixed-flow concept are represented by Sulzer's vertical pumps *SJT* [53] and *SJM* [52], which are shown in figure 2.5.

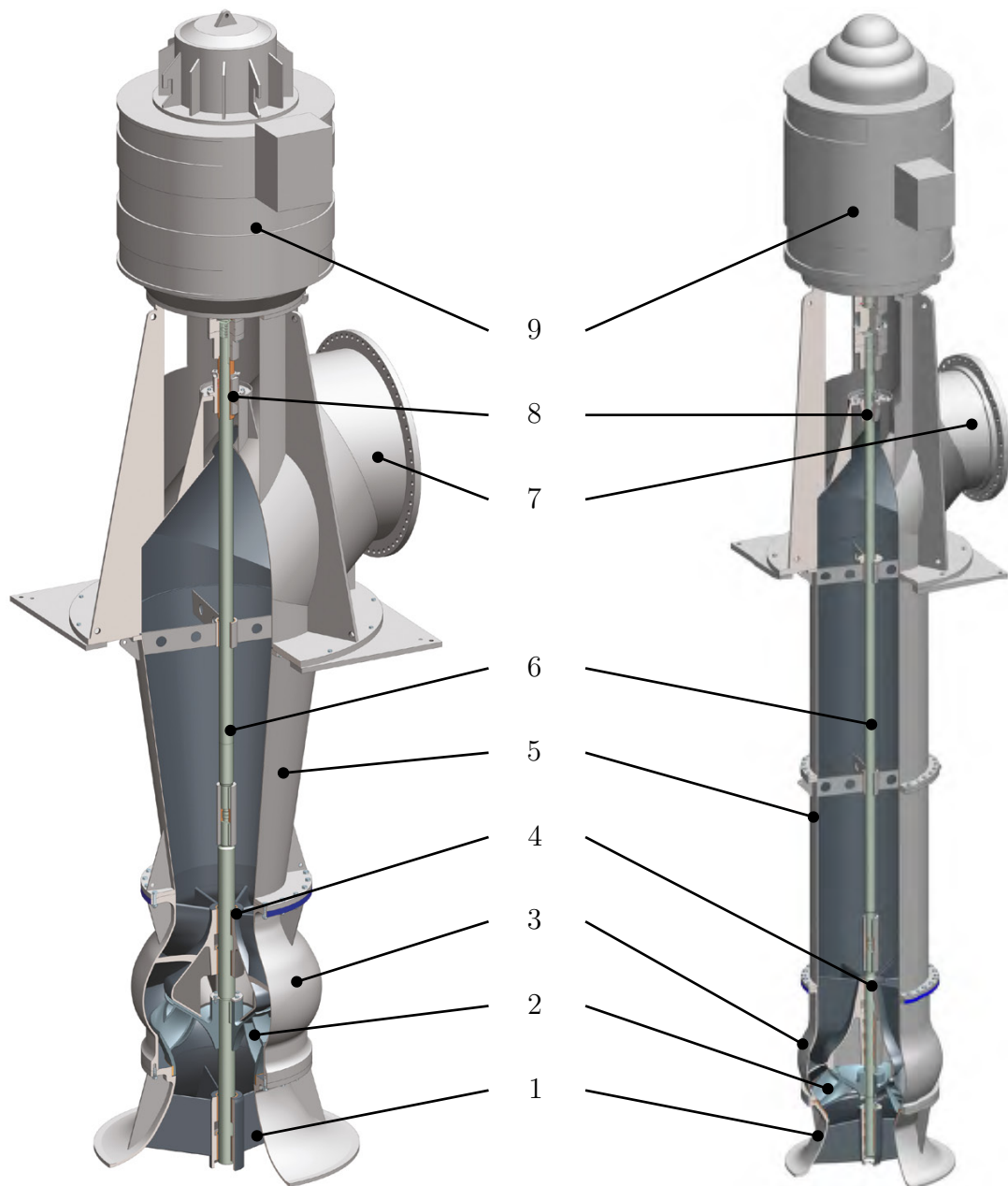


Figure 2.5: left: Sulzer SJT vertical turbine pump [53]; right: Sulzer SJM vertical mixed-flow pump [52]; 1 suction bell, 2 mixed-flow impeller, 3 bowl, 4 bowl bearings, 5 column assembly, 6 shaft, 7 discharge head, 8 shaft seal, 9 drive motor

Common applications for these specific types of mixed-flow pumps are cooling water pumps in thermal, nuclear or renewable power stations, water supply and irrigation pumps and booster services. Because of their compact design they are also used in pipelines as inline-pumps.

Vertical pumps consist of the following main components [53]:

1. Suction bell: The purpose of a suction bell is to provide a uniform velocity distribution at the impeller inlet. It may be equipped with anti-vortex ribs to prevent pre-swirl.
2. Mixed-flow impeller: The impeller can be closed (shrouded) or semi-open (unshrouded). Often it is mounted on the shaft by a key and split thrust ring.
3. Bowl: The bowl surrounds the impeller and the vaned diffuser in which the conversion of kinetic energy of the fluid into static pressure takes place.
4. Bowl bearings: Bowls can be fitted with metal or dual (rubber and metal) bearings
5. Column assembly: Column pipes may be conical or cylindrical. Cylindrical pipes are used for inline application, whereas in conical pipes the fluid flow experiences a further deceleration.
6. Shaft: The shaft is sized for maximum torque and made of stainless steel or duplex steel. Line shafts are connected by a split ring, key and sleeve couplings.
7. Discharge head: The discharge head features a 45 to 90 degree bend and a motor stool which the drive motor can be attached to.
8. Shaft seal: As usual with pumps, sealing of the shaft is provided by a packed stuffing box.
9. Drive motor

2.2.4 Acceptance tests

At the end of the development process of a pump, it is inevitable to prove its performance by acceptance tests. The purpose of these tests is to demonstrate the

fulfillment of the technical, hydraulic and mechanical guarantees agreed between the purchaser and the pump maker [54].

There are four types of tests:

1. Works or factory acceptance tests: These tests are performed on the manufacturer's test stand under reproducible conditions which makes them the most accurate.
2. Field tests: A field test is carried out directly at the plant at which the pump is installed. Results of this type of test hugely rely on the instrumentation and measuring positions.
3. Periodic field tests: The purpose of these tests is to detect changes or wear on the pump in operation.
4. Model tests: In case of a one hundred percent hydraulic model fidelity this test is a replacement for acceptance tests on the full-scale pump.

The aforementioned acceptance tests are subject to thorough standardization. Relevant codes for pumps are

- DIN EN ISO 9906:2012 Rotodynamic pumps - Hydraulic performance acceptance test - Grades 1, 2 and 3 [31]; abbr. ISO 9906
- DIN EN ISO 5198:1998 Centrifugal, mixed flow and axial pumps - Code for hydraulic performance tests - precision class [30]; abbr. ISO 5198
- ASME PTC 8.2: Centrifugal Pumps [5]
- ANSI/HI 12.1-12.6 – 2005: American National Standard for Rotodynamic (Centrifugal) Slurry Pumps [1]

Within the European Union, ISO 9906 and ISO 5198 are the most widely accepted standards for pumps. Therefore, the following section will give a brief introduction into the more general ISO 9906. This code defines a framework for acceptance tests which may take place at test stands of the manufacturer as well as at those of laboratories, for all types of centrifugal pumps (radial, mixed-flow and axial) of any size and any working fluid that reacts just as cold, clear water. It distinguishes between three acceptance grades (table 2.1): grade one having the highest precision

Grade	1			2		3	Guarantee requirement
$\Delta\tau_Q$	10%			16%		18%	
$\Delta\tau_H$	6%			10%		14%	
Acceptance grade	1U	1E	1B	2B	2U	3B	Mandatory
$\Delta\tau_Q$	+10%	$\pm 5\%$	$\pm 8\%$	16%	$\pm 9\%$		
$\Delta\tau_H$	+6%	$\pm 3\%$	$\pm 5\%$	10%	$\pm 7\%$		
$\Delta\tau_P$	+10%	+4%	8%	16%	9%		Optional
$\Delta\tau_\eta$	$\geq 0\%$	-3%	- % ^a		-7%		
Note $\tau_x (x = Q, H, P, \eta)$ stands for the tolerance of the indicated quantity.							

Table 2.1: Acceptance grades and corresponding tolerances for pump tests, modified from [31]

and grade three the lowest. The letters *U* and *B* stand for one or two-sided tolerance areas, whereas *E* indicates a class suitable for energy-efficient machines. Purchaser and maker of the pump are free to agree on any of these six grades. The guarantee requirement is fulfilled if the head curve intersects the cross spanned by the tolerance values $\Delta\tau_Q$ and $\Delta\tau_H$ around the guarantee point (Q_G, H_G) (green curves in figure 2.6).

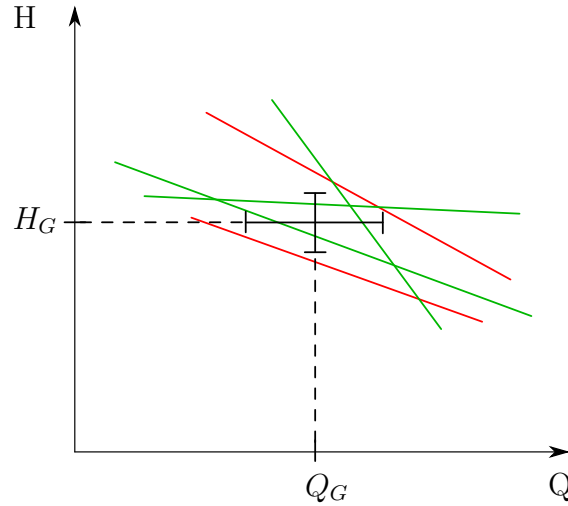


Figure 2.6: Acceptance for two-sided tolerance area: green - pass, red - fail, [31]

The standard IEC 60193 is not applicable to typical mixed-flow pumps, as it specifies to be valid only for models of prototype machines either with a unit power greater than 5 MW or with a reference diameter greater than 3 m [29]. Furthermore it applies only to laboratory models of any type of hydraulic turbine, storage pump or pump turbine.

2.3 Design procedure

When working on the advancement of hydraulic machinery, it is highly recommended to get a general idea of the expected behaviour of the machine by consulting analytical criteria before starting numerical flow analysis. Such criteria provide a good estimation of important design factors such as the correct blade angles, blade length, hub and shroud geometry and blade loading. Therefore, those criteria that have been relevant to this thesis together with an introduction into blade parametrization are presented in the following section.

2.3.1 Reparametrization

A common task in refurbishment projects of pumps is to replace the old blades of the impeller and the diffuser by improved ones, while keeping the meridional contour of hub and shroud unchanged. This means that the emphasis of such projects is directed to the redesign of rotor and stator blades. A key issue when redesigning the blades is to acquire valid geometrical data from the existing blade in order to start modification. Basically there are three common ways to achieve this:

1. Paper or CAD-drawings
2. Point data of the blade in model scale, measured on a 3D scanner
3. Point data of the full scale blade, recorded with a measurement arm

A much better start of the reparametrization can be guaranteed if the design engineer has access to parametric data of a proven blade layout which unfortunately is rarely the case with refurbishment projects. All the above mentioned approaches have one primary goal in common - to assign numerical values to the geometrical shape of the blades. Hajek [26] describes this process of parametrization as a way of transforming the engineering problem into a mathematical one.

There are two well-established methods to express the blade geometry mathematically, which both rely on two-dimensional blade profile definitions:

1. Camberline-Thickness method
2. Airfoil function method

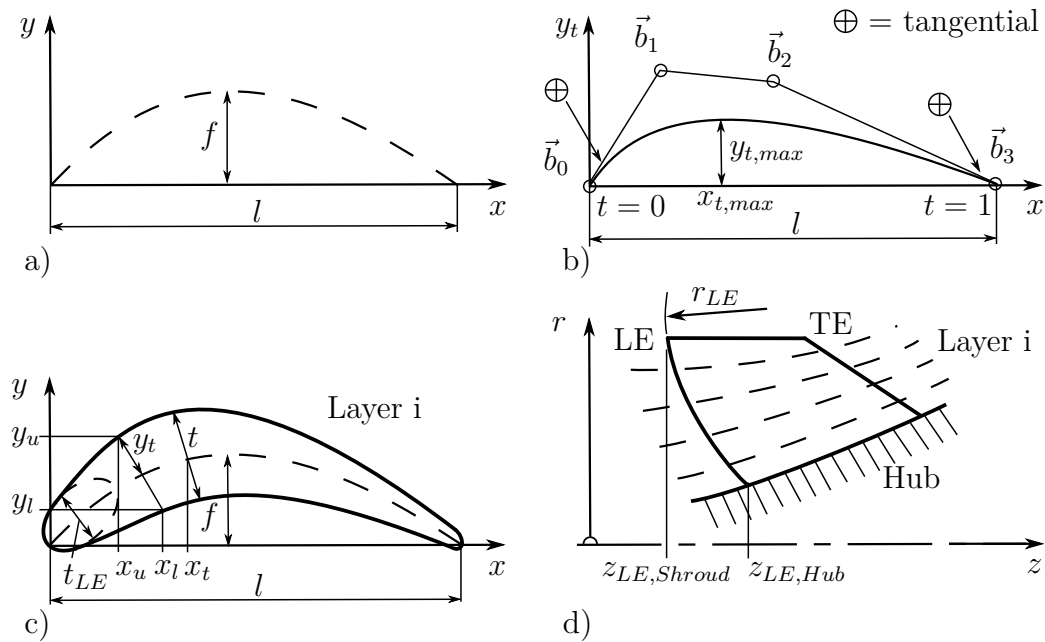


Figure 2.7: a) Mean line; b) Thickness distribution; c) Blade profile of layer i as superposition from a) and b); d) Meridional section of blade

Camberline-Thickness method

A classical way of determining the blade profile is to define the mean line (=camberline) and the thickness distribution of the profile as shown in figure 2.7.

The blade itself is made up of numerous layers of constant span. In each layer the blade profile is stored as a superposition of the mean line $y(x)$ and the thickness distribution $y_t(x)$. The meridional contour (figure 2.7 d) defines the stacking of the layers in radial direction as well as the position and shape of the leading (LE) and the trailing edge (TE). LE and TE can be detailed further by setting the thickness t_{LE} and t_{TE} and the ellipse ratios (ER_{LE} and ER_{TE}). The ellipse ratio is defined as the relation between the semi-major and semi-minor axes, where the length of the minor axes is equated with t_{LE} . For optimization it is crucial to find adequate parametrization of the mean line $y(x)$ and the thickness $y_t(x)$.

Airfoil function method

Similar to the camberline-thickness method the target of the airfoil function approach is to find a mathematical relation that describes the blade profile. In

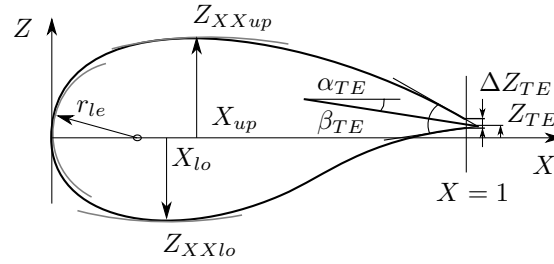


Figure 2.8: PARSEC airfoil geometry defined by eleven basic parameters, modified from [51]

contrast to the superposition of mean line and thickness function introduced before, this time the blade is directly defined by means of relations in the form of

$$Z = F_j(\vec{p}, X) \quad (2.28)$$

with a parameter vector $\vec{p} = (p_1, p_2, \dots, p_k)$ and X and Z being the airfoil coordinates [51]. Again, the goal is to find a function that makes use of a minimum number of parameters in order to keep computational costs for subsequent optimization at an acceptable level. For this purpose Sobieczky [51] introduced the *PARSEC* algorithm, which relies on polynomial functions of up to the sixth order to describe the upper and lower surface of a wing independently. This gives the airfoil function

$$Z_{PARSEC} = \sum_{n=1}^6 a_n(\vec{p}) \cdot X^{n-\frac{1}{2}} \quad (2.29)$$

in which the coefficients a_n are determined by the geometric parameters illustrated in figure 2.8.

Parametrization with Bezier-curves

In this thesis the camberline-thickness method in combination with Bezier-curves was chosen, because it is fully supported within the *BladeEditor* module of *ANSYS DesignModeler*.

For each layer i , there is one Bezier-curve for the mean line and one for the thickness distribution (figure 2.7 b), whereby every Bezier-curve of the order n can be defined by its Bezier-points \vec{b}_i and the Bernstein basis polynomials $B_i^{(n)}(t)$ as

follows ($t \in [0, 1]$ and $i = 0 \dots n$):

$$\vec{x}(t) = \begin{pmatrix} x(t) \\ y(t) \end{pmatrix} = \sum_{i=0}^n \vec{b}_i \cdot B_i^{(n)}(t) \quad \text{with} \quad B_i^{(n)}(t) = \binom{n}{i} \cdot t^i \cdot (1-t)^{n-i} \quad (2.30)$$

These sets of points, together with the shape and position of leading and trailing edges, provide a variety of free parameters for the optimization process.

2.3.2 Blade design

In terms of impeller design mixed-flow pumps with specific speed greater than $n_q = 150$ can be treated similarly to propeller pumps. Concepts known from centrifugal pumps such as slip factor are not applicable any longer because of the large spacing between the individual blades [24]. The following guidelines are useful not only in the design process of a new machine, but also allow to check the existing rotor and stator if they were designed properly.

Axial length

In his reference books on centrifugal pumps, Gülich specifies the following recommendation for the minimum chord length l of a mixed-flow impeller blade at the outer streamline [24]:

$$\left(\frac{l}{d_2} \right)_o \geq 1.1 \left(\frac{\beta_{2o}^+}{25} \right) \left(\frac{n_q}{200} \right)^{0.4} \quad (2.31)$$

A guide value for the minimal axial length l_{ax} of diffuser vanes at the mean streamline can be assessed from the demand that the diffuser losses according to the deflection and deceleration of the flow shall be kept low.

$$\left(\frac{l_{ax}}{d_4} \right)_m = 0.72 \left(\frac{n_q}{200} \right)^{0.19} \quad (2.32)$$

Blade angles

Starting from the desired or given performance data of the hydraulic machine (typically Q_{opt} and H_{opt}), first the main dimensions (rotor diameters) and the flow

velocities are calculated. From them the flow angles can be acquired. There are three common concepts to establish a correlation between flow angles (α, β) and blade angles (metal angles) (α_B, β_B) :

1. Slip factor correlations
2. Incidence and deviation
3. Angle exaggeration

Generally speaking, the goal of all of these concepts is to account for the deviation of the real flow from the blade congruent idealization, in which the fluid follows the blade smoothly and without slip. This deviation, particularly with radial impellers, is mainly caused by the Coriolis force that acts against the direction of rotation and triggers a secondary flow towards the pressure side of the blade [24]. Therefore, slip factor correlations are mostly used for radial pumps and compressors, whereas the concepts of incidence and deviation as well as angle exaggeration (which are very similar) are more common with axial machines. Incidence i is defined, so that it is positive in part-load and negative in overload. This results in

$$i_R = \beta_1 - \beta_{1B} = \beta_{1B}^+ - \beta_1^+ \quad \text{and} \quad i_S = \alpha_{3B} - \alpha_3 \quad (2.33)$$

for the incidence at the rotor (index R) and for the stator (index S). For the deviation δ the same definition

$$\delta_R = \beta_2 - \beta_{2B} = \beta_{2B}^+ - \beta_2^+ \quad \text{and} \quad \delta_S = \alpha_{4B} - \alpha_4 \quad (2.34)$$

can be applied accordingly, if a positive correlation between inlet and outlet flow angles is assumed.

In 1935, Weinig [57] developed a simple procedure for calculating the angle exaggeration for cascades with low deflection depending only on the stagger angle γ_m and the inverse of the solidity $1/\sigma$ at midspan (see figure 2.9). The stagger angle γ_m is the angle between the chord line (of length l) and the circumferential direction. The solidity σ is defined as the chord-spacing ratio

$$\sigma = \frac{l}{s} \quad \text{with} \quad s = \frac{d\pi}{z}, \quad (2.35)$$

in which s equals the spacing at a diameter d , l the chord length and z the number of blades in the cascade. The exaggeration factor μ (figure 2.9 right) can be

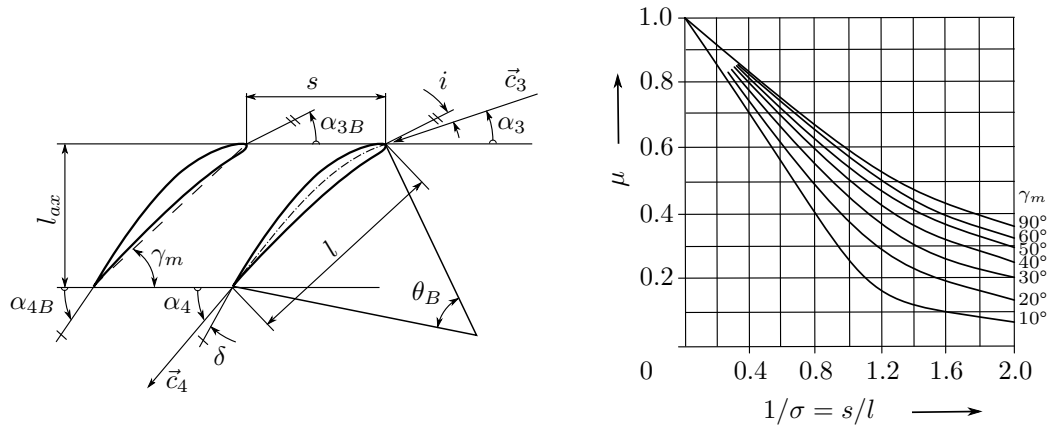


Figure 2.9: left: Cascade geometry for stator, modified from [18]; right: Angle exaggeration factor, modified from [10]

obtained by these two parameters.

The required exaggeration is eventually computed by

$$\Delta\alpha_B = \frac{(1 - \mu) \cdot \theta_B^*}{2} \quad \text{with} \quad \theta_B^* = \frac{\theta_B}{\mu} \quad (2.36)$$

Here the θ_B^* stands for the corrected camber angle and $\theta_B = |\alpha_{4B} - \alpha_{3B}|$ for the camber angle of the profile. The exaggeration should be split into equal portions for the leading and trailing edge of a profile [10]. Though Weinig's procedure is applicable to rotor and stator cascades, Gülich gives a more specific relation for vaned diffusers. He recommends a slight exaggeration of 4° to 6° [24] for the outlet of a vaned diffuser which is designed for swirl-free discharge flow, .

Blade loading

Flow separation in the blade passage, caused by the decelerated flow in compressor cascades, is the main boundary for blade loading. In fact, to prevent flow separation, maximum allowable deflection within a passage has to be limited. More generally spoken, the main relation to describe the threat of flow separation within a compressor blade passage was given by de Haller [17]. With the help of experiments, he found out that the maximum deceleration of the flow (caused by deflection) in

a rotor cascade must not fall below

$$\left(\frac{w_2}{w_1}\right)_i \geq \begin{cases} 0.55 \div 0.6 & \text{single-stage machines} \\ 0.7 & \text{multi-stage machines} \end{cases} \quad (2.37)$$

These limits count for the flow at the hub, at which the deflection and thus the deceleration is larger than at midspan or at the blade tip. In multi-stage machines the boundary layer at the hub is thicker than that in single-stages machines, hence more prone to separation. Therefore the limit has to be higher [47].

Starting from the incompressible, two-dimensional, turbulent boundary layer theory, Lieblein [38] deduced a simplified blade loading criterion which provides a supplement to de Haller's criterion for determining limiting design conditions in compressor stages. While in de Haller's approach the limit is dictated by the separation of the sidewall boundary layers, Lieblein found out that blade loading is also governed by the stability of the blade boundary layers. This means that not only the global deceleration from w_1 at the inlet to w_2 at the outlet of stage, but also the deceleration from the maximum relative velocity w_{max} at the blade surface to the outlet velocity w_2 is a decisive factor. Hence, Lieblein's diffusion factor states

$$D = \frac{w_{max} - w_2}{w_1} \quad (2.38)$$

The maximum relative velocity w_{max} can be calculated by [47]

$$w_{max} = w_1 + \frac{1}{2\sigma} \cdot \Delta w_\theta \quad (2.39)$$

Equations (2.38) and (2.39) combined result in

$$D = 1 - \frac{w_2}{w_1} + \frac{1}{2\sigma} \frac{w_{1\theta} - w_{2\theta}}{w_1} \quad (2.40)$$

This formula is comprised of the ratio of relative velocities w_2/w_1 (which in fact is the de Haller criterion for two dimensional blade rows) and a term accounting for the circulation about the blade $(w_{1\theta} - w_{2\theta})/w_1$ multiplied by the inverse solidity σ of the blade⁴. Gülich [24] states a maximum diffusion factor of 0.45 at the shroud and 0.6 at the hub for axial pumps. Equation (2.40) shows that for a certain deflection, required by the design point, the solidity becomes the main parameter to influence blade loading. A high solidity can always be achieved by lengthening the

⁴ $\Delta w_\theta = \Delta c_\theta$

blades or by increasing the number of blades, see equation (2.35). Longer blades give the flow more time to reach the desired deflection, whereas more blades equal to a lower load on a single blade. Finally, it has to be mentioned that the criteria of de Haller and Lieblein are applicable to both, rotor and stator cascades. But in this section, for convenience sake, they were presented in the notation for rotor blade passages.

2.3.3 Meridional contour

A common phenomenon that can occur in turbomachinery with main flow in axial direction is flow separation at the hub which is known as hub dead water or dead water core [47]. Bammert and Kläukens showed that the appearance of hub dead water is inherently depending on the swirl of the flow [7]. In fluid flow machinery a swirl-flow is present especially in the bladeless annular space between the cascades. In mixed-flow pumps the diffuser vanes are designed to straighten the flow, so that the discharge of the pump is swirl-free in the BEP. However, in part-load, or in case the vanes fail to extract the circumferential component of the flow, a residual swirl may remain in the fluid, which can cause the hub dead water.

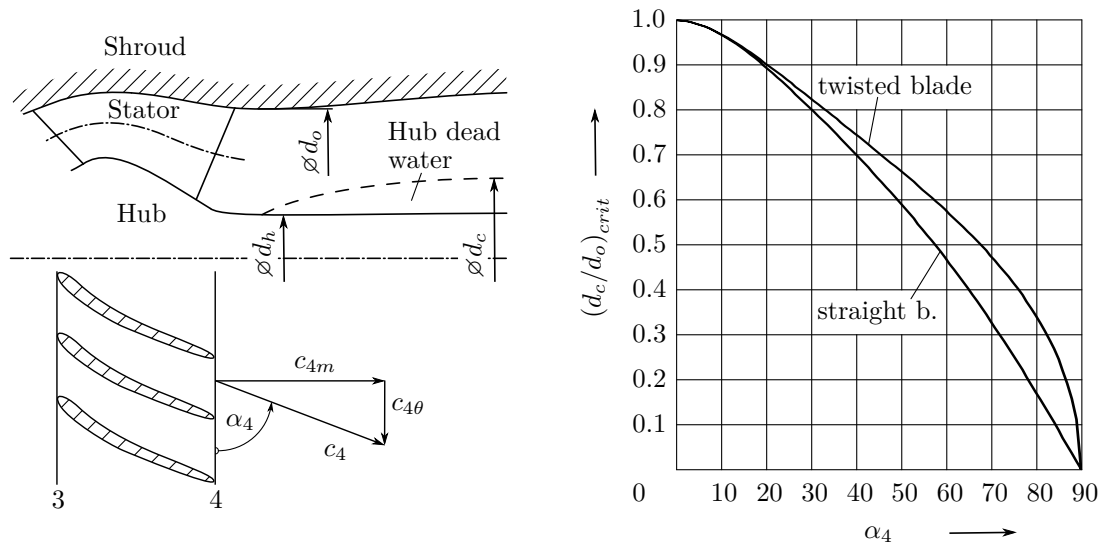


Figure 2.10: left: Flow through guide vanes; right: Critical hub diameter, both modified from [7]

The left side of figure 2.10 shows a flow exiting the stator cascade with a swirl of $rc_{4\theta}$ and the corresponding flow angle α_4 . Because of the swirl the flow cannot fill

the annular space spanned from hub ($\varnothing d_h$) to shroud ($\varnothing d_o$) and a dead water core of diameter $\varnothing d_c$ develops. The graph on the right side of figure 2.10 depicts the critical diameter ratio d_c/d_o at which the separation takes place. If, for a certain flow angle, d_h/d_o falls below the curve, flow separation at the hub and subsequently a formation of hub dead water has to be expected.

A detailed explanation of the underlying flow phenomena as well as a derivation of the correlation presented in figure 2.10 can be looked up in [7, 47].

2.4 Computational Fluid Dynamics

2.4.1 Navier-Stokes equations

Every fluid flow within a control volume (CV) can be described explicitly by the Navier-Stokes equations (NSE) in their full form, which consist of the *conservation of mass*

$$\frac{\partial}{\partial t} \int_V \rho \, dV + \int_{\partial V} \rho \vec{c} \cdot d\vec{A} = 0 \quad (2.41)$$

the *conservation of momentum*⁵

$$\frac{\partial}{\partial t} \int_V \rho \cdot \vec{c} \, dV + \int_{\partial V} \rho \cdot (\vec{c} \otimes \vec{c}) \cdot d\vec{A} = \int_V \nabla \cdot \mathbf{T} \, dV + \int_V \rho \vec{f} \, dV \quad (2.42)$$

and the *conservation of energy*. \mathbf{T} is the stress tensor, \vec{f} the vector of body forces, V the volume and ∂V the surface of the CV. In order to describe the fluid model, an equation of state is needed. A detailed derivation of these equations can be found in [37]. The problem with this set of equations is that an analytical solution can only be found for specific problems. To overcome this challenge, the field of Computational Fluid Dynamics (CFD) was established. It provides numerical solutions of the NSE for complex flow problems.

In most engineering applications the flow regime is turbulent, hence its quantities such as pressure and velocity show a time dependent, fluctuating behaviour. Solving the NSE for such a flow is computationally expensive. Fortunately only the time-

⁵In some literature only the balance of momentum is referred to as Navier-Stokes equation.

averaged quantities are of interest if you want to determine the global characteristics of turbomachines. Therefore, the computationally much less expensive Reynolds-averaged Navier-Stokes equations (RANS) can be applied. The basic idea behind RANS is, that for a statistically steady flow every variable ϕ can be written as a sum of a time-averaged value $\bar{\phi}$ and a fluctuation ϕ' about that value [20]:

$$\phi(\vec{x}, t) = \bar{\phi}(\vec{x}) + \phi'(\vec{x}, t) , \quad (2.43)$$

where

$$\bar{\phi}(\vec{x}) = \lim_{T \rightarrow \infty} \frac{1}{T} \int_0^T \phi(\vec{x}, t) dt , \quad \overline{\phi'} = 0 . \quad (2.44)$$

All linear terms in the NSE are replaced by their time-averaged quantity in the RANS equations, the quadratic terms, however, yield the so called *Reynolds stresses* $\overline{\rho u'_i u'_j}$ ⁶. The Reynolds stresses cannot be expressed uniquely in terms of flow quantities which means that the achieved conservation equations are not closed anymore [49]. Closure requires an approximation of the Reynolds stress tensor which is attained by turbulence models.

2.4.2 Shear-Stress Transport model

In the past a wide variety of turbulence models has been developed. For many technical flows two-equation eddy viscosity models deliver the most reliable results. In these models the stress tensor is modelled as proportional to the mean strain-rate tensor with the eddy viscosity being the factor of proportionality [8]. The most widely known two-equation eddy viscosity model is the *k- ϵ model* by Launder, in which the eddy viscosity is characterized by the turbulent kinetic energy k and its rate of energy dissipation ϵ . It offers good results for free-shear-layer flows, but has its weaknesses with adverse pressure gradients present in blade passages of pumps and compressors. The *k- ω model* by Wilcox defines the eddy viscosity in terms of turbulent kinetic energy k and specific rate of dissipation ω . In contrast to the *k- ϵ model* it does not require wall-damping functions, thus being advantageous in the near-wall flow regime. However, the *k- ω model* is susceptible to freestream turbulence [8]. In 1994 Menter [43] introduced the *Shear-Stress-Transport model*

⁶ $(i, j) = (x, y, z)$

(*SST*) to combine the advantages of the $k-\varepsilon$ model in free-stream and the $k-\omega$ model near the boundary layer. This is achieved by superposing a modified formulation of the $k-\varepsilon$ model to Wilcox's $k-\omega$ model by means of a blending function. The original Wilcox model is activated in the near wall region, and the standard $k-\varepsilon$ model in the outer wake region and in free shear layers. Because of its superior performance over both prior models the *SST*-model with automatic selection of wall functions [2] has become the industry standard for steady state simulations of hydraulic machinery. Thus it was employed for the simulations conducted in this thesis. The selection of the wall functions depends on the actual y^+ value of the cell.

$$y^+ = \frac{\rho \Delta y u_\tau}{\mu} \quad \text{with} \quad u_\tau = \sqrt{\frac{\tau_w}{\rho}}. \quad (2.45)$$

y^+ is the dimensionless distance from the wall, Δy the actual distance, u_τ the friction velocity, τ_w the wall shear stress, ρ the density of the fluid and μ its dynamic viscosity.

2.4.3 Uncertainty estimation

An important step to assess the quality of CFD simulations besides comparing them to measurements is to calculate the uncertainty due to discretization. The recommended method for discretization error estimation is the *Grid Convergence Method (GCI)* presented by Celik et al. [14], which stems from a systematic development of the Richardson Extrapolation and is summarized in the following paragraphs.

GCI recommends to use three grids (1, 2, 3) of different sizes (*fine, medium, coarse*), so that the grid refinement factor

$$r = \frac{h_{coarse}}{h_{fine}} > 1.3 \quad (2.46)$$

becomes greater than 1.3. For computing the grid refinement factor the calculation of the average cell height h is required:

$$h = \left[\frac{1}{N} \sum_{i=1}^N (\Delta V_i) \right]^{1/3} \quad (2.47)$$

This yields

$$r_{21} = \frac{h_2}{h_1}, \quad r_{32} = \frac{h_3}{h_2} \quad \text{with} \quad h_1 < h_2 < h_3$$

In the next step the user of GCI has to run simulations for the three grids and define key variables (e.g. ϕ) important to the objective of the simulation study. Then the order p of the method can be achieved by the expressions

$$p = \frac{1}{\ln(r_{21})} \cdot \left| \ln \left| \frac{\varepsilon_{32}}{\varepsilon_{21}} \right| + q(p) \right| \quad (2.48a)$$

$$q(p) = \ln \left(\frac{r_{21}^p - s}{r_{32}^p - s} \right) \quad \text{with} \quad s = 1 \cdot \text{sgn} \left(\frac{\varepsilon_{32}}{\varepsilon_{21}} \right) \quad (2.48b)$$

and the abbreviations

$$\varepsilon_{21} = \phi_2 - \phi_1, \quad \varepsilon_{32} = \phi_3 - \phi_2.$$

Negative values of s are an indication of oscillatory convergence. In addition Eça and Hoekstra [19] define the discriminating ratio $R = \frac{\varepsilon_{21}}{\varepsilon_{32}}$ and distinguish four cases

1. $0 < R < 1$ for Monotonic convergence
2. $R > 1$ for Monotonic divergence
3. $R < 0 \wedge |R| < 1$ for Oscillatory convergence
4. $R < 0 \wedge |R| > 1$ for Oscillatory divergence

The extrapolated value for the key variable ϕ results in:

$$\phi_{ext}^{21} = \frac{r_{21}^p \phi_1 - \phi_2}{r_{21}^p - 1}, \quad \phi_{ext}^{32} = \frac{r_{32}^p \phi_2 - \phi_3}{r_{32}^p - 1} \quad (2.49)$$

Finally the approximated relative error e_a and the extrapolated relative error e_{ext}

$$e_a^{21} = \left| \frac{\phi_1 - \phi_2}{\phi_1} \right|, \quad e_{ext}^{21} = \left| \frac{\phi_{ext}^{21} - \phi_1}{\phi_{ext}^{21}} \right| \quad (2.50)$$

as well as the Grid Convergence Index (GCI)

$$GCI_{fine}^{21} = \frac{1.25 \cdot e_a^{21}}{r_{21}^p - 1} \quad (2.51)$$

are obtained.

The discretization uncertainty corresponds to the maximum value of the Grid Convergence Index for the designated key variable $GCI(\phi)$ and should be kept as low as possible.

2.5 Optimization

In their reference book on optimization and computational fluid dynamics [55], Thèvenin and Janiga present the following definition for optimization

*Optimization = the design and operation or process to make
it as good as possible in some defined sense*

which is a slightly extended version of what a typical dictionary would say. Originally, optimization in computational fluid dynamics (CFD-O) was only a peripheral area in the academic research of fluid-flow machinery because the computations required to provide sufficient input data for the actual optimization were overly costly. Thus, problem size was extremely limited. The first applications of CFD-O can be found in aerospace engineering, where they were used for shape optimization of wing profiles [55]. However, with increasing performance of numerical simulation methods and computational speed, the number of CFD-O related publications has risen enormously. Today the usability of CFD-O has advanced so far that even small hydraulic machinery manufacturers without huge resources for research and development can profit from introducing this technique in their design process. Several software developing companies offer toolboxes or add-ons with optimization features. The two most prominent exponents for turbomachinery applications are the *DesignXplorer* module within *ANSYS Workbench 18.2* and the *Minamo Optimization Kernel* within *NUMECA's Fine/Design3D* package. Although computational costs are still an issue, and will be in the next century, a series of publications by Kim et al. [34, 35] as well as by Liu et al. [39] and Höller et al. [28] have shown the huge potential of CFD-O in pump design. Whereas Kim et al. used a Radial Basis Neural Network architecture (RBNN), Liu et al. developed their own optimization scheme based on Narasimhan's ultra-transfer approximation method and Höller et al. utilized the Multi-objective Genetic Algorithm (MOGA) that is implemented in *ANSYS Workbench*. Despite the entirely different

approaches, all the three authors have achieved their respective optimization target of maximising the overall efficiency of their machines. This is a clear indication for the effectiveness of modern optimization algorithms. The following paragraphs, therefore offer an introduction into the *Response Surface Optimization* method that has been applied in this thesis. It consists of the three segments: the Design of Experiments, the Response Surface generation and the actual Optimization. One of the major benefits of this method is, that once the Response Surface has been built, changing the optimization criteria and re-running is almost costless [4].

2.5.1 Design of Experiments

Design of Experiment (DOE) refers to the process of planning an experiment so that the appropriate data, when analyzed by statistical methods, result in valid and objective conclusions [56]. Practically spoken, the purpose of a DOE is to gather a representative set of data to compute a Response Surface (RS) and then run an optimization [4]. The aim of the DOE is to gain maximum insight into the design by using the fewest number of points.

When choosing a type of DOE, three main aspects must be considered [41]:

1. The number of design variables (i.e., domain space dimension)
2. The effort of a single experiment
3. The expected complexity of the objective function (OF)

In this thesis the *Optimal Space-Filling* design (OSF) which is an optimized form of *Latin Hypercube Sampling* (LHS) was chosen for DOE. In the following paragraph, both algorithms will be presented briefly according to *ANSYS DesignXplorer* User's Guide [4].

The LHS algorithm is an advanced form of the Monte Carlo sampling method. The points are randomly generated in a square grid across the design space, but no point shares a row or column of the design space with any other point [4]. Optimal Space-Filling design incorporates LHS, but adds an optimization process to it, so that the distance between adjacent points becomes a maximum. Therefore OSF achieves a more uniform distribution of points across the design space, whereas LHS tends to clustering (see figure 2.11). This makes OSF the recommended choice in case the number of design points has to be kept low. A drawback is that the

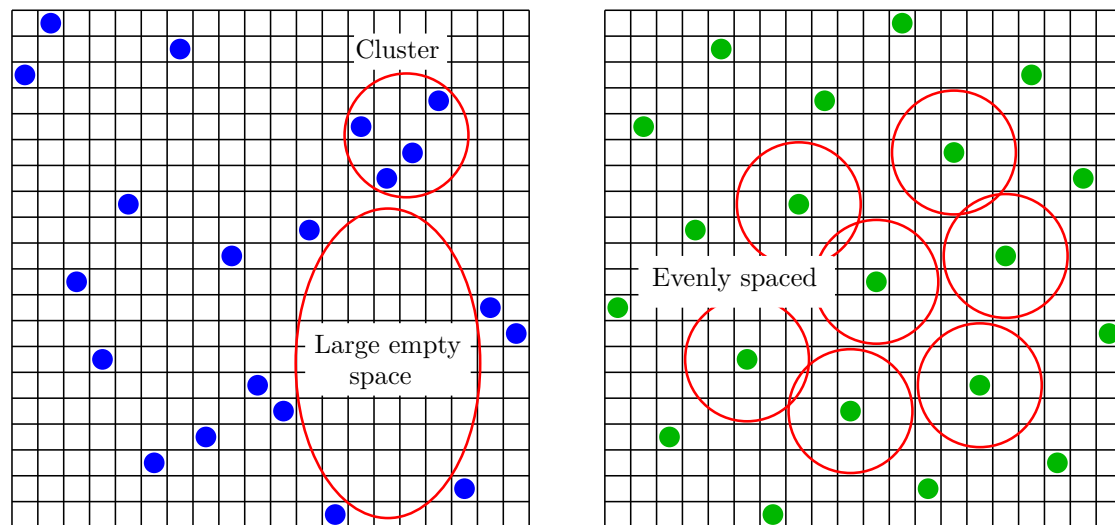


Figure 2.11: left: Latin Hypercube Sampling; right: Optimal Space-Filling, both showing 20 design points for two input parameters, modified from [4]

extremes of the design space are not necessarily covered, so the response prediction may be inaccurate at its boundaries.

2.5.2 Response Surface Method

Response Surfaces⁷ are functions of varying nature in which the output parameters are described in terms of the input parameters. Built from the DOE, they quickly provide the approximated values of the output parameters throughout the design space without having to perform a complete solution [4]. The quality of a response surface can be assessed by three criteria:

1. Accuracy - How does it fit the DOE points?
2. Validity - How big is the difference between predicted and observed values of the output parameters?
3. Smoothness - How close is it to the linear model?

All the three factors largely depend on the number of points in the DOE. The

⁷Often used synonyms for RS are surrogate model or meta model, although surrogate model is a general term for the whole group of models, whereas response surface is an example of a surrogate model.

complexity of the variations of the solution and the response surface type are of further influence.

If little is known about the relationship between input and output parameters of the DOE, the *Genetic Aggregation* algorithm (GenAgg) is a good choice, as it builds the response surface type that is the most appropriate approach for each output [4]. First of all, the GenAgg generates populations of different response surfaces based on five RS-types⁸, which are solved in parallel. Each of these response surfaces is evaluated by fitness functions in order to determine which one yields the best approach. The fitness functions take into account both, the quality (in terms of smoothness) and the stability (through cross-validation) of the generated RS. If one of the response surfaces meets the quality requirements, the GenAgg stops. Otherwise, the existing population has to pass through a number of cross-over and mutation steps until a new population of response surfaces can be created by means of reproduction from the parent generation (= already existing RS). The newly achieved population is then evaluated again. The process of evaluation and reproduction continues, until the user-defined quality requirements are met or a maximum number of iterations is reached [4].

2.5.3 Optimization

As cited at the beginning of section 2.5, in terms of engineering, optimization means to make something as good as possible. Transferred to a more mathematical way of thinking, the target of optimization is to find a global extremum (minimum or maximum) of a functional relation that satisfies all constraints of the underlying problem. Such a relation is called *Objective Function*(OF). In one-dimensional space this can be done pretty easily by curve sketching. For more complex problems with a higher-dimensional input parameter space (= design space), especially with multi-objective or multidisciplinary problems, individual OFs may be assembled to a global objective function (GOF) that is basically a weighted (w_i) sum of the individual OFs f_i :

$$GOF = \sum_i w_i \cdot f_i \quad (2.52)$$

⁸Full 2^{nd} order Polynomial, Non-Parametric Regression, Kriging, Moving Least Squares and Linear Basis Function [4]

Then finding an extremum becomes a challenge. Therefore a vast variety of optimization algorithms have been established. Some of the most prominent ones belong to the groups of *Sequential Quadratic Programming* methods (SQP), *Adjoint* methods and *Evolutionary Algorithms* (EA) [55]. In this thesis the *Multi-objective Genetic Algorithm* (MOGA), which is fully implemented within *ANSYS DesignXplorer*, has been applied. It is the recommended option for computing global maxima/minima, whereas other algorithms, such as SQP tend to fall into local instead of global optima [4].

Multi-objective Genetic Algorithm

Multi-objective Genetic Algorithms are related to the group of Pareto-based approaches for multi-objective problems. The specific type of MOGA used in goal-driven optimizations within *ANSYS DesignXplorer* is a hybrid variant of the popular *Non-dominated Sorted Genetic Algorithm-II* (NSGA-II) based on controlled elitism⁹ concepts [4]. It actually belongs to the second generation of Pareto-based approaches. In the following passages, the main concepts inherent to multi-objective genetic optimization will be presented.

Pareto dominance

In multi-objective optimization it is very common that two or more objectives stand in conflict to each other¹⁰. This implies, that there is not a single combination of input parameters, that optimizes all the objectives simultaneously, but that there exists a whole set of possible solutions of equivalent quality [41]. A combination of N input parameters (labelled as *individual* in EA jargon) is expressed by the parameter vector $\vec{x} = (x_k)$ with $k = 1, 2, \dots, N$. It can be said that *individual A* (\vec{x}_A) *dominates individual B* (\vec{x}_B) if and only if:

$$(\forall i : f_i(\vec{x}_A) \geq f_i(\vec{x}_B)) \cap (\exists j : f_j(\vec{x}_A) > f_j(\vec{x}_B)) , \quad (2.53)$$

⁹Elitism refers to the use of an external population to keep track of non-dominated individuals [41]

¹⁰E.g., a pointed leading edge of a pump impeller may allow for maximum efficiency at zero incidence (BEP), but will suffer from extensive shock losses at off-design points.

f_i being the i -th objective function¹¹ [41]. Expressed in words, equation (2.53) states that individual A dominates individual B , if for at least one of the objectives f_i A is strictly better adapted than B and if, for all other objectives, A is not worse than B [33]. Based on the evaluation of equation (2.53) every individual I is assigned a rank

$$\text{rank}(I) = 1 + J \quad (2.54)$$

within a group of M individuals based on how many individuals J it is dominated by. Non-dominated individuals therefore have rank 1, the maximum rank can be M . At the end of the EA, those individuals that have not been dominated¹² over all generations, form the so-called *Pareto-front* [33]. The Pareto-front has the dimension $L - 1$, L being the number of OF. Hence, if there are two OFs, e.g. efficiency vs. cavitation, the Pareto-front becomes a simple curve.

Basic idea of Genetic Algorithms

The *Genetic Algorithm* (GA), which belongs to the group of evolutionary algorithms has been adopted from living organisms in nature. Thus each individual can be seen as a DNA string [41] comprised of genes ($\hat{=}$ input parameters). Based on the initial population (= first generation of individuals that are created from the RS, also named samples), new generations of individuals(= offsprings) can arise through *Averaging*, *Cross-over* and *Mutation*. The process of evolution is depicted in figure 2.12 and will be described in the following paragraph.

Based on the fitness value¹³ of each individual, a selection operator chooses whether it will be promoted to the the next generation or not. The better the fitness, the higher the probability to be picked for the new population. The individuals with the highest fitness value are promoted directly without reproduction (= *Survival*). Their genes remain unchanged (left individual in the offspring generation of figure 2.12). Other selected individuals that are not promoted directly produce offspring through averaging and cross-over. In an individual that is created by averaging, the numerical values assigned to the genes are determined by forming some kind of mean value, depending on the actual algorithm. In the example shown in figure 2.12 the arithmetic mean was used. By contrast, cross-over is

¹¹This definition of Pareto-dominance is valid if the target is to maximise the OFs.

¹²Non-dominated individuals are also referred to as *Elite*.

¹³*Fitness* is the measure of how an individual fits the goal of an optimization [41].

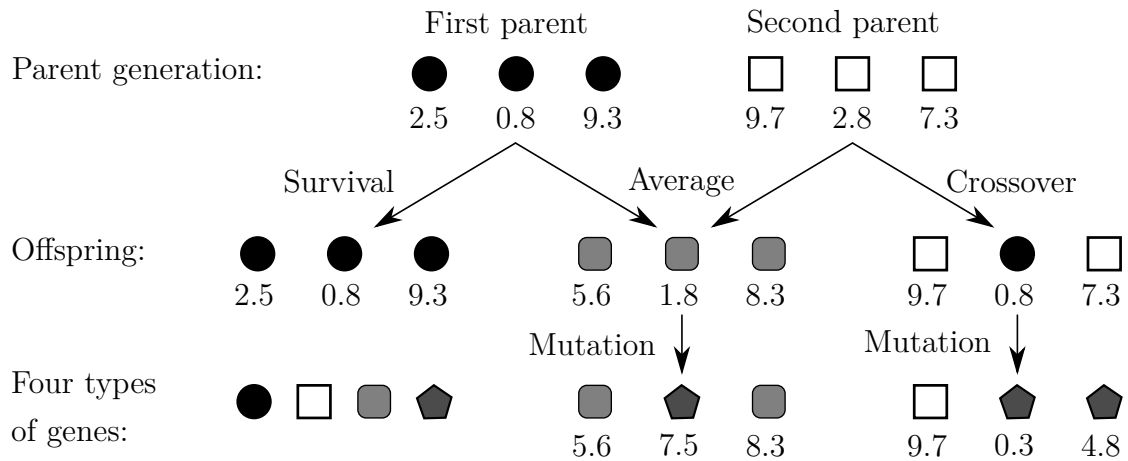


Figure 2.12: Principle of EA showing the procreation of offsprings from two parents, modified from [33]

a recombination between two parents whose genes are stochastically picked and re-assembled to form an offspring [41]. Finally, a mutation operator randomly substitutes genes of individuals to introduce diversity, to enhance the probability to explore untouched areas of the design space and to avoid premature convergence [33, 41]. Mutation helps GAs to avoid stagnating at any local optima [4].

Chapter 3

Reference configuration

This chapter gives an overview of the original mixed-flow pump model *PS550* by *Riva Calzoni SpA*, its main dimensions, the design point data and the performance characteristics. In addition, there is a section about the test rig and the model test configuration according to the model test report [48].

3.1 Model machine

The *PS550* model pump consists of an impeller with three blades and a diffuser with five vanes. The maximum diameter d_{2o} of the impeller is 379 mm. The radial gap of 0.15 mm between the impeller and the shroud results in a relative tip clearance t/d_{2o} of approximately $4 \cdot 10^{-4}$. Further main dimensions are depicted in figure 3.1 and listed in table 3.1. The specific speed n_q of the machine at BEP is 158.1 rpm. The flow coefficient ϕ_{BEP} and the head coefficient $\psi_{BEP, Ref, Test}$ of the model at the same operating point are 0.212 and 0.355 respectively, with a peak efficiency $\eta_{BEP, Ref, Test}$ of over 86%. The speed coefficient $\sigma_{BEP, Ref, Test}$ and the diameter coefficient $\delta_{BEP, Ref, Test}$ are 1.003 and 1.675. With these numbers the BEP of the pump lies exactly on the Cordier-line for pumps (figure A.2). The values of flow and head coefficient also coincide with the grid in the Cordier diagram. However, the blue marker indicating the position of the model pump lies distinctly to the right of the band for mixed-flow pumps. This clearly supports the approach of applying analytical criteria in the design process that have mainly been developed for axial-flow machines.

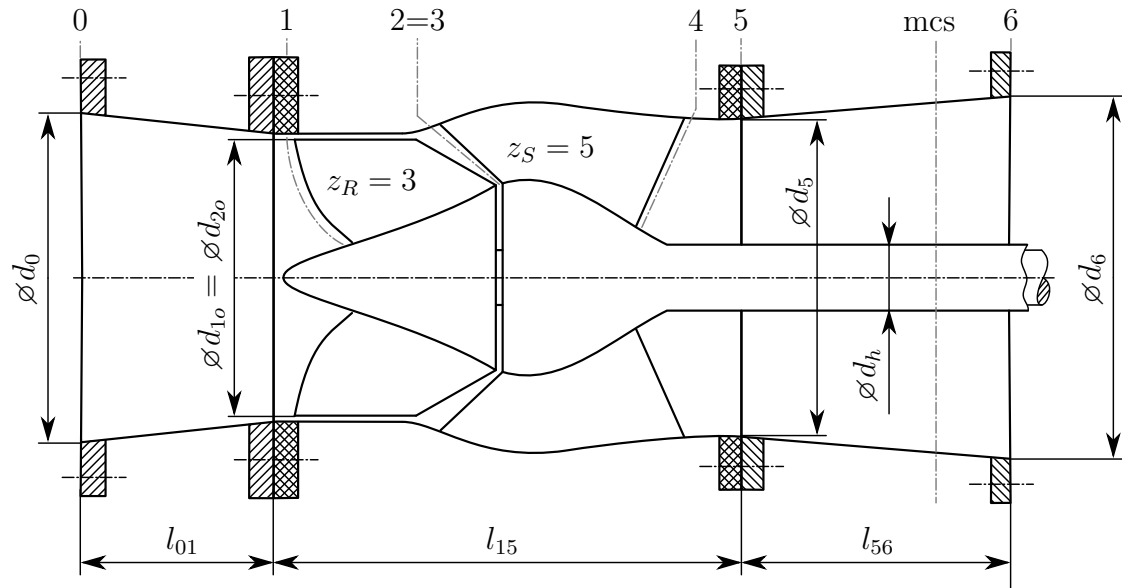


Figure 3.1: Meridional contour of the *PS550* model pump unit with main dimensions and calculation stations (0 - 6)

n	1000	rpm	z_R	3	-
ω	104.72	1/s	z_S	5	-
ϕ_{BEP}	0.212	1	$\sigma_{BEP, Ref, Test}$	1.003	1
$\psi_{BEP, Ref, Test}$	0.355	1	$\delta_{BEP, Ref, Test}$	1.675	1
d_0	430	mm	d_5	410	mm
d_{20}	379	mm	d_6	460	mm
d_h	82.5	mm	l_{15}	606	mm
l_{01}	245	mm	l_{56}	350	mm

Table 3.1: Model test data at the BEP and main dimensions

3.2 Test rig

The model tests were conducted at the hydraulic laboratories of Riva Calzoni SpA in Milan, Italy. A scheme of the closed hydraulic circuit is shown in figure 3.2. Exiting the tailwater vessel (1), which is used to provide an adequate pressure level for cavitation measurements, the fluid passes a 90° inlet elbow (2) before it enters the pump unit (3). This pump unit consists of a short, convergent inlet

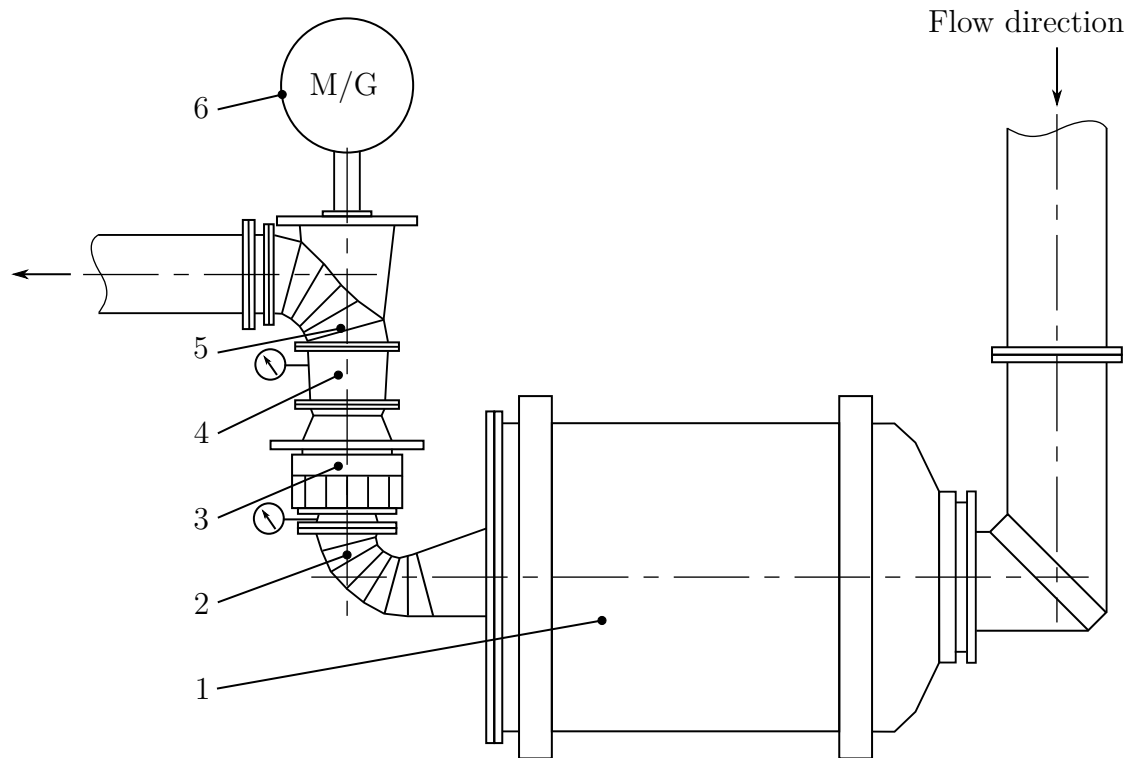


Figure 3.2: Hydraulic circuit scheme: 1 tailwater vessel, 2 inlet elbow, 3 pump unit, 4 annular diffuser, 5 outlet elbow, 6 motor/generator unit

section, the impeller and the vaned diffuser. Details of the meridional contour can be assessed from figure 3.1. It is followed by a short annular diffuser (4) and a 90° outlet elbow (5). The pump is powered by a motor/generator unit (6). According to drawings of the test rig and the model test report, pressure gauges have been installed in the diffuser section and the inlet section, the flow rate was measured by a venturi meter. In the diffuser section the gauges were installed 100 mm upstream of calculation station 6, labelled as measurement cross-section (mcs) in figure 3.1.

3.3 Model test data

Figure 3.3 depicts the performance characteristics of the pump model *PS550*. Measurements were taken from approximately $50\% \phi_{BEP}$ to $133\% \phi_{BEP}$. The model shows a smooth head curve without any instability or saddle in its designated operating range. The shape of the measured head and power curves are very similar to the typical characteristics of pumps of such a specific-speed (presented in

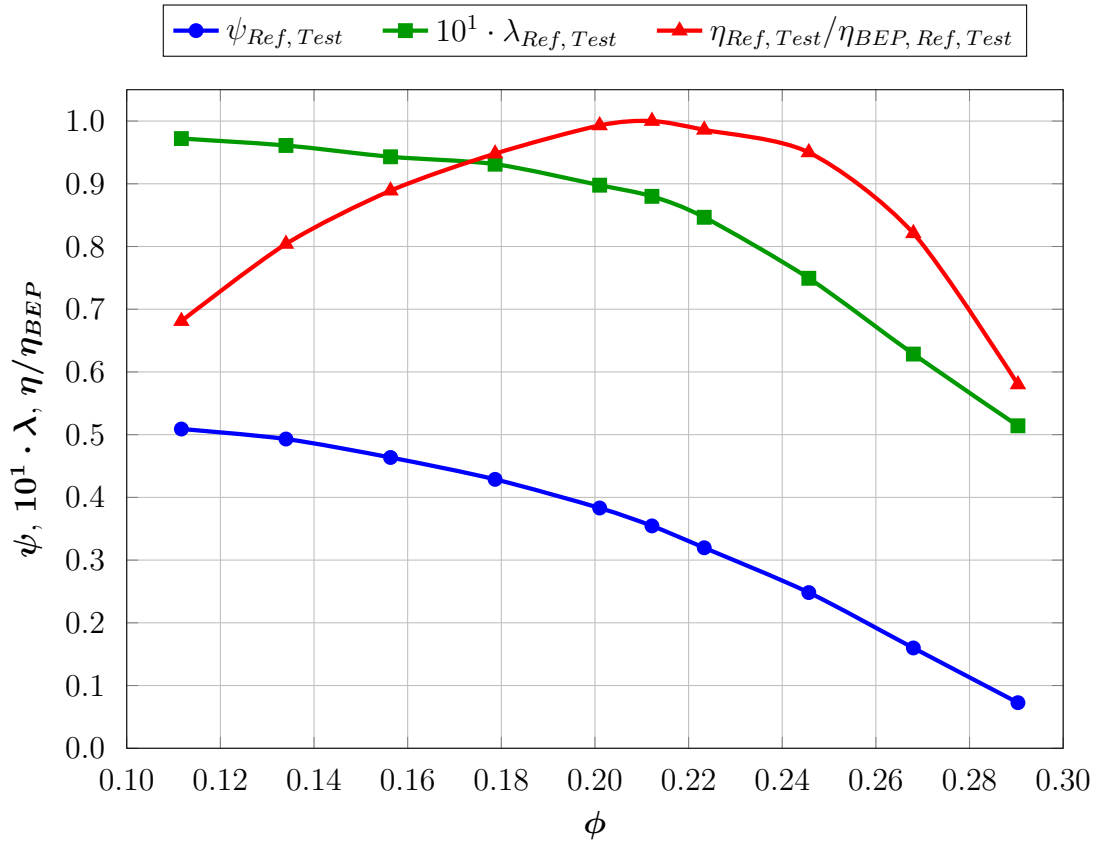


Figure 3.3: Performance curves of mixed-flow pump *PS550*, acquired from the model test report [48]

figure 2.3). As mentioned before, the peak efficiency of the reference configuration of the pump lies just above 86 %, whereby in part-load and overload, the efficiency does not fall below 80 % of its peak value within a range of $0.63 \leq \phi / \phi_{BEP} \leq 1.25$. Measurement results of the cavitation behaviour were also included in the model test report [48]. Although assessing cavitation was not a major part of this thesis, at least one conclusion that can be drawn from those measurements is that cavitation free operation is provided between $0.75 \leq \phi / \phi_{BEP} \leq 1.15$, in case the intake reservoir is located at the same geodetical height as the impeller. If operation outside these boundaries is taken into account, the pump has to be mounted deeper than the reservoir to provide enough supply pressure. Unfortunately, the model test report omitted any detail on the measurement procedure or the instruments. Thus an estimation of the measurement uncertainty was not possible.

Chapter 4

Simulation setup

All simulations presented in this thesis were conducted by modules included in the commercial multi-purpose simulation software package *ANSYS Workbench 18.2*. At first the original geometry of the *PS550* model pump was rebuilt in *Solid Edge ST8* and then imported into *ANSYS DesignModeler*. There, the blade contours were detailed using the *BladeEditor* features. The meshes for the rotor and stator component were created in *TurboGrid*, those for the outlet elbow in *ANSYS Meshing*. The simulation set-up and the boundary conditions were defined in *CFX-Pre*, while the flow equations were solved by means of the *CFX-Solver*. Post-Processing was executed mostly within the Turbo workspace of *CFD-Post*.

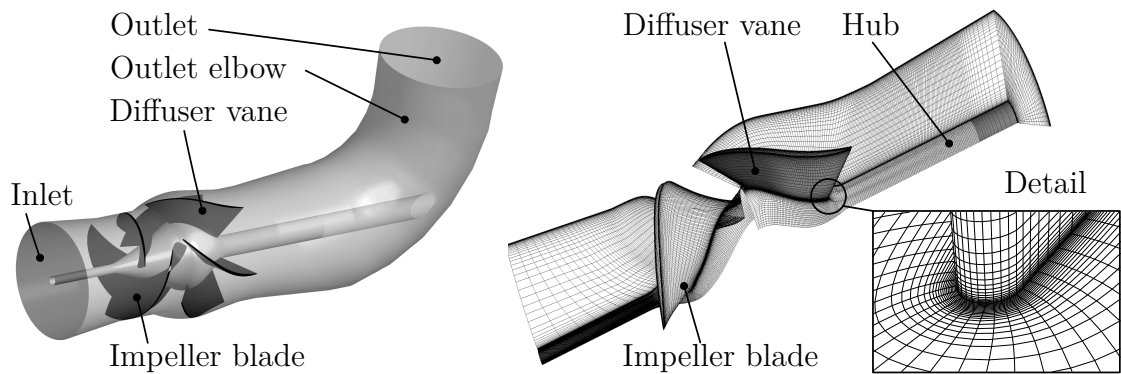
4.1 Computational domain

The computational domain was divided into five main segments:



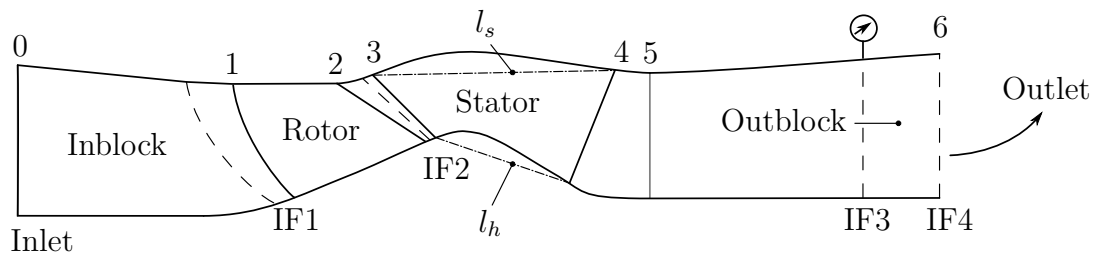
For the first four segments only one passage was taken under consideration, whereby for the outlet elbow the full 360° model was simulated. All segments except for the rotor were set stationary. Figure 4.1 shows the 3D model of the flow region, its different domains and the mesh. The solid lines in part c) of these figure represent the rotor and stator blade leading and trailing edges. Positioned slightly

before the LE and after the TE there are the calculation stations 1 to 4. The dashed lines indicate the positions of the interfaces between inblock and rotor (IF1), rotor and stator (IF2), stator and outblock (IF3) and outblock and outlet elbow (IF4). According to the model test pressure gauges were installed 100 mm upstream of the beginning of the outlet elbow, thus an additional interface IF3 in the stationary component downstream the vaned diffuser had to be inserted. The original outlet-elbow was included in the CFD-model to allow for a location of the outlet boundary far downstream the measurement position (IF3). This provided the evaluation of the flow quantities at IF3 to be widely unaffected by the selection of the outlet boundary constraints. The radial gap between rotor blades and shroud was not included in the model as the number of cells needed in the blade tip region to precisely capture tip leakage vortices would significantly increase the grid size¹. This could not be allowed in order to keep the simulation model feasible for optimization.



a) Mixed flow pump model

b) Mesh of rotor and stator



c) Meridional contour and interfaces

Figure 4.1: a) 3D model of the mixed flow pump; b) mesh of rotor and stator; c) meridional contour with interfaces and calculation stations (0 - 6)

¹Zhang et al. [60] needed up to about $6.6 \cdot 10^6$ mesh nodes in their study of an axial flow pump.

4.2 Boundary conditions and numerical scheme

The type of the flow analysis was set to steady state with water as working fluid which was treated as incompressible. A change of temperature was not considered in the simulations. The reference pressure for the domain was fixed at 100 000 Pa. Boundary conditions were chosen according to best practices recommended in [3]. While at the inlet the total pressure option with a relative pressure of 0 Pa and medium turbulence intensity was selected, the total mass flow rate with unconstrained pressure shape option was imposed at the outlet. All solid surfaces were defined as smooth, no slip walls. Stationary segments of the domain were coupled by means of general grid interfaces (GGI), whereas for IF1 and IF2 the stage (mixing-plane) frame change model with constant total pressure option was applied. The flow between adjacent passages was set to be periodic in the direction of rotation. Turbulence treatment was conducted by Menter's Shear Stress Transport model with automatic wall function processing. The characteristics of the SST-model were summarized in section 2.4.2. The three-dimensional steady-state incompressible RANS equations were solved by means of a second order accurate advection scheme (high resolution) that computes the blend factor for each node as close to one as possible [2]. A first order upwind differencing scheme was used to interpolate the turbulence transport. The time scale option was set to automatic which resulted in a physical time scale of $0.1/\omega$. Due to slow convergence behaviour, the maximum number of iterations was set to 3000 to ensure an acceptably converged solution. For more details of the simulation setup see tables 4.1 and 4.2.

Calculation of integral quantities is carried out by area (denoted by $\bar{\phi}$) and mass flow averaging (denoted by $\hat{\phi}$), whereby the variable ϕ is a place holder. For convective quantities, which are transported along with the flow (e.g. momentum, total pressure, ...) mass flow averaging is applied, for quantities not transported with the flow (e.g. static pressure) area averaging is used.

$$\bar{\phi} = \frac{\int_{\vec{A}} \phi \cdot d\vec{A}}{\int_{\vec{A}} d\vec{A}} \quad \hat{\phi} = \frac{\int_{\vec{A}} \rho \vec{c} \cdot \phi \cdot d\vec{A}}{\int_{\vec{A}} \rho \vec{c} \cdot d\vec{A}} \quad (4.1)$$

In the following, for the sake of convenience the superscripts $\bar{\quad}$ and $\hat{\quad}$ will be omitted.

Property	Settings	Options
Advection scheme	High resolution	
Turbulence numerics	First order	
Timescale control	Automatic timescale with conservative length scale	timescale factor 1.0
Convergence criteria	root mean square value of residuals	target = $1 \cdot 10^{-6}$
Maximum number of iterations	3000	

Table 4.1: Basic settings for the solver control

Property	Settings	Options
Analysis type	Steady state	Incompressible
Fluid	Water at 20 °C	$\rho = 998.2 \text{ kg/m}^3$, $p_v = 2339 \text{ Pa}$ [29]
Reference pressure	100 000 Pa	
Turbulence treatment	SST-model with automatic wall functions	
Inlet	Total pressure (stable), normal to boundary	Relative pressure 0 Pa, medium turbulence intensity
Outlet	Mass flow rate	Pressure shape unconstrained
Hub, shroud and blades (if stationary)		
Hub, blade of rotor	Smooth, no slip wall	Rotating
Shroud of rotor		Counter rotating
Periodic interfaces	Rotational periodicity around z-axis	GGI
Stationary interfaces without frame change	General connection, no frame change model	GGI
Rotor-Stator interface	General connection with stage mixing model	Constant total pressure, pitch ratio: $z_S/z_R = 5/3$

Table 4.2: Boundary conditions and interface definitions

4.3 Validation

The results of the numerical simulations were evaluated by a grid independence study and a comparison of the computed performance characteristics to the model test data. The grid independence study was executed according to the GCI method of Celik et al. [14] in order to assess the discretization error. The theoretical background for the application of this method is summarized in section 2.4.3. Three different sets of meshes with an overall number of cells of approximately 390 000 (coarse, subscript 3), 1 100 000 (medium, subscript 2) and 3 300 000 (fine, subscript 1) were tested. The meshes consist of a rotor (including the inblock) and a stator (including the outblock) domain and an outlet elbow, which account for approximately 50 %, 40 % and 10 % of the cells, respectively. For each mesh the size of the cells adjacent to the walls was kept constant to provide for similar values of y^+ . Only the number of cells in between two walls was altered. In compliance with the automatic wall treatment of the SST-turbulence model an average value for y^+ of around 15 was achieved for all three meshes. As the contribution of the outlet elbow to the upstream flow field is negligible, the elbow was meshed relatively coarse compared to the rotor and the stator segments. Moreover, a higher value of up to 40 was tolerated for the mean of y^+ . A detailed listing of the mesh data for the rotor and the stator domain as well as for the outlet elbow is provided in tables A.1 to A.3.

The key variables chosen for the estimation of the discretization error were the head coefficient ψ , the power coefficient λ and the efficiency η . Their respective values for the three tested grid sizes are shown in table 4.3. The results of the uncertainty error estimation are summarized in table 4.4, full results are given in table A.4.

	Model test	Coarse (3)	Medium (2)	Fine (1)
ψ	0.355	0.330	0.350	0.346
$\eta/\eta_{Ref, Test}$	1.000	0.988	1.006	0.989
λ	$8.800 \cdot 10^{-2}$	$8.194 \cdot 10^{-2}$	$8.542 \cdot 10^{-2}$	$8.575 \cdot 10^{-2}$

Table 4.3: Values of head coefficient, power coefficient and efficiency of the three tested meshes compared to model test values

	ψ	$\eta/\eta_{Ref, Test}$	λ
r_{21}	1.453		
r_{32}	1.400		
R	-0.220	-0.949	0.095
p	4.413	0.148	7.066
e_{ext}^{21} in %	0.305	41.560	0.030
GCI_{fine}^{21} in %	0.380	36.698	0.037

Table 4.4: Summary of quantities calculated by the GCI method

The convergence ratio of the head coefficient and of the efficiency lies below zero which indicates an oscillatory convergence of these two quantities. The convergence ratio of the power coefficient is slightly greater than zero, thus being a sign of monotonic convergence. The values of the order p of the method as well as the values of the Grid Convergence Index GCI_{fine}^{21} for the fine solution prove the assumption that the head coefficient and the efficiency show oscillatory convergence, compared to the monotonic convergence behaviour of the power coefficient. Their extrapolated errors e_{ext}^{21} and Grid Convergence Indices are well below 1%. However, one must admit that the order p of the efficiency is very low, thus the extrapolated error as well as the Grid Convergence Index are very high. A possible reason for this characteristic lies in the oscillatory convergence of the simulation itself which is caused by the massive turbulences downstream the stator. A further discussion of the flow in the stator will be given in chapter 5. Bamberger [6] encountered a comparable situation when optimizing fans. He stated that in the case of oscillating convergence it is not possible to estimate the exact solution. Newer contributions to the estimation of numerical uncertainty, e.g. Eça and Hoekstra [19], are based on the assumption that for such cases with anomalous behaviour the GCI method cannot be applied in its strict sense. Therefore, for further validation of the numerical setup used in this thesis the results of the simulation of the medium mesh were compared to the model test (figure 4.2). The comparison shows that the simulation data generally are in good agreement with the test results for flow coefficients of approximately 0.15 to 0.25 ($0.75 \leq \phi/\phi_{BEP} \leq 1.15$). In operating points of low part-load or high overload unsteady flow phenomena such as recirculation occur. They cannot be captured precisely by the steady state approach presented in this thesis. In consequence the discrepancy between measurement and simulation becomes significantly larger at the boundaries of the operating range. This should

not be too much of a concern, as the focus of this work is to improve the performance of the pump near its original design point, where the simulation delivers satisfying results. On that account, the medium mesh was chosen for all further simulations, because it allows to keep an adequate balance between numerical accuracy of the solution and computational costs, which are highly depending on the grid size (for calculation times see table 4.5).

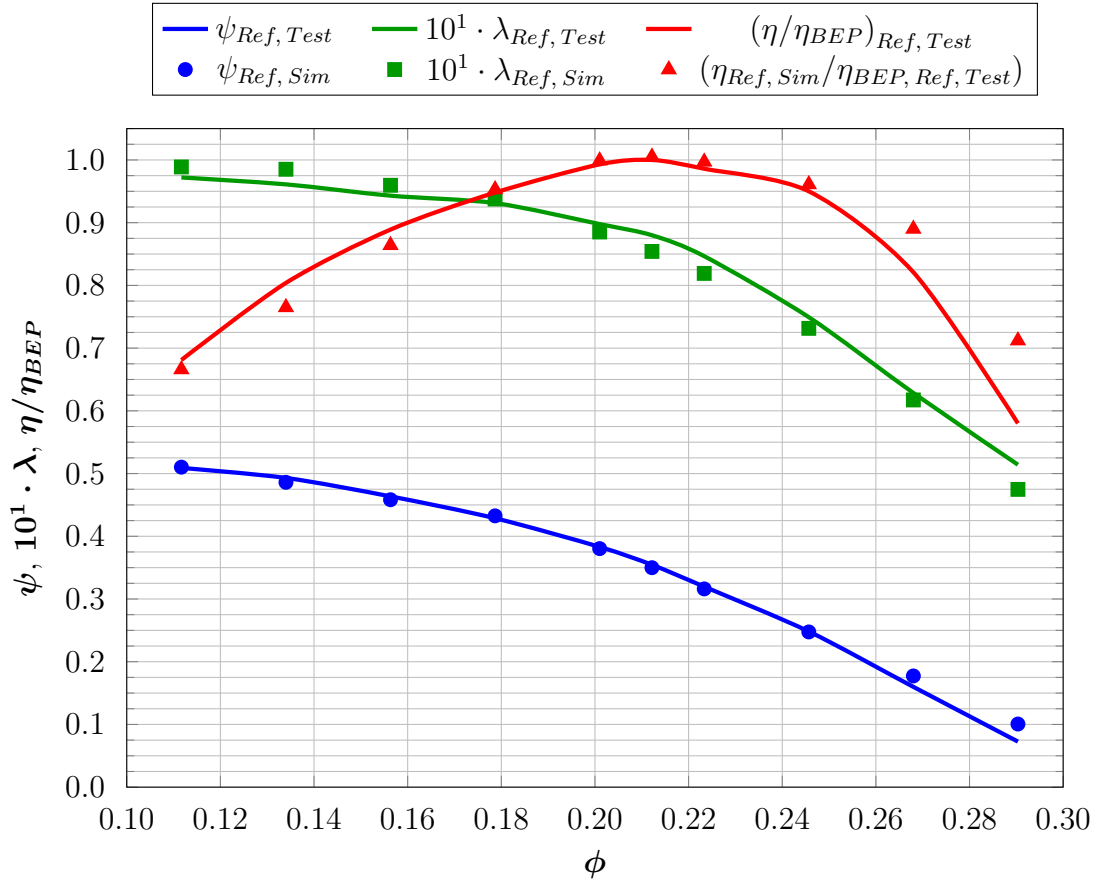


Figure 4.2: Comparison of model test data against simulation results of the medium mesh

	Coarse	Medium	Fine
Time in hh:mm	09:20	24:14	73:25

Table 4.5: Calculation times for the three different meshes on a workstation with Intel Xeon W3530 processor (quad-core, 2,80 GHz) and 24 GB RAM

Chapter 5

Flow in the vaned diffuser

This chapter is divided into three sections. First, the flow in the diffuser of the existing mixed-flow pump model *PS550* is analysed, numerically as well as by means of the criteria presented in section 2.3.2. Then the necessary design modifications are explained. In the third part of this chapter the most suitable design to overcome the weaknesses of the reference configuration is presented and compared to the existing diffuser. All simulations within this chapter were conducted for the BEP of the pump and for all of these simulations the original impeller design was used. All numerical values of the flow quantities used in this chapter are based on simulation data. For the sake of convenience, the subscript *Sim* is omitted in most figures and equations.

5.1 Assessment of the original diffuser

The simulation of the existing pump model revealed that this machine suffers from massive flow separation in the vaned diffuser. The separation starts approximately at the biggest diameter of the hub at the suction side of the vane and causes massive swirl in the flow downstream the stator, which is also the source for the hub dead water (marked in red in figure 5.1). Figure 5.2 shows that the separation bubble blocks around half of the outlet cross-section of the diffuser vanes and thus induces a severe deflection of the main flow towards the circumferential direction. Instead of swirl-free flow ($\alpha_{mcs} = 90^\circ$), an average flow angle of around 63° was computed at the measurement cross-section downstream the diffuser.

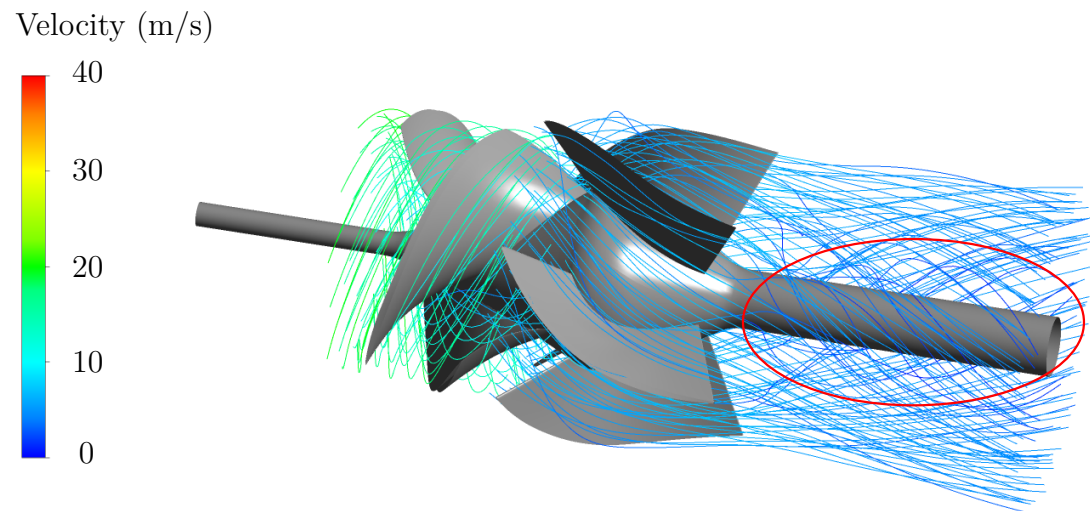


Figure 5.1: Streamlines (starting from the rotor inlet) in the existing pump model at BEP

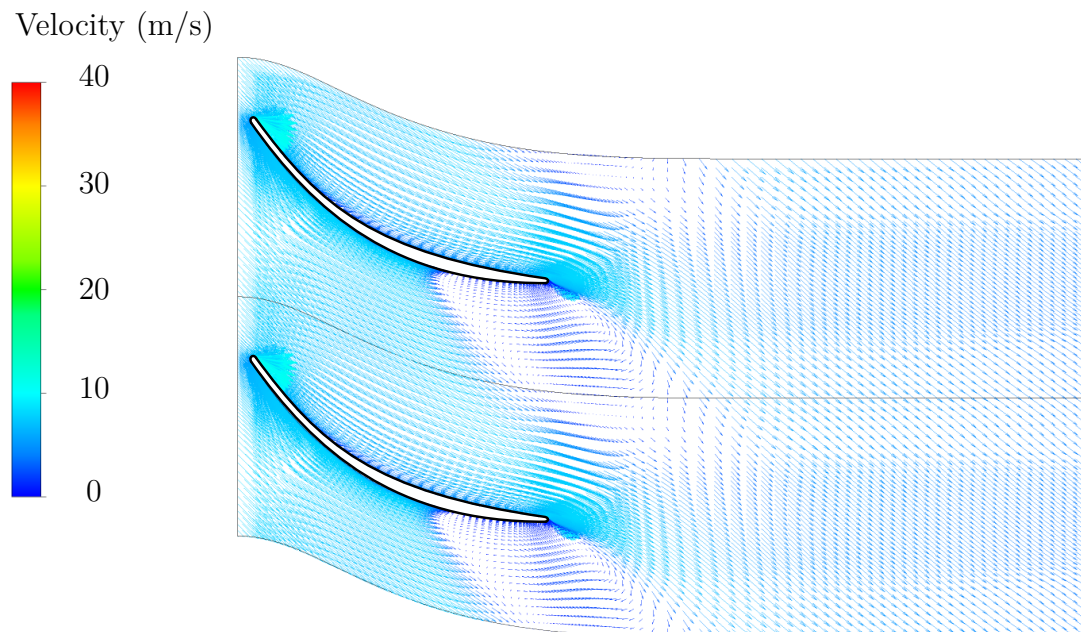


Figure 5.2: Velocity vectors in the diffuser of the existing pump model at BEP in a blade-to-blade projection at midspan, two passages shown

Furthermore, the left plot in figure 5.6 uncovers that the blade is adversely affected by negative incidence which usually is not expected at the BEP but in overload conditions. With a blade angle of $\alpha_{3B} = 33^\circ$ and a flow angle of $\alpha_3 = 46^\circ$ the

incidence i_S becomes -13° . In simulations at a low part-load of $\phi/\phi_{ref} < 2/3$ the flow approaching the stator leading edge was free of incidence. In other words, the stator may have been developed for a similar pump with lower flow rate and was not adapted thoroughly to this specific model.

Analytical criteria that are common in the design process of turbomachinery cascades have been consulted to prove the outcome of the simulations. A theoretical introduction to these criteria is given in section 2.3.2. First of all, it has to be noted that the simulated deflection angle $\theta = \alpha_4 - \alpha_3$ amounts to only about 15° instead of the desired 45° . This is a clear indication that the flow is unable to follow the blades smoothly, so separations¹ have to be expected.

De Haller's criterion from equation (2.37) applied to the diffuser cascade gives

$$\frac{c_4}{c_3} = \frac{c_{4m}}{\sin \alpha_{4B}} \cdot \frac{\sin \alpha_{3B}}{c_{3m}} = \frac{A_3 \cdot \sin \alpha_{3B}}{A_4 \cdot \sin \alpha_{4B}}, \quad (5.1)$$

in which $Q = A \cdot c_m$ and $\sin \alpha_B \simeq \alpha = c_m/c$ were taken for granted. With the numerical values for the blade angles and the diameter ratio $(A_4/A_3)_{Ref} = 1.117$ the evaluation of equation (5.1) at the hub (span = 0) yields

$$\frac{c_4}{c_3} = 0.471 < 0.55 \div 0.6, \quad (5.2)$$

thus de Haller's criterion is infringed and there is a reasonable suspicion that the blade loading is too high. In fact, the limits found by de Haller only allow for a deflection of approximately 30° for the stator geometry of the reference configuration. This means that with a given blade angle α_{3B} being slightly larger than 30° at the stator inlet, the corresponding blade angle at the outlet should not exceed 60° by far. However, the desired flow angle of $\alpha_4 = 90^\circ$, to obtain swirl-free flow at the outlet, requires a blade angle α_{4B} which should be marginally greater than that value.

A more severe evidence that the blade loading of the diffuser vanes of the reference configuration exceeds the limits can be received from Lieblein's formula for the diffusion factor as introduced in equation (2.40). For the stator cascade, this equation denotes as

$$D = 1 - \frac{c_4}{c_3} + \frac{1}{2\sigma} \frac{c_{3\theta} - c_{4\theta}}{c_3} \quad (5.3)$$

¹These separations are caused by high blade loading, which is accompanied by strong diffusion hurting the stability of the boundary layer of the suction side of the blade.

Span	α_{3B}	α_{4B}	l	s	σ	D
0.0	0.949	1.007	0.723	0.622	1.693	0.772
0.5	1.000	1.000	1.000	1.000	1.455	0.782
1.0	0.997	0.991	1.293	1.379	1.365	0.799

Table 5.1: Geometrical data of original stator cascade, scaled to quantities at midspan

and with the flow velocities expressed by geometrical quantities as

$$D = 1 - \frac{A_3 \cdot \sin \alpha_{3B}}{A_4 \cdot \sin \alpha_{4B}} + \frac{s}{2l} \left(\cos \alpha_{3B} - \frac{A_3}{A_4} \cdot \frac{\sin \alpha_{3B}}{\tan \alpha_{4B}} \right). \quad (5.4)$$

Again, $Q = A \cdot c_m$, $\sin \alpha_B \simeq \alpha = c_m/c$ and $\cos \alpha_B \simeq \alpha = c_\theta/c$ were taken for granted. The solidity σ was substituted by the chord length

$$l = \sqrt{\Delta x^2 + \Delta y^2 + \Delta z^2} \quad (5.5)$$

and the spacing

$$s = \frac{d\pi}{z_S} \quad (5.6)$$

of the diffuser vanes, which both, of course, vary from hub to shroud. As the spacing also varies between leading and trailing edge, arithmetic averaging of the respective values was chosen for evaluation of equation (5.4). The resulting diffusion factors are summarized in table 5.1. They exceed the limits of 0.45 at the shroud (span = 1) and 0.6 at the hub (span = 0) by far, which is another undoubtful indication of a too high blade loading of the original diffuser vanes.

As explained at the beginning of this section, the simulations show a massive dead water core at the hub downstream the stator (see also the perturbed velocity vectors in the top plot of figure 5.11). The reason for this dead water is the residual swirl in the flow behind the vanes. With a flow angle α of around 60° after the exit of the diffuser cascade and a diameter ratio d_h/d_5 of approximately 0.2, the original diffuser falls below the critical curve proposed by Bammert and Kläukens (blue marker in figure 5.12, section 5.3).

All three criteria, de Haller, Lieblein and Bammert and Kläukens, indicate that the stator geometry needs to be modified. As the blade angles are pre-determined by the flow exiting the rotor and the demand for swirl-free flow downstream the

pump stage, they cannot be altered except for adapting the blade angle at the leading edge to the incoming flow. Thus the only other options are to modify the meridional contour and the position of the trailing edge of the diffuser vanes.

5.2 Design modifications

The analysis of the reference configuration of the *PS550* mixed-flow pump unfolded three areas of the diffuser vanes that needed to be changed:

1. Blade angle α_{3B} of the leading edge
2. Axial length l_{ax}
3. Blade angle α_{4B} of the trailing edge

The adjustment of the blade angles is made to compensate the incidence at the stator inlet and to reposition the trailing edge according to design recommendations for swirl-free downstream as presented in section 2.3.2. Modifying the axial blade length tackles the separation problem. Equation (5.3) reveals that the main geometrical parameter to lower the diffusion factor (and thus the blade loading) is the solidity σ . If the solidity is raised, either by lengthening the blades or increasing the number of blades, the diffusion factor in turn becomes smaller. In addition, also the size of the cross-section at the outlet of the stator cascade was reduced in order to lower the diffusion factor (see table 5.2).

5.2.1 Leading edge

At the beginning of section 5.1, a brief discussion of the computed incidence of $i_S = -13^\circ$ led to the conclusion that the stator vanes are not thoroughly adapted to the incoming flow. Although it is common to design compressor cascades with little negative incidence to allow for little profile losses not only in the BEP but also in part-load and overload [47], an angle of $i_S = -13^\circ$ is too much. Pfleiderer [47] presented findings by Weinig, Carter and Lieblein, Halstrick and Linsi for recommended incidence for different types of thermal turbomachinery², however

²In these findings the recommended incidence for the BEP lies in the low to mid single digit range.

their applicability to mixed-flow pumps seems to be doubtful. Instead, with the help of simulations an appropriate blade angle of $\alpha_{3B} = 39^\circ$ was identified for the leading edge of the diffuser vanes of the *PS550* pump model.

5.2.2 Axial length

A guide value for the minimal axial length of the diffuser vanes at midspan can be assessed from equation (2.32), which gives $l_{ax,min}/l_{ax,Ref} = 1.072$ for the *PS550* mixed-flow pump with $n_q = 158.1$ rpm. The same equation evaluated at the hub illustrates that the blade should be at least one-third longer.

5.2.3 Trailing edge

To determine reference values for the suitable blade angles at the trailing edge the correlation of Weinig as presented in section 2.3.2 was consulted. The process of achieving these values is exemplarily demonstrated by means of configuration D (table 5.2). At first the stagger angle

$$\gamma_m = \frac{\alpha_{3B} + \alpha_{4B}}{2} \sim 60^\circ \quad (5.7)$$

is computed. Together with the inverse of the solidity $1/\sigma \sim 0.5$ an exaggeration factor μ of around 0.775 can be read from figure 5.3. Using the corrected camber angle

$$\theta_B^* = \frac{|\alpha_{4B} - \alpha_{3B}|}{\mu} \quad (5.8)$$

allows to finally calculate the required exaggeration

$$\Delta\alpha_B = \frac{(1 - \mu) \cdot |\alpha_{4B} - \alpha_{3B}|}{2\mu}, \quad (5.9)$$

which in this case amounts to around 7° . The computed exaggeration gives a very similar result to Gülich's recommendation of 4° to 6° .

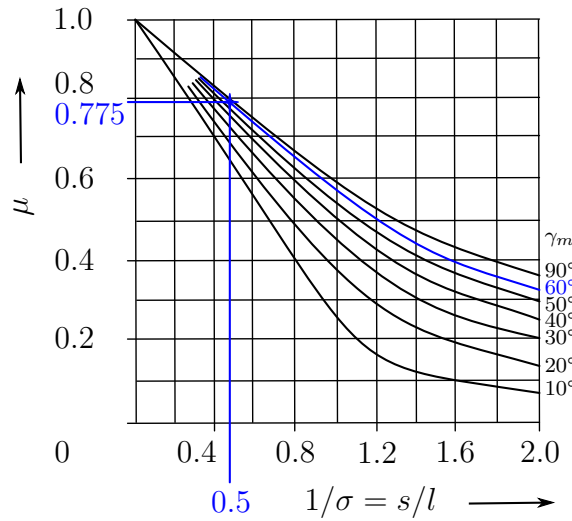


Figure 5.3: Determination of the exaggeration factor for configuration D, modified from [10]

5.3 Suitable designs

5.3.1 Overview of design variants

Altogether, more than 30 different design variants were tested. The number of stator vanes z_S , the axial length l_{ax} and the blade angle at the trailing edge α_{4B} were varied according to the aforementioned considerations. In figure 5.4 the most promising designs are compared to the original configuration. The geometrical data of these variants can be looked up in table 5.2. The original design (A) of the reference configuration is marked in blue, the most suitable design (J) which was then chosen as a basis for the following optimization is marked in green. One can see that all of the applied modifications result in a significantly higher solidity and subsequently in a lower diffusion factor which now lies within the range of the limits (0.45 at the shroud and 0.6 at the hub) proposed by Gülich (section 2.3.2).

Figure 5.4 illustrates that the loss of total pressure evaluated between the stator inlet (3) and the measurement cross-section (mcs), which is expressed in non-dimensional form as

$$\omega_{Stator} = \frac{p_{t,3} - p_{t,mcs}}{p_{t,3} - p_3} \quad (5.10)$$

can be reduced by over 50%. Accordingly the simulated head coefficient ψ_{Sim} is increased marginally and the efficiency rises by about four percentage points.

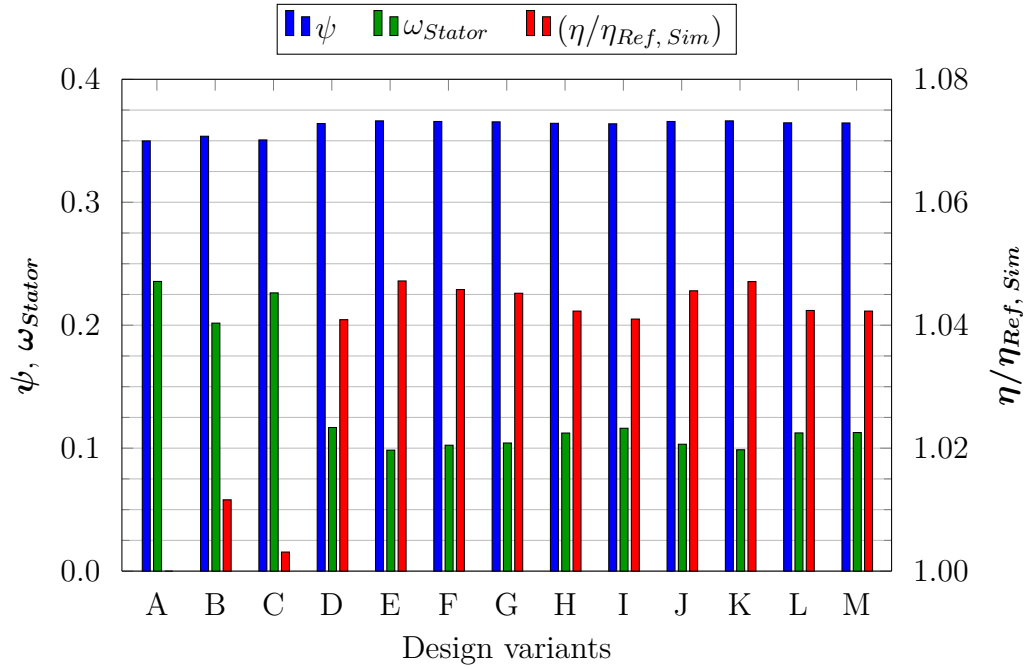


Figure 5.4: Comparison of various stator designs: A - reference configuration, J - most suitable design

	z_S	l_{ax}	A_4/A_3	α_{4B}	l	s	σ	D
A	5	1.000	1.117	1.000	1.000	1.000	1.455	0.782
B	5	1.000	1.117	0.927	0.997	0.892	1.626	0.636
C	5	1.195	1.154	1.008	1.168	1.013	1.678	0.677
D	5	1.359	1.065	1.095	1.324	0.973	1.981	0.615
E	5	1.359	1.002	1.095	1.329	1.006	1.921	0.585
F	6	1.359	1.002	1.095	1.329	0.839	2.305	0.549
G	7	1.359	1.002	1.095	1.329	0.719	2.689	0.523
H	8	1.359	1.002	1.095	1.329	0.629	3.073	0.504
I	9	1.359	1.002	1.095	1.329	0.559	3.457	0.489
J	5	1.359	1.002	1.148	1.344	1.006	1.942	0.589
K	5	1.606	1.086	1.061	1.525	0.986	2.250	0.597
L	5	1.606	1.086	1.090	1.532	0.986	2.259	0.600
M	5	1.606	1.086	1.148	1.545	0.986	2.280	0.604

Table 5.2: Geometrical data and resulting diffusion factor at midspan of most promising design variants, all values are scaled in relation to the corresponding quantities of the reference configuration (A)

An interesting conclusion that can be drawn from figure 5.4 is that from variant E to I, as the number of stator vanes is increased by an increment of one, the pressure loss steadily rises as well. This means that, although a higher number of blades reduces the load on every single one and thus reduces the area of flow separation, the additional losses due to the increased friction overcompensate the positive effects. On that account a change of the number of blades was discarded for the further design process.

5.3.2 Comparison of the reference configuration to the most suitable design

In this section the best configuration from table 5.2, which is design J, is compared to the original stator of the *PS550* mixed-flow pump. Type J was chosen as the design to continue the development process with, because it represents the best combination in terms of low pressure losses, high efficiency and little residual swirl downstream the stator (which is the main reason, the variants E, F, G and K were discarded as they were unable to reduce the swirl at the same magnitude as type J). The most noticeable difference between configuration J and the original stator are the vanes which were lengthened by over a third. In addition to that also the hub diameter at the exit of the diffuser vanes was increased to obtain a passage which has roughly the same cross-section area at the inlet and the outlet ($A_4/A_3 \sim 1$). The backwards cut of the original trailing edge was abandoned, instead a straight shape was imposed. The meridional contour of the leading edge remained unchanged. Moreover, the blade angles were altered as explained in section 5.2. An overview of the modifications can be assessed from figure 5.5 in which the meridional contour of the original diffuser is compared to that of type J. The impact of these design changes on the flow pattern is presented in the following paragraphs.

Figure 5.6 depicts the contour plots of relative static pressure for the reference design (left) and the improved design of type J (right). As mentioned in section 5.1, the reference design suffers from massive incidence, thus the stagnation point has moved towards the suction side of the blade. By increasing the blade angle α_{3B} by about 6° incidence in BEP could be reduced dramatically and the stagnation point is now situated almost directly at the tip of the blade.

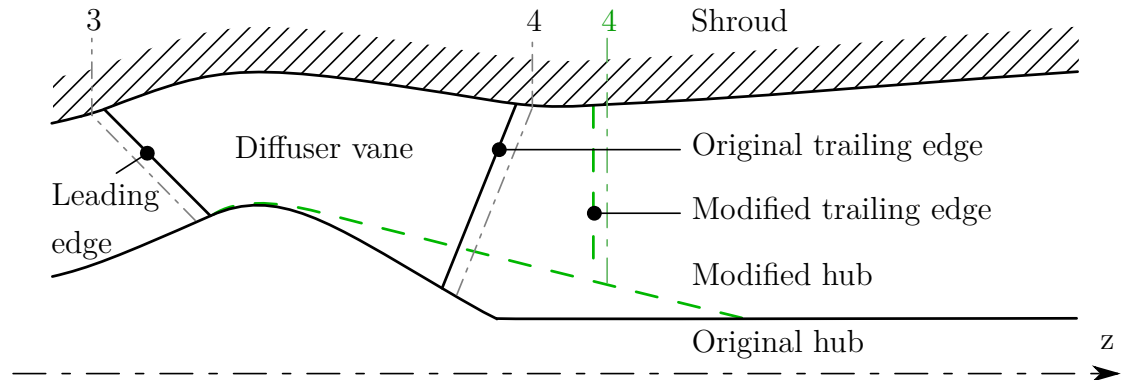


Figure 5.5: Comparison of original meridional contour (solid black lines) and type J (dashed green lines)

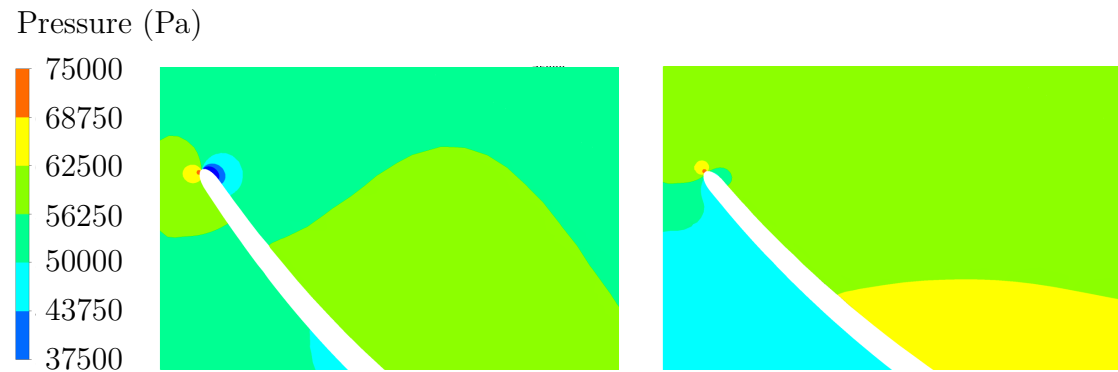


Figure 5.6: Position of stagnation point at the leading edge of the diffuser vane; left: reference design; right: improved design (J)

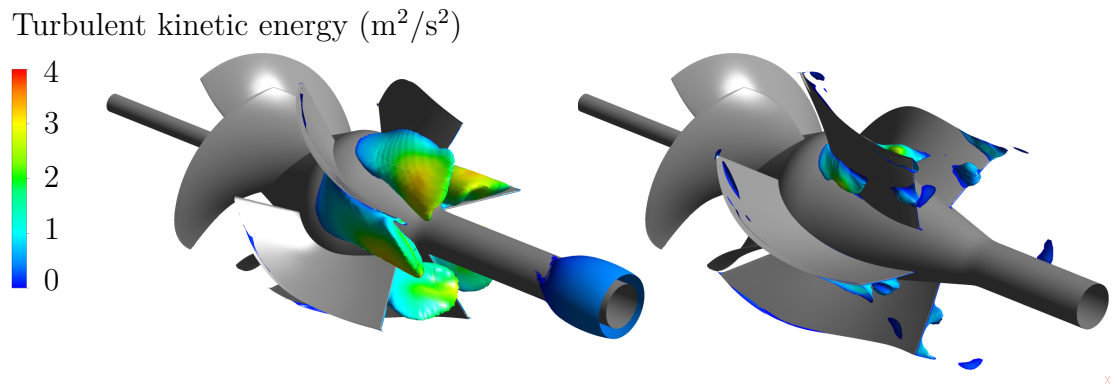


Figure 5.7: Isosurfaces with axial velocity $c_{ax} = 0$ m/s, coloured by the turbulent kinetic energy of the fluid; left: reference design; right: improved design (J)

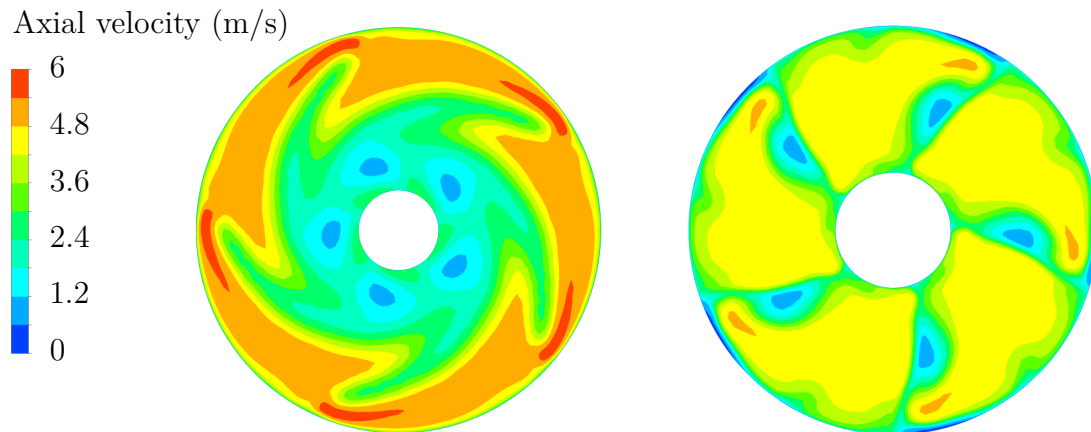


Figure 5.8: Contour plot of axial velocity c_{ax} 100 mm downstream the trailing edge of the diffuser vane; left: reference design; right: improved design (J)

With the help of figure 5.7 it is possible to demonstrate impressively how effective an increase of the chord length of the blade can be in order to prevent separation. In the picture of the original pump on the left an extensive blockage area that has its origin at the hub of the suction side of the diffuser vane can be seen. Close to the end of the hub downstream the stator a small fraction of the dead water core caused by the residual swirl becomes visible. The improved design on the right of this figure does not show this phenomenon. Now, the flow separation zone is also drastically smaller and produces a much more uniform velocity distribution (right picture of figure 5.8). Compared to the original design which yields a contour plot of axial velocity that has over two thirds of its diameter affected by the separation bubble, in design J only the sectors directly behind the five blades show the expected velocity deficit.

In the diagram of figure 5.9 the normalized static pressure in the stator domain is plotted over the streamwise location. The pressure of the reference configuration starts to decline rapidly at approximately one third of the blade length at a streamwise location of 0.16 (I). At this point the flow passes the maximum diameter of the hub and starts to separate from the suction side of the blade close to the hub. As the flow advances through the passage, an increasing amount of the cascade cross-section becomes affected by the separation zone which causes a further drop of pressure to the exit of the passage. Immediately after the trailing edge the normalized pressure rises sharply at first due to the sudden expansion of the cross-

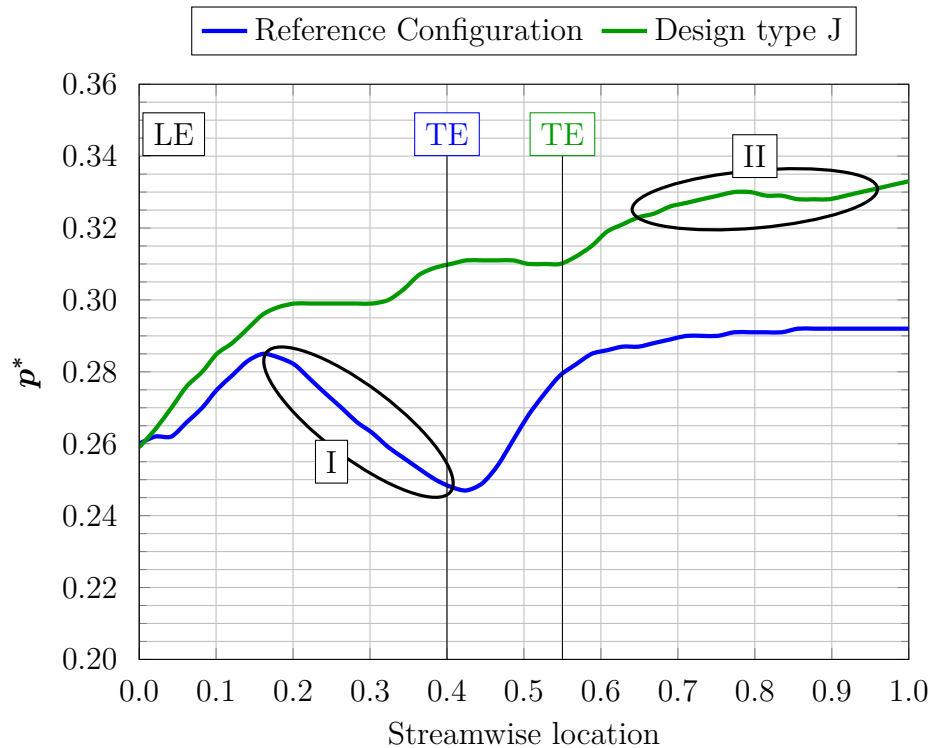


Figure 5.9: Distribution of normalized static pressure p^* in the stator domain; I: pressure drop due to flow separation; II: pressure recovery in the diffuser

section, but then levels off quickly. A maximum of just above 0.29 is reached at the end of the outlet diffuser (streamwise location = 1). The curve of the improved design J shows a gradual incline of pressure in the first third of the blade to a streamwise coordinate of around 0.2. When the separation zone, which now is much smaller, starts to build up, the pressure stays constant at first, then increases slightly and finally remains steady towards the trailing edge. In the annular diffuser after the blade exit, a pressure recovery of minor extent can be observed (II). Again the maximum pressure is reached at the end of the outlet diffuser.

In figure 5.10 the mass flow averaged flow angle, evaluated around 150 mm upstream the measurement cross-section, is plotted against the spanwise coordinate. The values of the flow angle are scaled so that a swirl-free flow ($\alpha = 90^\circ$) corresponds to 1. In the reference configuration the flow angle varies greatly from hub to shroud. It has its minimum of about 0.44 at a quarter of the span. At this spanwise coordinate the flow separation zone has its biggest extent, thus the downstream flow is most affected. From there the flow angle rises evenly with increasing span,

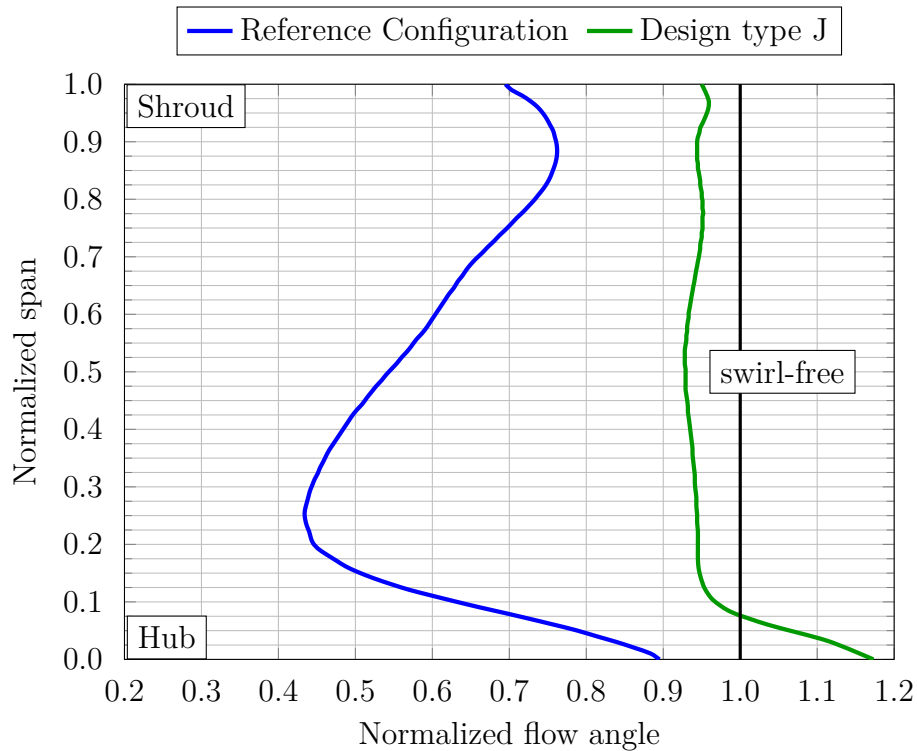


Figure 5.10: Distribution of mass flow averaged flow angle, evaluated around 150 mm upstream the measurement cross-section

until it becomes smaller again towards the shroud. Nearby the hub the flow angle approaches its maximum of 0.9 which can be explained by the unguided flow in the dead water core. The upper plot of figure 5.11 confirms this assumption as it shows that the velocity vectors near the hub at a span of 0.05 are completely perturbed. The improved design reveals a different, much more even distribution of the flow angle from hub to shroud. In fact, within a span ranging from 0.1 to 1 the normalized flow angle stays almost constant at a value of approximately 0.93. Only very close to the hub the velocity vectors are negatively affected by the separation zone that forms on the suction side of the diffuser vanes (lower plot of figure 5.11). Thus the flow is overturned at the hub which results in the increase of the flow angle at a low spanwise coordinate. As this behaviour is a direct result of the flow separation in the stator³, it cannot be corrected by a further adaptation of the exit blade angle α_{4B} .

³The flow separation is still present in the improved design and could not be removed entirely, but its extent has become much smaller.

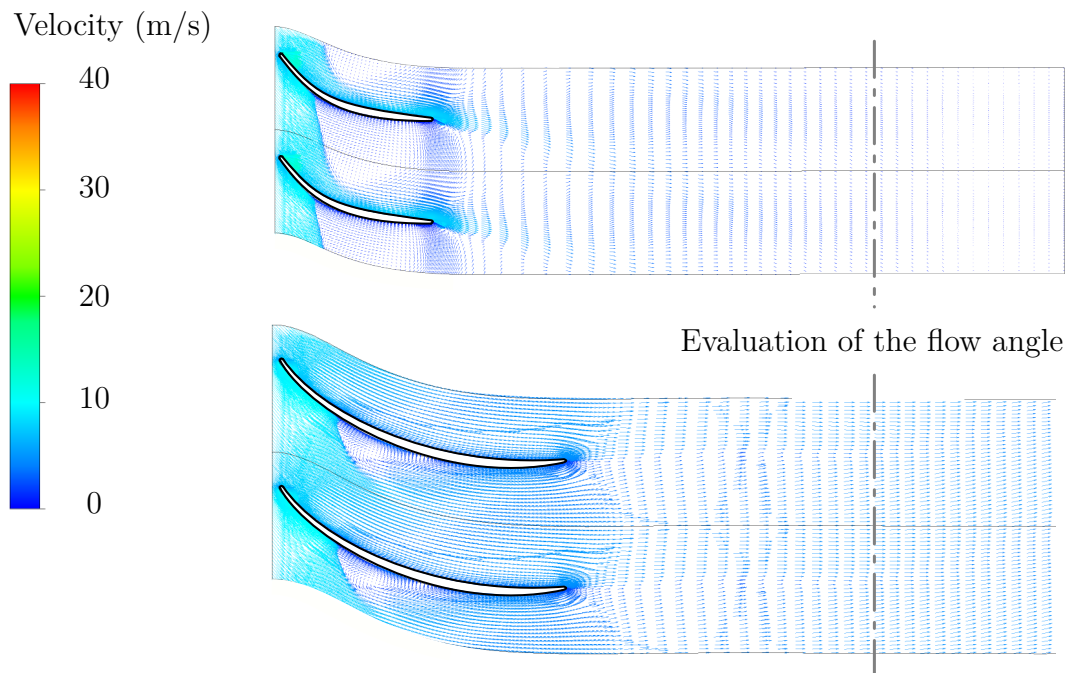


Figure 5.11: Comparison of velocity vectors of the reference configuration (top) and the improved design J (bottom) near the hub (span = 0.05)

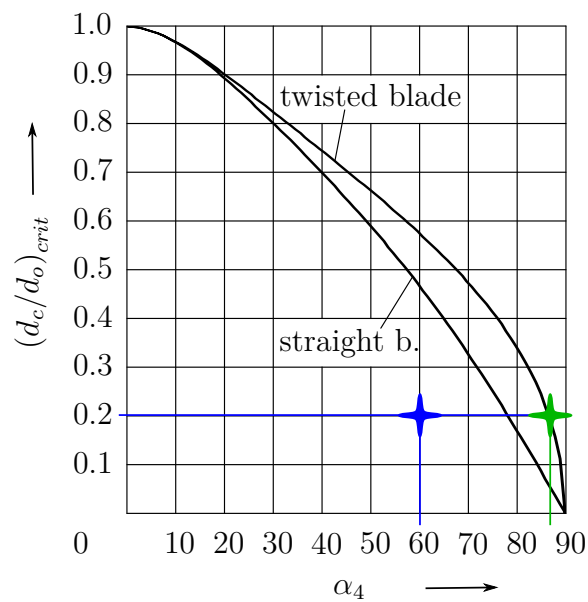


Figure 5.12: Position of the reference configuration (blue marker) and the improved design of type J (green marker) in relation to the curve of the critical hub diameter as proposed by Bammert and Kläukens [7]

Figure 5.11 does not only depict the flow patterns near the hub, but also illustrates how much the blades actually increased in length. In addition, the cross-section at which the flow angles of figure 5.10 were evaluated is indicated by grey dash-dotted lines. On average, the flow angle at the illustrated cross section lies just below 60° for the original design and at around 87° for the improved configuration of type J. With the flow angle of type J being that close to 90° the criterion of Bammert and Kläukens (depicted in figure 5.12) is met and so the dead water core does not appear any more (refer to the right plot of figure 5.7).

By lengthening the diffuser vanes and correcting their blade angles, incidence and flow separation in the BEP were reduced substantially. Pressure losses in the stator were more than halved, which resulted in an efficiency gain of over four percentage points. Moreover, the residual swirl in the flow exiting the diffuser was almost eliminated.

Chapter 6

Optimization

After the flow separations that occurred in the stator of the original configuration of the *PS550* pump had been reduced significantly, the model was set up for optimization. The general methodology for this optimization is explained in the first section of this chapter. It is then followed by sections that elucidate the parametrization of the blade geometries and the definition of objective functions for the rotor and stator component. Finally, the trade-off between conflicting objectives is shown and the optimized geometry is compared to the reference design. Moreover, the resulting performance characteristics are presented.

6.1 Methodology

6.1.1 Workflow

The focus of the optimization process was to provide an exemplary workflow of how to improve the peak efficiency of a mixed-flow pump with comparatively low effort. Therefore, one major boundary was that it must be possible to carry out the simulations necessary in order to gather sufficient data for the actual optimization on common engineering workstations within a reasonable amount of time. The second major boundary was that software which is already well-established in the turbomachinery industry should be used, in order to minimize problems with data conversion and data transfer between different kinds of software and to prevent extra costs. On that account, the workflow presented in figure 6.1 was defined.

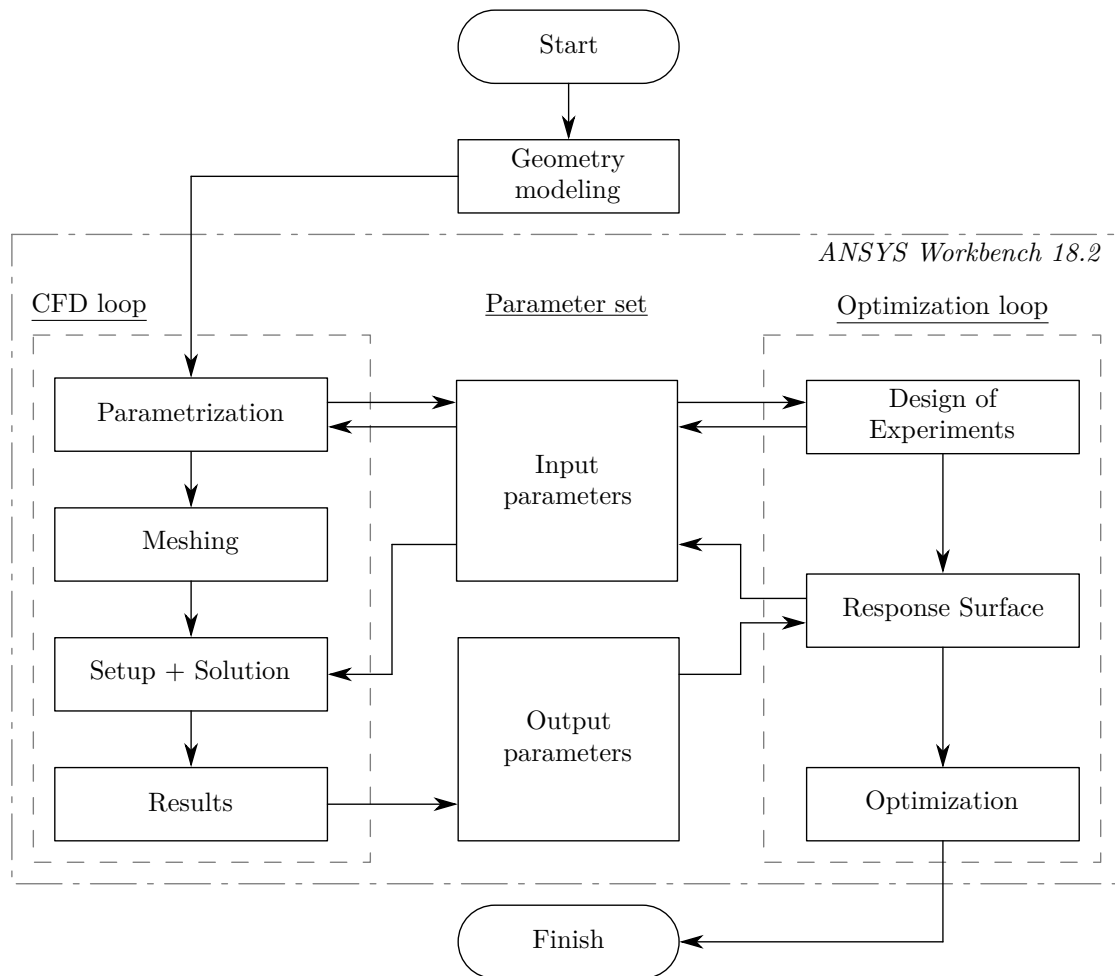


Figure 6.1: Flowchart describing the optimization framework

The first step in the process is remodelling the original pump from paper drawings by means of an appropriate CAD software package. While this step could also be done in the *DesignModeler* module of *ANSYS Workbench* in this thesis Siemens' *Solid Edge ST8* was used. A turnkey CAx tool such as *Solid Edge* provides more options in terms of drafting, CAM or data management for subsequent production. The finished CAD model of the pump is imported in *ANSYS Workbench 18.2*, in which from then on all further tasks of the workflow are executed. Parametrization takes place in *DesignModeler*. At first the CAD model is stripped of all unnecessary details, such as gaps or interferences between adjacent bodies, overlapping faces or casting radii. Then dimensions that are to be altered in the optimization loop are defined as input parameters, while other dimensions are fixed. As it is customary with CFD simulations, the following steps are meshing, setting up the solver and solving the flow equations. The results are achieved by post-processing. A thorough

explanation of the settings for these three tasks is given in chapter 4. In the results task, flow quantities such as the static and total pressure as well as integral terms such as the total head rise or the efficiency are chosen as output parameters. Both, the input and the output parameters are stored in a parameter set which serves as a database for the optimization loop¹. The input parameters that are defined in the *DesignModeler* are passed on to the Design of Experiments step in which a list of design points that have to be evaluated in the CFD loop is created. For this purpose, for every input parameter a range of allowed values has to be defined. From the list of design points the values of the input parameters are read out and transferred on the one hand to the *DesignModeler*, in which the geometry is adapted accordingly and on the other hand to the setup step, in which the volume flow rate is checked. Then the flow equations are solved for this specific design point and the resulting values for the observed quantities are passed to the list of output parameters. This process is repeated until all design points are evaluated. In the next step the response surface is built from the information of the DOE and the output parameters. The RS task forms a basic functional relationship (= response surface) between input and output parameters of the design point list and assesses the quality of the created response surface. If the RS fails to meet the user-defined quality requirements, additional design points (= refinement points) are added to the parameter set and computed in the CFD loop. If the desired quality of the RS is accomplished, the data is transferred to the Optimization task. The most important action in this step is to define the objectives and constraints of the optimization. A general objective would be to maximize or minimize a certain (combination of) output parameter(s) without exceeding predefined boundaries for the input parameters. Moreover, in some cases it might come handy to specify additional relationships between parameters. Based on these inputs the optimization is carried out by a genetic algorithm which finally provides a set of three candidate points that fulfil the given criteria best. After evaluating the predictions that the optimization algorithm made for the parameters of the candidate points, the user of this workflow has to pick the one which obtains the highest performance gain for the pump.

¹The general concepts of optimization are explained in section 2.5.

6.1.2 Settings for the CFD loop

As explained before, the majority of the setup of the CFD simulations was kept the same as described in chapter 4. However, in order to keep the number of input parameters and so design points created by the DoE low, the domain was split at the interface two (figure 4.1). In the first optimization cycle, only the rotor was modified, because the feedback from the stator to the flow in the impeller is negligible. Therefore, the stator and outblock domain as well as the outlet elbow were omitted in these simulations. In the second optimization cycle, the inblock and rotor domains were removed and only the stator and outblock domains were included. The outlet elbow was neglected again. Beyond that, the boundary conditions were adapted. In the first optimization cycle, instead of IF2 an outlet with specified mass flow rate was placed, whereas in the second cycle the corresponding surface was defined as an inlet boundary. After the optimization of the rotor component, the values of the flow quantities (p_t , c_r , c_θ , c_z as well as k and ε) at the impeller exit were computed and imposed at the inlet boundary of the stator. Another huge benefit of conducting two separate optimization cycles was that, due to the then reduced number of grid cells, the calculation time of every design point was almost halved compared to simulations of the whole domain. All simulations for the two optimization cycles were conducted with the flow rate of the BEP of the original machine.

6.1.3 Settings for the optimization loop

Considering that the whole workflow described above should have been conducted on a single workstation it was viable to keep the number of design points to evaluate as low as possible. Therefore, the OSF algorithm with a maximum of ten iteration cycles was employed to create the samples for the Design of Experiments task, as it provides a good filling of the design space. A full quadratic model was picked for sampling. It is known from similarity numbers, that the head of the pump (flow quantity) is proportional to the square of the impeller diameter (geometrical quantity). Therefore, a quadratic model between the input parameters (mostly geometrical quantities) and the output parameters (flow quantities such as pressure and velocity) should fit best. The genetic aggregation algorithm was chosen for the generation of the response surface. The quality of the RS was assessed by the maximum predicted error, which was set to 0.008 for the efficiency of the

Property	Settings	Options
Design of Experiments type	Optimal Space-Filling	Max-Min Distance, 10 iteration cycles
Samples type	Full Quadratic	

Table 6.1: Basic settings for the Design of Experiments task

Property	Settings	Options
Response Surface type	Genetic Aggregation	
Tolerances	Max. predicted error	η_R : target = 0.008
		ω_{Stator} : target = 0.01

Table 6.2: Basic settings for the Response Surface task

Property	Settings	Options
Method	MOGA	100 initial samples
Number of samples per iteration	100	max. 50 iteration cycles

Table 6.3: Basic settings for the Optimization task

impeller η_R and to 0.01 for the loss of total pressure ω_{Stator} in the stator. The Multi-objective Genetic Algorithm implemented in *ANSYS DesignXplorer* was selected for the optimization step. The number of initial samples as well as the number of samples created per iteration of MOGA was pre-set to 100. Although a maximum of 50 iteration cycles was specified, the algorithm converged after less than ten iterations. The most important settings for the tasks of the optimization loop are summarized in tables 6.1 to 6.3.

6.2 Rotor optimization cycle

6.2.1 Parametrization

Preliminary analysis have exhibited that the original impeller is designed very well, it does not show any major weaknesses. Its peak efficiency reaches almost 94%.

Therefore, the distribution of the blade angles from leading edge to trailing edge as well as the distribution of the blade thickness was just smoothed. This implies that for each layer the curve for the mean line as well as for the thickness was substituted by a third order Bezier-curve, which was automatically generated by the *Blade* feature in *ANSYS DesignModeler* after defining the coordinates of the Bezier-points. It is presented in [25] that altering the blade profile at the LE and TE affects cavitation behaviour and the impeller efficiency². As the main target of the optimization process was to increase the efficiency of the pump in its BEP the following four input parameters were defined:

1. t_{LE} - thickness of the leading edge
2. t_{TE} - thickness of the trailing edge
3. ER_{LE} - ellipse ratio of the leading edge
4. ER_{TE} - ellipse ratio of the trailing edge

A total number of five layers were used to form the rotor blade. For each of these five layers, the thickness distribution was controlled the by the two parameters t_{LE} and t_{TE} . However, a constraint was set, so that the blade thickness decreases linearly from hub to shroud by 20%. Similarly, for the ellipse ratios an increase of 20% from hub to shroud was imposed. The coordinates of the inner Bezier-points were determined by a weighted linear combination of the thickness of the blade at the leading and at the trailing edge. The weights of the linear combination were controlled by another constraint that guarantees for sufficient thickness in order not to harm the structural integrity of the rotor blades. In addition to the aforementioned input parameters, the axial position and the shape of the leading edge were parametrized with the help of:

1. $z_{LE,h}$ - axial position of LE at the hub
2. $z_{LE,s}$ - axial position of LE at the shroud
3. r_{LE} - radius of LE in a meridional cross-section

²For example, a long, wedge-like shape of the leading edge allows for the highest efficiency but suffers from incidence in off-design points.

ID	t_{LE}	t_{TE}	ER_{LE}	ER_{TE}	a)	b)	c)
Min.	0.495	1.209	0.156	0.076	0.000	0.000	0.396
Ref.	1.000	1.000	1.000	1.000	0.219	0.000	0.660
Max.	1.902	4.837	2.338	1.140	0.264	0.079	1.319

Table 6.4: Ranges of the design variables for the rotor optimization cycle: t_{LE} , t_{TE} , ER_{LE} , ER_{TE} are scaled in relation to the corresponding quantity of the reference configuration; a) = $z_{LE,h}/d_{2o}$, b) = $z_{LE,s}/d_{2o}$, c) = r_{LE}/d_{2o}

Except for the thickness and the ellipse ratio, the shape of the trailing edge remained unchanged. A detailed explanation of the seven design variables chosen as input parameters is given in figure 2.7. Their permitted ranges are listed in table 6.4. A full register of all design points created by the DOE and the RS based on the parametrization explained above can be read up in table A.5. The minimum and maximum values of those parameters were determined according to the analytical criteria for blade design presented in section 2.3.2 as well as by the capabilities of the *Blade* feature of *ANSYS DesignModeler* and the meshing tool *TurboGrid*.

6.2.2 Objectives

Parameter	Objective	Importance	Target value
$\eta_R/\eta_{R, Ref, Sim}$	maximize	high	
$A_{Cav}/A_{Cav, Ref, Sim}$	minimize	low	

Table 6.5: Definition of the objectives for the rotor optimization cycle

The primary aim for the optimization of the rotor component was to maximize the impeller efficiency η_R . However, cavitation tendencies should not be burdened by any measure taken to increase the efficiency. The area of isosurfaces A_{Cav} with local static pressure below vapour pressure was computed in *CFD-Post* and set as additional output of the simulations in order to assess cavitation. Therefore, the second objective was to minimize the area of these isosurfaces. The reason for not paying more attention to the influence of cavitation on the rotor design is that the focus of this thesis lay on simplicity and practicability rather than on considering everything to the last detail. Hence, this user-friendly, yet sufficiently

dependable approach was chosen. Elaborate techniques to assess cavitation areas in a centrifugal pump or to calculate the NPSH-curve of such a machine were presented by [22] and [40] respectively.

6.2.3 Results

The outcome of the rotor optimization cycle is summarized in table 6.6 in which the design variables and the output parameters of the reference impeller are compared to the optimized configuration. Column d) and e) show that the impeller efficiency could be raised by one percentage point and the area of isosurfaces with a static pressure below the vapour pressure could be lowered by about ten percentage points. These observations are confirmed by the plots depicted in figure 6.2. They provide a visualization of the areas of the leading edge at which cavitation has to be expected. The entire LE of the original impeller is affected by low pressure zones. These zones are significantly less visible around the leading edge of the optimized blade profile. A possible explanation for this effect can be found by looking at figure 6.3 which matches the shape of the LE of the reference design against the optimized one. It is obvious that the contour of the original LE is leaner and more pointed towards the tip than the contour of the optimized LE is. In theory, such a shape should be beneficial when trying to achieve a high efficiency in the BEP, however in the present optimization, the performance of the original rotor is worse. This is a clear indication that the inflow to the rotor is not free of incidence. In other words, the thicker, much more rounded design of the optimum leading edge is much less sensitive to these incident flow conditions and therefore yields a higher impeller efficiency η_R and a smaller low pressure area.

ID	t_{LE}	t_{TE}	ER_{LE}	ER_{TE}	a)	b)	c)	d)	e)
Ref.	1.000	1.000	1.000	1.000	0.219	0.000	0.660	1.000	1.000
Opt.	1.314	1.230	0.275	1.127	0.063	0.062	0.700	1.010	0.903

Table 6.6: Comparison of the optimized design to the reference configuration: t_{LE} , t_{TE} , ER_{LE} , ER_{TE} are scaled in relation to the corresponding quantity of the reference configuration; a) = $z_{LE, h}/d_{2o}$, b) = $z_{LE, s}/d_{2o}$, c) = r_{LE}/d_{2o} , d) = $\eta_R/\eta_{R, Ref, Sim}$, e) = $A_{Cav}/A_{Cav, Ref, Sim}$

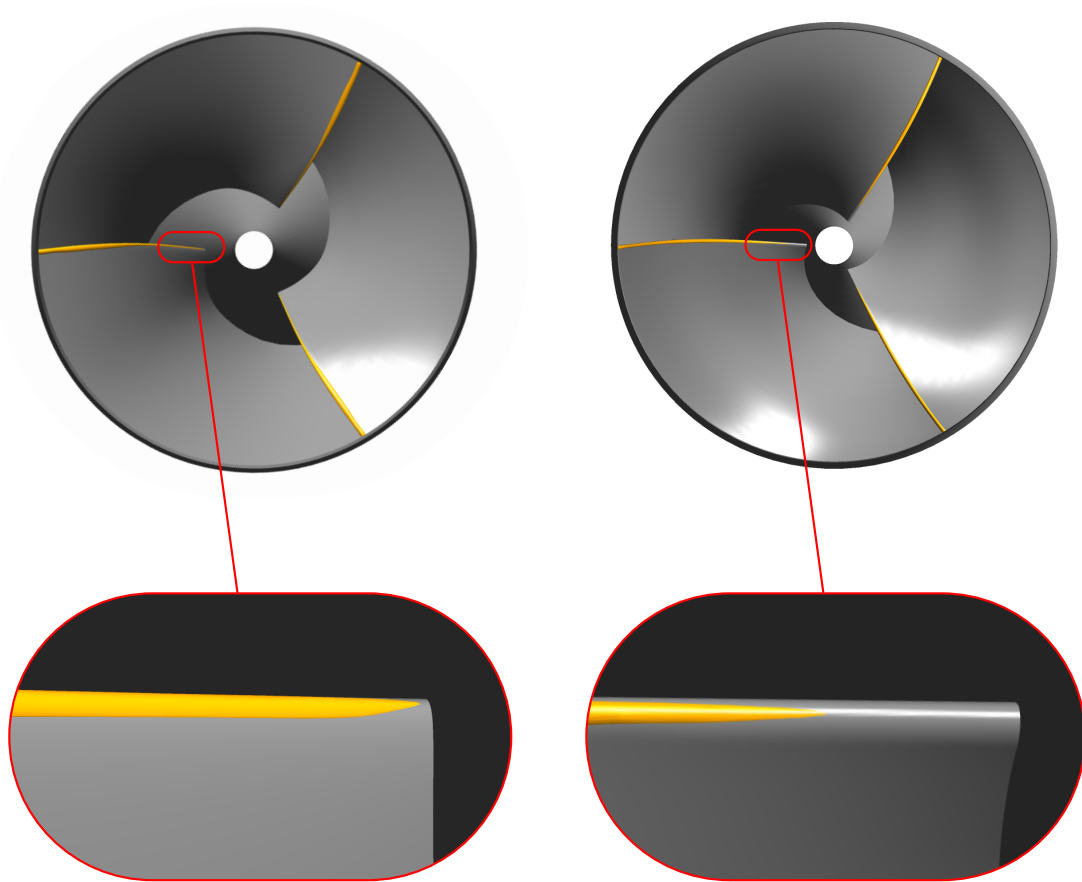


Figure 6.2: Comparison of isosurfaces with a static pressure below the vapour pressure of 2339 Pa (orange) at the LE of the impeller; left: reference configuration; right: optimized design

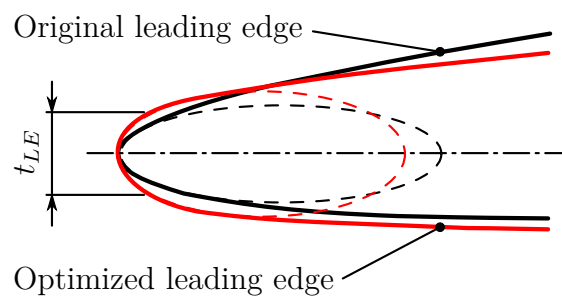


Figure 6.3: Detail view of the leading edge of the rotor at the hub: reference design - black, optimized design - red

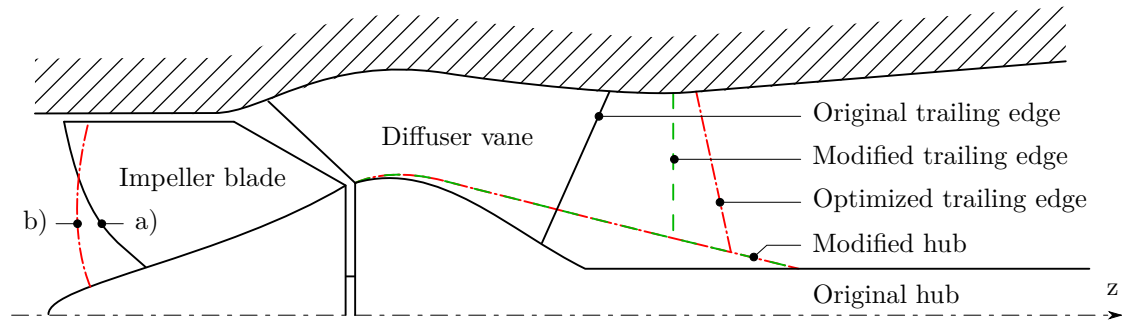


Figure 6.4: Comparison of meridional cross-sections: original - solid black lines, improved design (type J) - dashed green lines, optimized design - dash-dotted red lines; a) = original LE, b) = optimized LE

Another possible reason for the reduced cavitation zone is given by the revised meridional contour of the optimized LE as presented in figure 6.4. Opposing to the original leading edge, the optimized one is pulled forward at the hub which according to Gülich helps to reduce cavitation near the hub (especially at part-load conditions) [25].

In general, figure 6.5 stresses the observation that the position of the leading edge, which is controlled by the two dimensions $z_{LE,h}$ and $z_{LE,s}$, has the greatest influence of all seven input parameters on the overall performance of the pump. The sensitivities³ plotted in this figure show that all three output parameters are most affected by the design of the meridional contour of the LE, whereas the ellipse ratio of the TE is negligible.

Figure 6.6 reveals the trade-off between the impeller efficiency and the cavitation zone. Four generations of Pareto-optimal frontiers (POF) are plotted in this diagram, whereupon the best generation, POF1, includes all non-dominated design points (feasible solutions of the optimization). The actual optimum configuration within all the points of POF1 is marked by a red square. It is remarkable that there is a relatively large gap between the predicted values for the optimum configuration and the verified ones. This discrepancy is an indication that the quality of the response surface created from the design points is not sufficient for the optimization. An improvement of the RS and the optimization quality could certainly be accomplished by providing more design points to the response surface.

³The local sensitivity is a measure that indicates what impact a change of the value of a specific input parameter has on the value of a specific output parameter. A negative sensitivity means that an increase of an input quantity leads to a decrease of the corresponding output quantity.

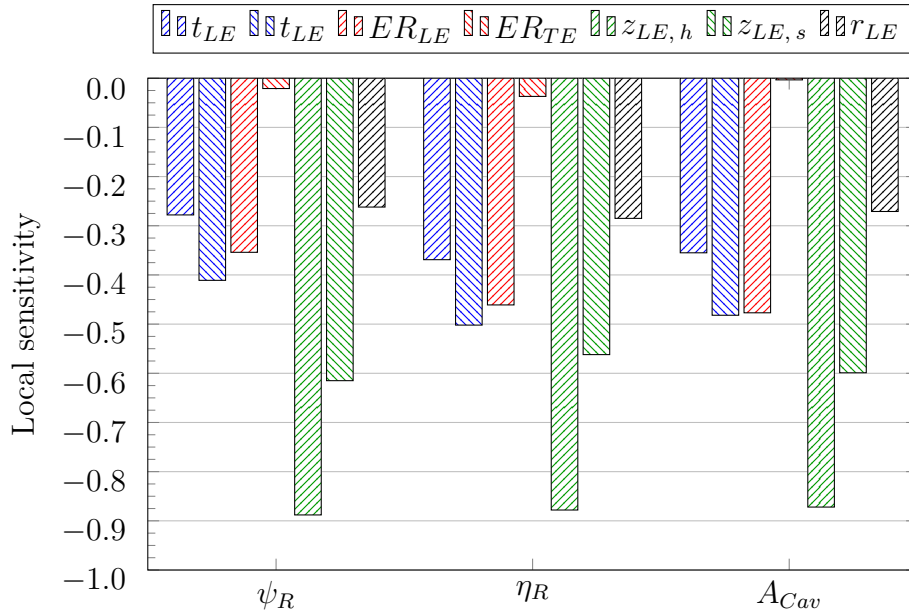


Figure 6.5: Absolute value of the local sensitivities of head coefficient ψ_R , efficiency η_R and area of the low pressure isosurfaces A_{Cav} to a variation of the seven input parameters of the rotor optimization cycle

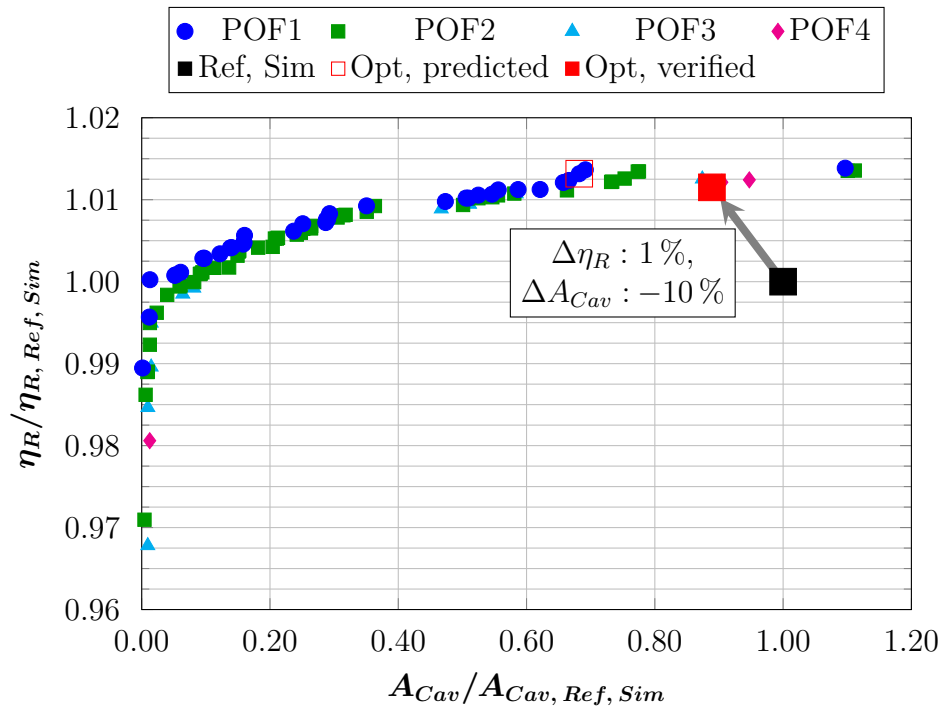


Figure 6.6: Trade-off (Pareto-optimal frontier) between impeller efficiency η_R and area of the low pressure isosurfaces A_{Cav}

6.3 Stator optimization cycle

6.3.1 Parametrization

A thorough analysis of the vaned diffuser was presented in chapter 5. The stator vanes were lengthened and the blade angles were adapted in order to prevent flow separation and to reduce pressure losses. It turned out that the position of the trailing edge as well as the blade angle α_{4B} at the exit of the passage had the greatest influence on the flow in and downstream the vaned diffuser. Therefore the following five input parameters for the second optimization cycle were chosen:

1. $\alpha_{4B,i}$ - blade angle of the trailing edge at the hub (span = 0.0)
2. $\alpha_{4B,m}$ - blade angle of the trailing edge at midspan (span = 0.5)
3. $\alpha_{4B,o}$ - blade angle of the trailing edge at the shroud (span = 1.0)
4. $z_{TE,h}$ - axial position (z-coordinate) of the TE at the hub
5. $z_{TE,s}$ - axial position (z-coordinate) of the TE at the shroud

The blade angles at the leading edge remained the same as in section 5.2. However, for each of the three layers used to build the vane, the original distribution of the blade angle from LE to TE was replaced by a third-order Bezier-curve. Similar to the parametrization of the rotor, the inner Bezier-points were defined by means of a weighted linear combination of the blade angle at the inlet and that at the outlet of the vaned diffuser. Unlike the rotor blades, the thickness distribution of the stator vanes was not altered compared to the reference configuration.

ID	$\alpha_{4B,i}$	$\alpha_{4B,m}$	$\alpha_{4B,o}$	$z_{TE,h}$	$z_{TE,s}$
Min.	0.978	0.985	0.994	1.935	1.326
Ref.	1.000	1.000	1.000	1.000	1.000
Max.	1.150	1.159	1.170	2.419	1.657

Table 6.7: Range of the design variables for the stator optimization cycle: $\alpha_{4B,i}$, $\alpha_{4B,m}$, $\alpha_{4B,o}$, $z_{TE,h}$ and $z_{TE,s}$ are scaled in relation to the corresponding quantity of the reference configuration

The range of the input parameters is listed in table 6.7 and a full register of all design points created in the stator optimization cycle is shown in table A.6. The minimum and maximum values of those parameters were determined according to the design modifications explained in section 5.2 as well as by the capabilities of the *Blade* feature of *ANSYS DesignModeler* and the meshing tool *TurboGrid*.

6.3.2 Objectives

Three objectives were defined for the optimization of the stator (table 6.8). The primary objective was to minimize the loss of total pressure ω_{Stator} which for a stationary component is the equivalent to the increase of the efficiency of a rotating component. The other two objectives were a) to find a configuration that provides a downstream flow with minimum swirl and b) to minimize the area of isosurfaces A_{Sep} with low axial velocity. A flow angle of 90° is required to meet the demand for minimum swirl. Minimizing the extent of the isosurfaces with low axial velocity shall prevent a blocking of the passage by the separated flow, as this adversely affects the stator performance.

Parameter	Objective	Importance	target
ω_{Stator}	minimize	high	
α_{mcs}	seek target	medium	90°
$A_{Sep}/A_{Sep, Ref, Sim}$	minimize	low	

Table 6.8: Definition of the objectives for the stator optimization cycle

6.3.3 Results

The outcome of the stator optimization cycle is summarized in table 6.9, which compares the optimized stator against the reference configuration and design J of section 5.3. It unveils that the modifications suggested by the optimization algorithm yield a design with a lower loss coefficient ω_{Stator} . This comes at the price of a slightly worse flow angle and a bigger extent of the flow separation zone. The sensitivity correlations plotted in figure 6.7 explain the main reason for the reduced losses by a further increase of the blade length at the hub. Opposed to the big impact of the axial position of the TE at the hub, the corresponding position

ID	$\alpha_{4B, i}$	$\alpha_{4B, m}$	$\alpha_{4B, o}$	$z_{TE, h}$	$z_{TE, s}$	ω_{Stator}	α_{mcs}	a)
Ref.	1.000	1.000	1.000	1.000	1.000	0.236	0.696	1.000
J	1.104	1.148	1.193	1.935	1.326	0.092	0.892	0.187
Opt.	0.999	1.095	1.148	2.219	1.340	0.064	0.873	0.190

Table 6.9: Comparison of the optimized design to the reference configuration and design type J of section 5.3: $\alpha_{4B, i}$, $\alpha_{4B, m}$, $\alpha_{4B, o}$, $z_{TE, h}$ and $z_{TE, s}$ are scaled in relation to the corresponding quantity of the reference configuration; α_{mcs} is normalized so that swirl-free flow ($\alpha = 90^\circ$) corresponds to 1; a) $= A_{Sep}/A_{Sep, Ref, Sim}$

of the TE at the shroud is surprisingly not affecting any of the observed output parameters at all. The values for the sensitivity of the four output parameters to a change of the blade angles have to be treated with caution, because the flow exiting the blade passage is affected by the separation zones (figure 6.8). Therefore the calculation of the flow angle and the subsequent prediction of the local sensitivities of the blade angle is not precise.

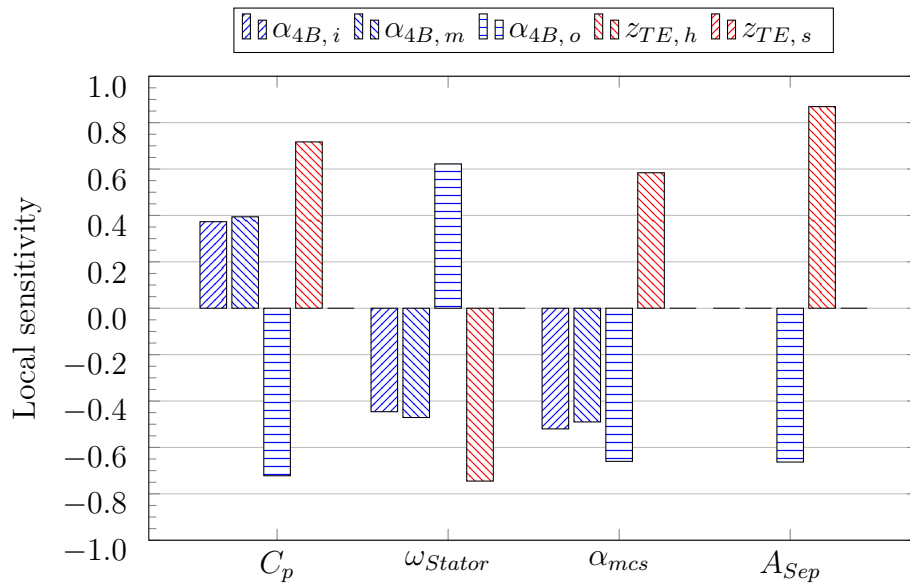


Figure 6.7: Absolute value of the local sensitivities of pressure coefficient C_p , total pressure losses ω_{stator} , flow angle at the measurement cross-section α_{mcs} and the area of isosurfaces with low axial velocity A_{Sep} to a variation of the five input parameters of the stator optimization cycle

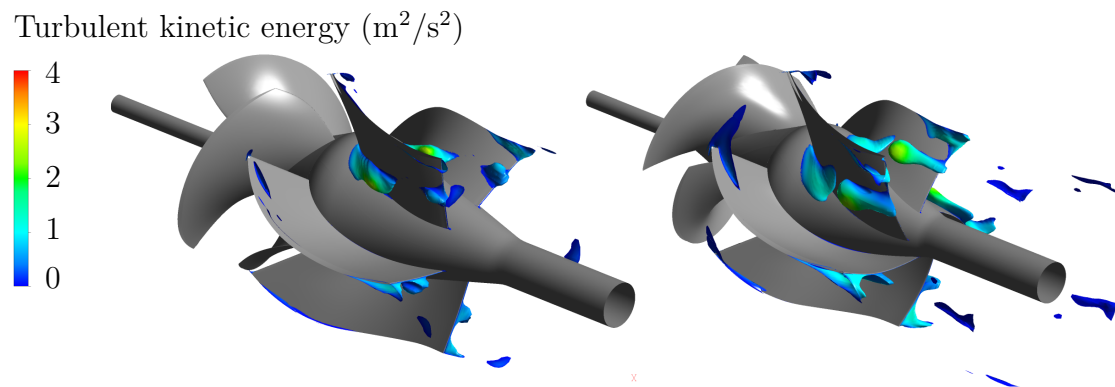


Figure 6.8: Isosurfaces with axial velocity $c_{ax} = 0$ m/s, coloured by the turbulent kinetic energy of the fluid; left: design J; right: optimized design

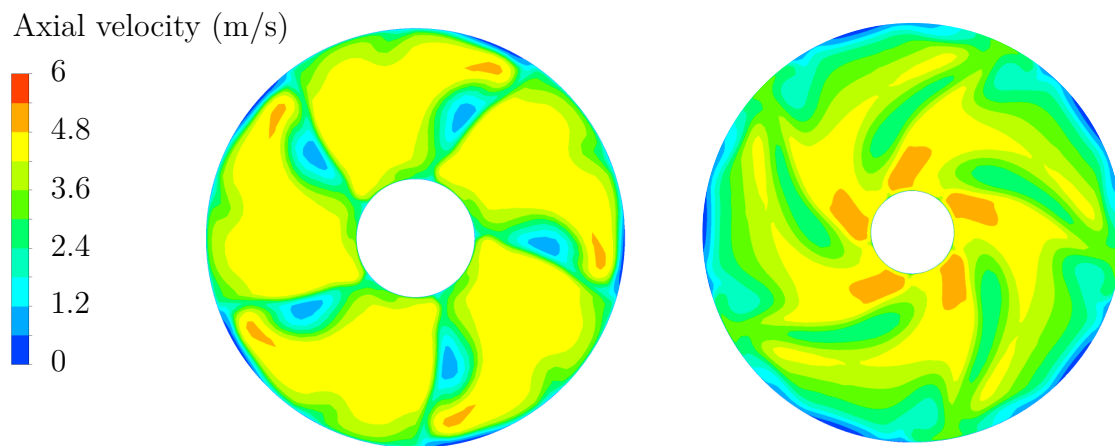


Figure 6.9: Contour plot of axial velocity c_{ax} 100 mm downstream the trailing edge of the diffuser vane; left: design J; right: optimized design

The marginal increase of the area of the isosurfaces with low axial velocity is also depicted in figure 6.8, in which the stator design J is contrasted to the optimized configuration. However, separations in the optimum found are still much less than they were in the original diffuser. Therefore, also the contour plot of the axial velocity, taken downstream the trailing edge of vanes as shown in figure 6.9, is more uniform than that of the reference design (figure 5.8). Nevertheless, the comparison of the three configurations shows that for this specific diffuser the improvement reached by the optimization cycle is almost negligible and not worth the additional computational costs⁴.

⁴The efficiency of the pump is only 0.3% higher when equipped with the optimized stator than it is with stator design J.

6.4 Performance characteristics

Figure 6.10 shows the simulated performance curve of the original pump (Ref, Sim) compared to the configuration with original rotor and optimized stator (I) and the configuration with optimized rotor and optimized stator (II). The main goal of the optimization was met for flow coefficients around the BEP, as the peak efficiency could be improved by over five percentage points. In addition, the efficiency of the optimal design also surpasses that of the original pump in part-load and overload conditions. In the BEP the head coefficient increased by the same extent as the efficiency. The gain of the head coefficient becomes larger towards overload, because the improved rotor is able to handle incident flow in off-design points better than the original one.

In part-load at around $\phi/\phi_{BEP} \sim 0.8$ the slope of the head curve suddenly becomes positive and an instability occurs. The efficiency curves of configurations I and II suffer from a massive slump. In fact, at this specific flow rate, the designs I and II are worse than the original pump. At even lower flow coefficients the head and efficiency curves become smooth and stable again. However, the performance curves of design I with the original impeller and the optimized diffuser remain lying below those of the reference. On the opposite, design II with the optimized rotor and optimized stator exceeds the performance of the original machine considerably. This is a distinct indication that the enhancement in part load can be fully accredited to the rotor, which again profits from the improved leading edge design. On the other hand, the optimized stator accounts for most of the five percent points gain around BEP.

Although there is a number of publications on mixed-flow pumps, e.g. [35, 44] that also show an instable performance characteristic similar to those of the optimized designs I and II presented in this thesis the exact reason for the instability remains vague. Gülich supposes that a sweep-back of the leading edge of the impeller at the hub (as can be seen in figure 6.4 for the optimized configuration) harms the stability of the head curve [25]. But with the *PS550* model pump the instability is already present in configuration I, that is equipped with the original rotor. Therefore, a possible explanation by Höller et al. [28] must be considered. They claim that the diffuser instability is based on the rotor-stator interactions between impeller and diffuser. At part load a backflow out of the diffuser channel at the diffuser inlet which is caused by a disturbed impeller outflow may occur [28]. On that account,

it can be assumed that the flow separations in the vaned diffuser of the *PS550* pump model are not the only reason for the part-load instability. However, it seems possible that the instability as well as the flow separations, which are still present in the stator passage even with the optimized design, are a consequence of the rotor-stator interaction.

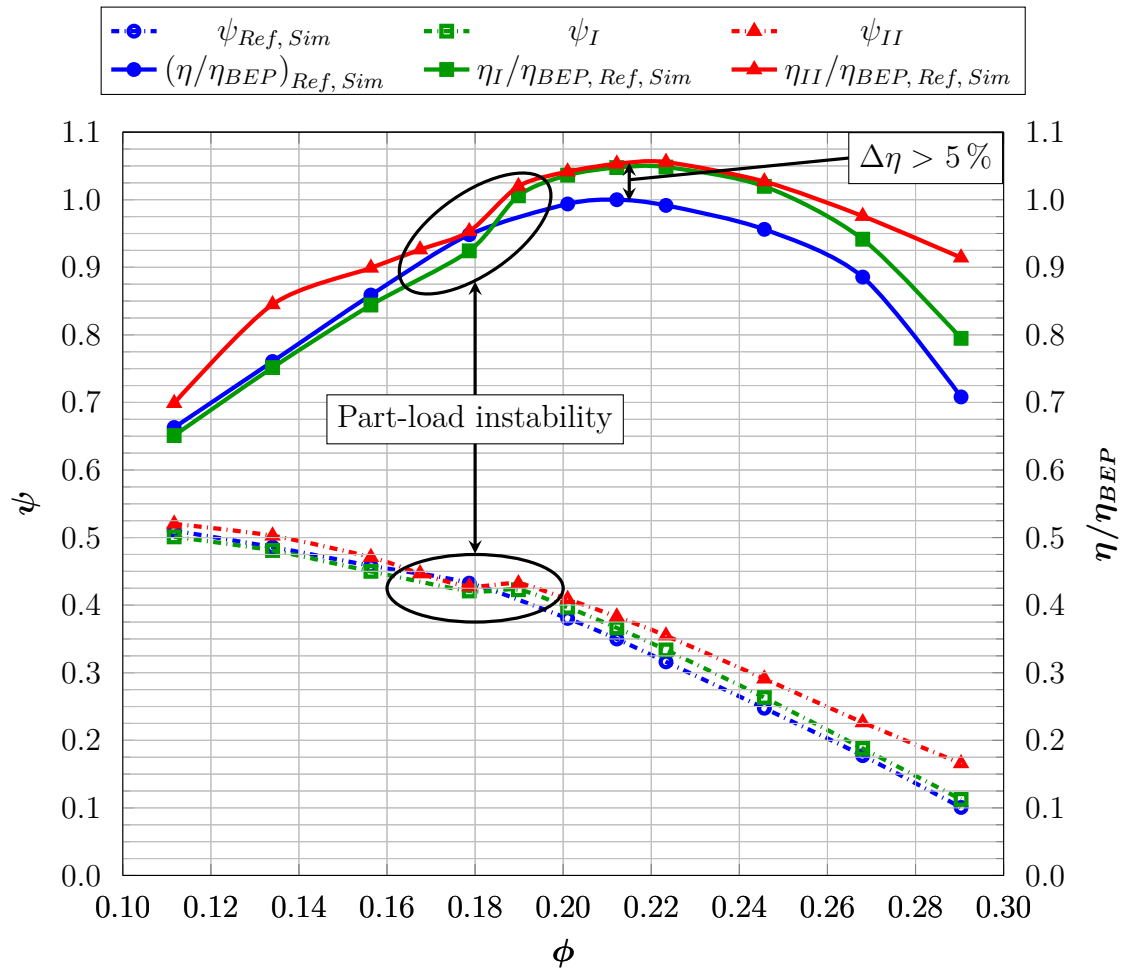


Figure 6.10: Performance characteristic curves: Ref, Sim - original design; I - configuration with original rotor and optimized stator; II - configuration with optimized rotor and optimized stator

Chapter 7

Conclusion

7.1 Outcome

The main goal of this thesis was to develop a simple but sufficiently dependable workflow to improve the performance of a mixed-flow pump at and close to its BEP. However, it turned out to be extremely useful to first consult analytical criteria, e.g. that of Lieblein for blade loading or that of Bammert and Kläukens for hub dead water to get an impression of how the flow in the pump will behave and what phenomena may occur. These criteria in combination with CFD-simulations unveiled that there was an extensive zone of separated flow in the passage of the original diffuser vanes. Therefore the diffuser was redesigned by hand according to the aforementioned criteria and guidelines for the design of hydraulic components as presented in Bohl [10], Gülich [25] and Pfeleiderer [47]. This redesign resulted in an increase of efficiency of around 4% and in a significant reduction of the area of the blades that were affected by the flow separation. However, the separations are still present and it seems that only a full redevelopment of the whole stage may solve this issue.

Starting from the original impeller geometry and the revised stator two separate optimization cycles were defined. In terms of setting up the CFD-model for the required simulations the focus lay on finding an adequate balance between accuracy and computational costs without neglecting the chance to capture any relevant flow phenomenon. Therefore a new approach of splitting the domain at the interface between rotor and stator was introduced. In the first cycle only the impeller was

optimized and in the second cycle only the vaned diffuser (without the impeller) was considered. After the first cycle the outflow of the optimized rotor was computed and imposed as inflow boundary condition for the stator in the second cycle. With this measure computational time was approximately halved from about a month to fourteen days. Certainly, a major drawback of this method is that interaction between rotor and stator could not be investigated in every detail. Nevertheless, with this approach a further efficiency gain of approximately 1% in the impeller and 0.2% in the stator was achieved. However, as the stator still suffers from flow separation, the optimization results are rather imprecise and the little gain of only 0.2% shows that the additional costs¹ of the simulations necessary to conduct the optimization of the diffuser are not worth the outcome. Another issue that was raised by the redesign of the stator is the part-load instability which the original pump did not feature.

Although the problems of the flow in the vaned diffuser were not eliminated completely, a rise of the peak efficiency of over 5% and an increase of the performance in part-load and overload conditions clearly prove the capabilities of the presented workflow. The combination of analytical design criteria with multi-objective optimization emerged to be the key to the improvement of the design of the *PS550* mixed-flow pump.

7.2 Further research

The difficulties in dealing with the flow separation and the occurring part-load instability have exposed the weaknesses of the workflow presented in this thesis. When dealing with measures to compensate for the part-load instability, most approaches presented in literature tackle the impeller design to positively affect rotor-stator interaction. However, analysis of the *PS550* mixed-flow pump indicated that the instability was caused by the stator itself. Therefore it seems to be worthwhile to dedicate some research effort into investigating the flow phenomena occurring in the vaned diffuser and to develop a design procedure in order to prevent the separation and the instability.

In terms of optimization it is likely that better results can be achieved if the domain is not split at the interface between the impeller and the vaned diffuser. Instead, the

¹The design point evaluations for the stator optimization took around seven days.

whole pump should be optimized in one cycle so that also the trailing edge of the rotor and the leading edge of the stator can be adjusted in the optimization process. Beyond that, the application of multi-condition optimization in which the objectives are not only to improve the efficiency in BEP but also in specified off-design points is very likely to then produce a performance curve that is stable throughout the whole operating range of the pump. This matter should therefore definitely be subject of further research. Besides, it is necessary to check the optimized design for structural integrity with regards to production and to the detection of margins for material savings. For this reason an interesting research question is, whether the integration of fluid-structure interaction in the optimization process is feasible or not.

The next step in the development process must be the execution of model tests on a laboratory test rig. They would definitely be helpful to further verify the simulation results and also to gain a more detailed insight on the actual flow behaviour and performance characteristics. It has to be checked, whether those flow phenomena, such as the separation in the vaned diffuser, which were predicted in the simulations do appear in experiments too. Furthermore, if such a model tests were conducted, it would also be possible to investigate cavitation as well as to record NPSH curves. The knowledge gained from those tests should then contribute to adapt a method in order to capture cavitation in the optimization process.

In case computational resources were unlimited (or at least not limited to what a single workstation is able to carry out) it would definitely be beneficial to examine tip clearance effects on the pump performance and it would be especially helpful to know if they showed an influence on the instability.

Bibliography

- [1] ANSI/HI 12.1-12.6, *Rotodynamic (Centrifugal) Slurry Pumps*; American National Standards Institute, Inc.: 2011.
- [2] ANSYS CFX, Theory Guide., version 18.2, ANSYS, Inc., 2018.
- [3] ANSYS CFX, Reference Guide., version 18.2, ANSYS, Inc., 2018.
- [4] ANSYS DesignXplorer, User's Guide., version 18.2, ANSYS, Inc., 2018.
- [5] ASME PTC 8.2, *Centrifugal pumps, Performance, test, codes*; The American Society of Mechanical Engineers: New York, 1991.
- [6] Bamberger, K., *Aerodynamic optimization of low-pressure axial fans*; Berichte aus der Strömungstechnik; Shaker: Aachen, 2015.
- [7] Bammert, K., and Kläukens, H. (1949). Nabentotwasser hinter Leiträdern von axialen Strömungsmaschinen. *Ingenieur-Archiv Band XVII*.
- [8] Bardina, J. E., Huang, P. G., and Coakley, T. J., *Turbulence Modeling Validation, Testing, and Development*; NASA Technical Memorandum; Ames Research Center: Moffett Field, CA, 1997.
- [9] Bing, H., Tan, L., Cao, S., and Lu, L. (2012). Prediction method of impeller performance and analysis of loss mechanism for mixed-flow pump. *Science in China Series E: Technological Sciences* 55, 1988–1998.
- [10] Bohl, W., *Strömungsmaschinen 2, Berechnung und Konstruktion*, 8. Aufl.; Kamprath-Reihe; Vogel Buchverlag: Würzburg, 2012.
- [11] Bohl, W., and Elmendorf, W., *Strömungsmaschinen 1, Aufbau und Wirkungsweise*, 11. Aufl.; Kamprath-Reihe; Vogel Buchverlag: Würzburg, 2012.
- [12] Brandt, M. J., Johnson, K. M., Elphinstion, A. J., and Ratnayaka, D. D., *Twort's Water Supply*; Elsevier: 2017.

- [13] Casey, M., Zwyssig, C., and Robinson, C., The Cordier Line for Mixed Flow Compressors. In *Proceedings of the ASME Turbo Expo 2010*; 7; ASME: New York, NY, 2010, pp 1859–1869.
- [14] Celik, I. B., Ghia, U., Roache, P. J., Freitas, C. J., Coleman, H., and Raad, P. E. (2008). Procedure for Estimation and Reporting of Uncertainty Due to Discretization in CFD Applications. *Journal of Fluids Engineering* 130, 078001/1–4.
- [15] Cordier, O. (1953). Ähnlichkeitsbedingungen für Strömungsmaschinen. *Brennstoff-Wärme-Kraft, Bd. 5, Heft 10*, 337–340.
- [16] d’Agostino, L. (2013). On the hydrodynamics of rocket propellant engine inducers and turbopumps. *IOP Conference Series: Materials Science and Engineering* 52.
- [17] de Haller, P. (1953). Das Verhalten von Tragflügelgittern in Axialverdichtern und im Windkanal. *Brennstoff-Wärme-Kraft, Bd. 5, Heft 10*, 333–337.
- [18] Dixon, S. L., and Hall, C. A., *Fluid mechanics and thermodynamics of turbomachinery*, 6th ed.; Butterworth-Heinemann/Elsevier: Burlington, MA, 2012.
- [19] Eça, L., and Hoekstra, M. (2014). A procedure for the estimation of the numerical uncertainty of CFD calculations based on grid refinement studies. *Journal of Computational Physics* 262, 104–130.
- [20] Ferziger, J. H., and Peric, M., *Numerische Strömungsmechanik*; Springer Vieweg: Berlin Heidelberg, 2008.
- [21] Future Market Insights. Centrifugal Pump Market: Global Industry Analysis, Size and Forecast, 2017 to 2027. https://www.futuremarketinsights.com/reports/centrifugal-pumps-market-102017#preview_analysis (accessed July 18, 2018).
- [22] Gadermaier, G., *CFD - Simulation von Kavitationserscheinungen in einer Radialpumpe*, Diplomarbeit; TU Wien: 2015.
- [23] GRUNDFOS A/S, *Axial and mixed flow pumps for high volume water handling*, KPL and KWM range 50Hz; GRUNDFOS Holding A/S: Bjerringbro, DK, 2016.
- [24] Gülich, J. F., *Centrifugal Pumps*, 2nd ed.; Springer-Verlag Berlin Heidelberg: Heidelberg, 2010.

- [25] Gülich, J. F., *Kreiselpumpen, Handbuch für Entwicklung, Anlagenplanung und Betrieb*, 4th ed.; Springer-Verlag Berlin Heidelberg: Heidelberg, 2013.
- [26] Hájek, J., Parameterization of Airfoils and Its Application in Aerodynamic Optimization. In *WDS'07 Proceedings of Contributed Papers, Part I*, Šafránková, J., Ed., Vyd. 1; Matfyzpress: Praha, 2007, pp 233–240.
- [27] HamiltonJet, *Which Pump - Axial or Mixed Flow?*; JetTorque, Vol. 8; HamiltonJet New Zealand: Christchurch, 1997.
- [28] Höller-Litzlhammer, S., Benigni, H., and Jaberg, H., Optimisation of a Variable Pitch Mixed Flow Diffuser Pump with Numerical Methods and Test Rig Verification. In *Conference proceedings, Conference on Modelling Fluid Flow (CMFF'15)*, Department of Fluidmechanics, Budapest University of Technology and Economics, Ed., Budapest, 2015.
- [29] IEC 60193, *Turbines hydrauliques, pompes d'accumulation et pompes-turbines – Essais de réception sur modèle*, 2nd ed., 1999.
- [30] ISO 5198, *Regeln für die Messung des hydraulischen Betriebsverhaltens Präzisionsklasse*, 1999.
- [31] ISO 9906, *Kreiselpumpen - Hydraulische Abnahmeprüfungen - Klassen 1, 2 und 3*, 2013.
- [32] Jacobsen, C. B., *The Centrifugal Pump*, Research and Technology; GRUNDFOS Management A/S: 2016.
- [33] Janiga, G., A Few Illustrative Examples of CFD-based Optimization. In *Optimization and Computational Fluid Dynamics*, Thévenin, D., and Janiga, G., Eds.; Springer: Berlin, Heidelberg, 2008, pp 17–59.
- [34] Kim, J.-H., and Kim, K.-Y. (2011). Optimization of Vane Diffuser in a Mixed-Flow Pump for High Efficiency Design. *International Journal of Fluid Machinery and Systems* 4, 172–178.
- [35] Kim, J.-H., and Kim, K.-Y. (2012). Analysis and Optimization of a Vaned Diffuser in a Mixed Flow Pump to Improve Hydrodynamic Performance. *Journal of Fluids Engineering* 134, 071104/1–10.
- [36] KSB Aktiengesellschaft, *Auslegung von Kreiselpumpen*, Technische Information, 5., überarbeitete und erweiterte Auflage; KSB Aktiengesellschaft: Frankenthal (Pfalz), 2005.

- [37] Kuhlmann, H. C., *Strömungsmechanik, Eine kompakte Einführung für Physiker und Ingenieure*, 2., aktualisierte Auflage; Pearson: Hallbergmoos, 2014.
- [38] Lieblein, S., Schwenk, F. C., and Broderick, R. L., *Diffusion Factor for estimating losses and limiting blade loadings in axial-flow-compressor blade elements*; NACA Research Memorandum; Lewis Flight Propulsion Laboratory: Cleveland, OH, 1953.
- [39] Liu, H., Chen, X., Wang, K., Tan, M., and Zhou, X. (2016). Multi-condition optimization and experimental study of impeller blades in a mixed-flow pump. *Advances in Mechanical Engineering* 8, 1–9.
- [40] Lorusso, M., Capurso, T., Torresi, M., Fortunato, B., Fornarelli, F., Camporeale, S. M., and Monteriso, R. (2017). Efficient CFD evaluation of the NPSH for centrifugal pumps. *Energy Procedia* 126, 778–785.
- [41] Manzan, M., Nobile, E., Pieri, S., and Pinto, F., Multi-objective Optimization for Problems Involving Convective Heat Transfer. In *Optimization and Computational Fluid Dynamics*, Thévenin, D., and Janiga, G., Eds.; Springer: Berlin, Heidelberg, 2008, pp 217–266.
- [42] Mcilvaine Company. Forecasts of Pump Purchases for each of the 6730 Largest Customers. <http://home.mcilvainecompany.com/index.php/component/content/article/7-news/1396-nr2421> (accessed July 18, 2018).
- [43] Menter, F. R. (1994). Two-equation eddy-viscosity turbulence models for engineering applications. *AIAA Journal* 32, 1598–1605.
- [44] Muggli, F. A., Holbein, P., and Dupont, P. (2002). CFD Calculation of a Mixed Flow Pump Characteristic From Shutoff to Maximum Flow. *Journal of Fluids Engineering* 124, 798–802.
- [45] Oxford Economics. Global Pump Market Outlook. <https://www.oxfordeconomics.com/global-pump-valves-market-forecast-reports> (accessed July 18, 2018).
- [46] Persistence Market Research. Pumps Market: Global Sales, Industry Size, Market Share, opportunities, and Key Trends by 2024. <https://www.persistencemarketresearch.com/market-research/pumps-market.asp#market-bytes> (accessed July 18, 2018).
- [47] Pfeleiderer, C., and Petermann, H., *Strömungsmaschinen*, 7., unveränd. Aufl.; Klassiker der Technik; Springer: Berlin, 2005.

- [48] RIVA Calzoni S.p.A., *Pompa Modello D550 Cilindrica 832/75, Tabella Componenti Var. 75 Lab. R.C. Banco A*, Milano, 1988.
- [49] Schobeiri, M. T., *Fluid mechanics for engineers, A graduate textbook*; Springer: Berlin and London, 2010.
- [50] Seume, J., and Mailach, R., Grundlagen der Strömungsmaschinen. In *Dubbel, Taschenbuch für den Maschinenbau*, Dubbel, H., Grote, K.-H., and Feldhusen, J., Eds., 24., aktualisierte Aufl.; Springer Vieweg: Berlin, 2014, pp 1250–1277.
- [51] Sobieczky, H., Parametric Airfoils and Wings. In *Notes on Numerical Fluid Mechanics*, Fujii, K., and Dlikravich G.S., Eds.; Vol. 68; Vieweg: 1998, pp 71–88.
- [52] Sulzer Ltd, *SJM Vertical Mixed Flow Pump*, 2015.
- [53] Sulzer Ltd, *SJT Vertical Turbine Pump*, 2015.
- [54] Sulzer Pumps, *Centrifugal Pump Handbook*; Elsevier: 2010.
- [55] Thévenin, G., Dominique; Janiga, *Optimization and Computational Fluid Dynamics*; Thévenin, D., and Janiga, G., Eds.; Springer: Berlin, Heidelberg, 2008.
- [56] Van den Braembussche, René A., Numerical Optimization for Advanced Turbomachinery Design. In *Optimization and Computational Fluid Dynamics*, Thévenin, D., and Janiga, G., Eds.; Springer: Berlin, Heidelberg, 2008, pp 147–189.
- [57] Weinig, F., *Die Strömung um die Schaufeln von Turbomaschinen: Beitrag zur Theorie axial durchströmter Turbomaschinen*; Barth: Leipzig, 1935.
- [58] Willinger, R., and Köhler, M., Influence of Blade Loading Criteria and Design Limits on the Cordier-Line for Axial Flow Fans. In *Proceedings of the ASME Turbo Expo: Turbine Technical Conference and Exposition - 2014*, Hodson, H., Ed.; ASME: New York, NY, 2014.
- [59] Wu, C.-H., *A General Theory of three-dimensional flow in Subsonic and Supersonic Turbomachines of Axial-, Radial-, and Mixed-Flow types*; NACA Technical Note; Lewis Flight Propulsion Laboratory: Cleveland, OH, 1952.
- [60] Zhang, D., Shi, W., Pan, D., and Dubuisson, M. (2015). Numerical and Experimental Investigation of Tip Leakage Vortex Cavitation Patterns and Mechanisms in an Axial Flow Pump. *Journal of Fluids Engineering* 137, 121103/1–14.

Appendix A

Tables and diagrams

A.1 Simulation setup

	Coarse	Medium	Fine
No. of nodes	218258	584685	1696288
No. of elements	203880	554520	1628400
% of mesh	52.14	51.44	49.16
Min. face angle in ° ($>15^\circ$)	24.0	24.2	24.4
Max. face angle in ° ($<165^\circ$)	156.2	156.0	155.8
Max. element volume ratio	8.981	5.878	4.413
Min. volume	$6.066 \cdot 10^{-14}$	$3.012 \cdot 10^{-14}$	$1.434 \cdot 10^{-14}$
Max. edge length ratio	5428	4554	4616
Volume in m^3	$1.867 \cdot 10^{-2}$		
Average cell height h in mm	4.507	3.229	2.255
y_{mean}^+ (area avg.)	13.9	13.1	13.2

Table A.1: Data of the (Inblock + Rotor)-mesh used for validation of the simulation

	Coarse	Medium	Fine
No. of nodes	159210	459574	1542446
No. of elements	147180	433920	1481280
% of mesh	37.64	40.25	44.72
Min. face angle in ° (>15°)	21.7	24.6	24.9
Max. face angle in ° (<165°)	159	156.0	155.2
Max. element volume ratio	9.656	4.117	2.909
Min. volume	$3.443 \cdot 10^{-13}$	$1.734 \cdot 10^{-13}$	$8.655 \cdot 10^{-14}$
Max. edge length ratio	985	508	338
Volume in m ³	$1.864 \cdot 10^{-2}$		
Average cell height h in mm	5.021	3.502	2.326
y_{mean}^+ (area avg.)	11.3	12.9	12.6

Table A.2: Data of the (Stator + Outblock)-mesh used for validation of the simulation

	Coarse	Medium	Fine
No. of nodes	15009	36452	79065
No. of elements	39939	89626	202775
% of mesh	10.21	8.31	6.12
Max. skewness (<0.9)	0.821	0.899	0.899
Min. orthogonal quality (>0.1)	0.144	0.101	0.101
Volume in m ³	$1.294 \cdot 10^{-1}$		
Average cell height h in mm	14.76	11.30	8.613
y_{mean}^+ (area avg.)	35.4	39.3	38.4

Table A.3: Data of the mesh of the outlet-elbow used for validation of the simulation

	ψ	η/η_{ref}	λ
r_{21}		1.453	
r_{32}		1.400	
R	-0.220	-0.949	0.095
p	4.413	0.148	7.066
ϕ_{ext}^{21}	0.345	0.699	$8.577 \cdot 10^{-2}$
ϕ_{ext}^{32}	0.356	1.346	$8.577 \cdot 10^{-2}$
e_a^{21} in %	1.279	1.670	0.385
e_a^{32} in %	5.733	1.731	4.071
e_{ext}^{21} in %	0.305	41.560	0.030
e_{ext}^{32} in %	1.652	25.321	0.415
GCI_{fine}^{21} in %	0.380	36.698	0.037
GCI_{fine}^{32} in %	2.100	42.384	0.521

Table A.4: Quantities calculated by the GCI method^a.

^aIn this table, ϕ_{ext}^{21} and ϕ_{ext}^{32} represent place holders for ψ , η/η_{opt} and λ , they must not be mistaken for the flow coefficient.

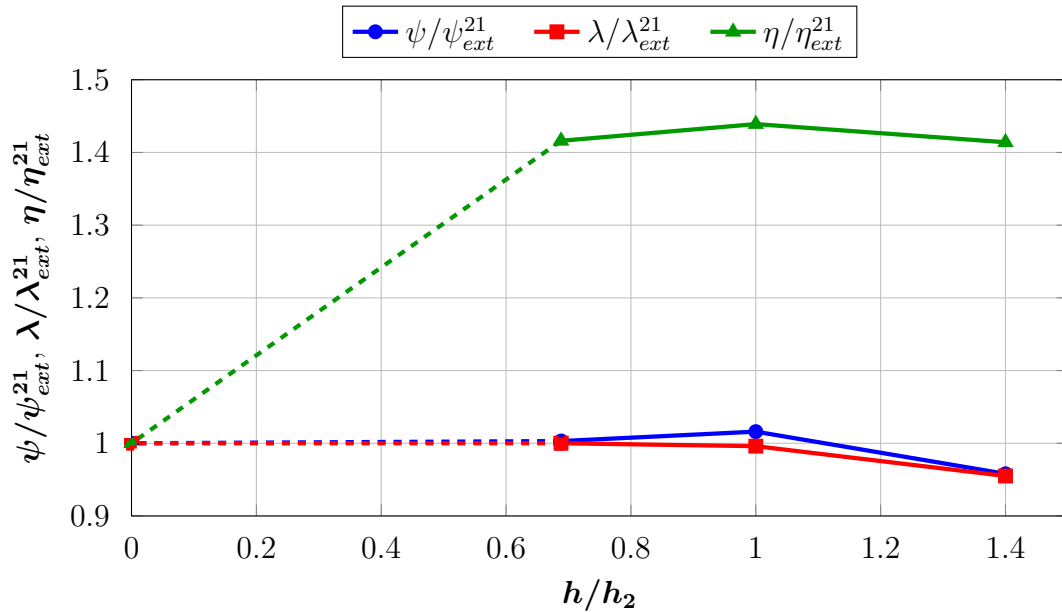


Figure A.1: Convergence plot of head coefficient, power coefficient and efficiency

A.2 Analysis of the flow in the vaned diffuser

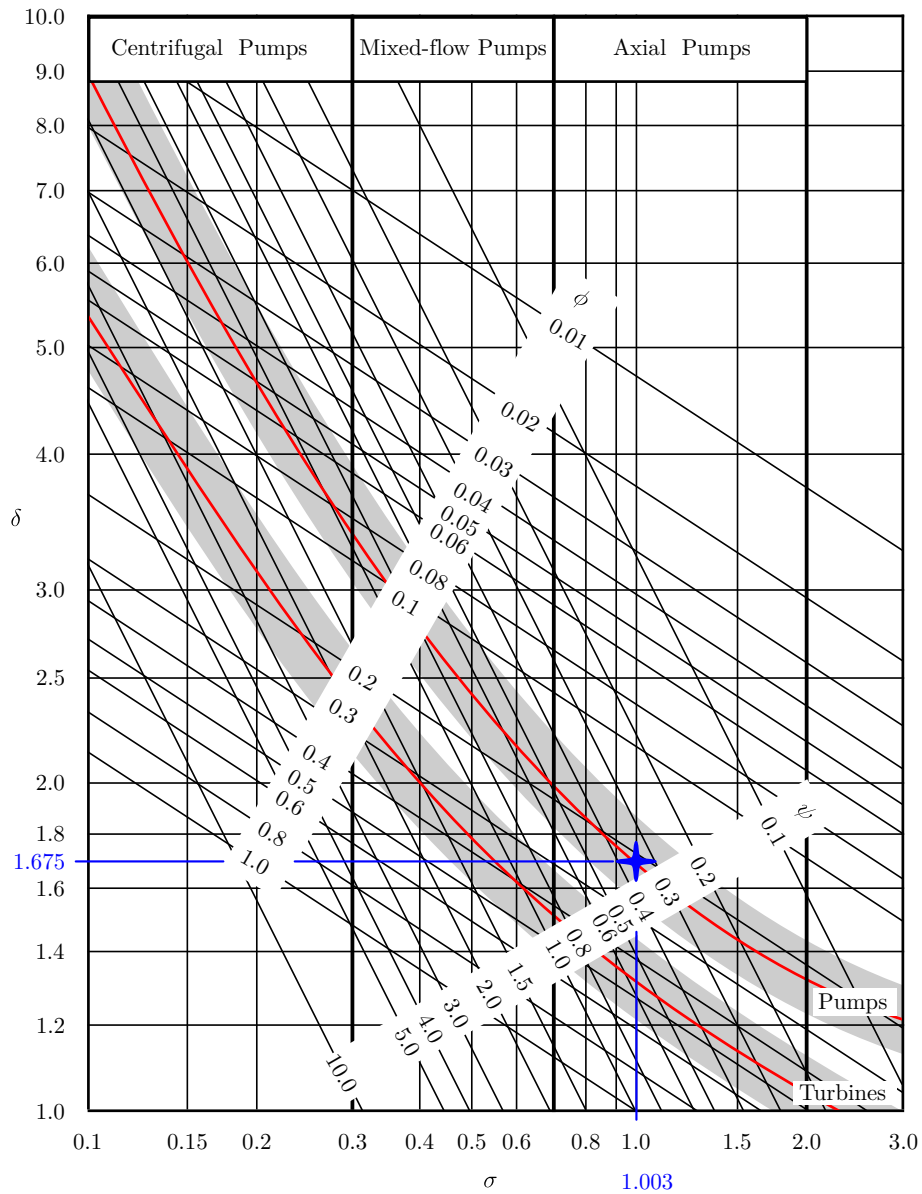


Figure A.2: Cordier diagram: blue marker denotes position of *PS550* model pump, modified from [50]

A.3 Optimization

ID	t_{LE}	t_{TE}	ER_{LE}	ER_{TE}	a)	b)	c)	d)	e)
Ref.	1.000	1.000	1.000	1.000	0.219	0.000	0.660	1.000	1.000
1	0.495	2.973	0.914	0.475	0.011	0.019	0.819	0.987	1.523
2	0.535	3.779	1.459	0.298	0.077	0.060	1.204	1.000	0.372
3	0.574	3.880	1.883	0.327	0.143	0.012	0.588	0.985	0.971
4	0.614	3.074	1.035	0.652	0.136	0.076	0.434	1.000	0.397
5	0.654	1.461	0.732	0.150	0.106	0.052	0.870	1.005	0.655
6	0.693	3.578	0.550	0.919	0.246	0.034	1.076	0.997	0.421
7	0.733	3.477	1.398	0.209	0.253	0.065	0.845	0.986	0.089
8	0.773	2.066	1.944	1.066	0.048	0.041	0.691	0.998	0.846
9	0.812	1.965	1.217	0.357	0.165	0.010	1.281	1.000	0.799
10	0.852	3.678	2.308	1.037	0.099	0.023	1.101	1.002	0.699
11	0.891	4.585	1.520	1.096	0.172	0.063	0.716	1.000	0.253
12	0.931	1.260	1.580	0.771	0.224	0.067	0.922	0.995	0.183
13	0.971	1.864	0.186	0.978	0.121	0.032	0.614	1.010	1.095
14	1.010	4.485	0.610	0.859	0.084	0.008	0.639	1.007	1.147
15	1.050	2.167	1.762	0.889	0.238	0.005	0.665	0.998	0.672
16	1.090	2.771	0.671	0.682	0.026	0.071	1.153	1.009	0.629
17	1.129	2.469	0.974	1.125	0.092	0.016	1.255	1.010	1.002
18	1.169	4.686	2.005	0.446	0.216	0.030	1.229	0.996	0.236
19	1.208	1.562	1.641	0.120	0.180	0.027	0.537	1.005	0.706
20	1.248	4.081	0.247	0.386	0.128	0.025	1.306	1.007	0.815
21	1.288	4.384	0.429	0.268	0.194	0.036	0.511	1.004	0.696
22	1.327	1.360	2.186	0.416	0.062	0.043	1.127	1.009	0.688
23	1.367	4.787	1.095	0.830	0.004	0.056	0.768	1.008	0.591
24	1.406	3.981	2.247	0.179	0.040	0.047	0.896	1.009	0.558
25	1.446	3.275	0.792	0.239	0.018	0.054	0.460	1.008	0.962
26	1.486	2.267	0.368	0.534	0.260	0.014	0.742	1.001	0.691

ID	t_{LE}	t_{TE}	ER_{LE}	ER_{TE}	a)	b)	c)	d)	e)
27	1.525	2.671	1.823	0.623	0.055	0.001	0.563	1.005	1.224
28	1.565	3.174	0.307	0.564	0.209	0.074	1.050	0.986	0.018
29	1.605	3.376	2.126	0.741	0.202	0.038	0.409	1.004	0.461
30	1.644	4.182	1.701	0.505	0.187	0.078	0.793	0.989	0.000
31	1.684	1.663	0.853	0.800	0.114	0.069	0.486	1.007	0.464
32	1.723	2.368	1.277	1.007	0.231	0.049	1.178	0.991	0.003
33	1.763	1.764	0.489	0.593	0.033	0.021	0.973	1.012	1.243
34	1.803	2.872	2.065	0.948	0.070	0.058	1.024	1.007	0.319
35	1.842	4.283	1.338	0.712	0.158	0.003	0.947	1.006	0.612
36	1.882	2.570	1.156	0.091	0.150	0.045	0.999	1.003	0.216
37	0.475	1.388	0.156	0.207	0.000	0.000	0.823	1.002	0.891
38	0.475	1.506	0.156	0.162	0.000	0.000	0.821	1.001	0.871
39	0.475	4.837	2.338	0.076	0.213	0.000	0.396	0.983	1.158
40	1.902	4.837	0.156	1.140	0.264	0.079	1.319	0.945	0.141
41	1.902	4.837	0.156	1.140	0.264	0.079	0.396	0.979	0.228
42	0.475	1.209	2.338	0.076	0.015	0.079	1.319	0.995	0.472
43	1.902	4.837	2.338	1.140	0.264	0.000	1.319	0.992	0.150
44	1.902	1.209	0.156	1.140	0.264	0.079	1.319	0.965	0.202
45	1.685	1.209	0.181	0.133	0.015	0.001	0.396	1.009	1.971
46	1.314	1.230	0.275	1.127	0.063	0.062	0.700	1.010	0.903
47	1.397	1.231	1.405	1.123	0.110	0.052	1.209	1.007	0.393

Table A.5: Design points and objectives for the rotor optimization cycle - the optimal configuration is marked in red: t_{LE} , t_{TE} , ER_{LE} , ER_{TE} are scaled in relation to the corresponding quantity of the reference configuration; a) = $z_{LE,h}/d_{2o}$, b) = $z_{LE,s}/d_{2o}$, c) = r_{LE}/d_{2o} , d) = $\eta_R/\eta_{R,Ref,Sim}$, e) = $A_{Cav}/A_{Cav,Ref,Sim}$

ID	$\alpha_{4B, i}$	$\alpha_{4B, m}$	$\alpha_{4B, o}$	$z_{TE, h}$	$z_{TE, s}$	ω_{Stator}	α_{mcs}	a)
Ref.	1.000	1.000	1.000	1.000	1.000	0.236	0.696	1.000
1	1.147	1.079	1.075	2.159	1.344	0.106	0.846	0.252
2	1.141	1.040	1.127	2.357	1.455	0.106	0.846	0.463
3	1.134	1.104	1.088	2.177	1.639	0.096	0.856	0.149
4	1.128	1.085	1.030	1.980	1.541	0.110	0.794	0.119
5	1.121	1.027	1.049	2.375	1.578	0.100	0.813	0.240
6	1.115	1.117	1.004	2.249	1.479	0.095	0.843	0.156
7	1.109	0.989	1.062	2.052	1.529	0.120	0.782	0.592
8	1.102	1.137	1.101	2.392	1.492	0.078	0.894	0.387
9	1.096	1.156	1.114	2.124	1.381	0.090	0.897	0.122
10	1.089	1.072	1.140	1.944	1.467	0.109	0.805	0.253
11	1.083	1.021	0.997	2.303	1.430	0.105	0.801	0.183
12	1.077	1.001	1.166	2.195	1.553	0.114	0.818	0.548
13	1.070	1.047	1.147	2.267	1.332	0.066	0.862	0.128
14	1.064	1.130	1.160	2.106	1.590	0.070	0.885	0.281
15	1.057	1.014	1.082	1.998	1.357	0.107	0.780	0.413
16	1.051	1.098	1.017	2.016	1.369	0.099	0.842	0.052
17	1.045	1.034	1.121	2.034	1.651	0.118	0.788	0.377
18	1.038	1.143	1.036	2.088	1.614	0.094	0.870	0.180
19	1.032	1.066	1.134	2.410	1.516	0.081	0.825	0.203
20	1.026	0.995	1.043	2.231	1.602	0.101	0.770	0.102
21	1.019	1.111	1.069	2.339	1.627	0.075	0.864	0.375
22	1.006	1.150	1.108	2.213	1.418	0.075	0.895	0.181
23	1.000	1.008	1.056	2.285	1.406	0.077	0.792	0.085
24	0.994	1.059	1.010	2.070	1.565	0.102	0.820	0.066
25	0.987	1.053	1.153	2.142	1.443	0.066	0.862	0.103
26	0.981	1.092	1.095	1.962	1.504	0.085	0.822	0.200
27	1.020	1.045	1.170	2.224	1.358	0.068	0.854	0.269
28	1.015	1.159	1.170	2.405	1.326	0.074	0.906	0.218

ID	$\alpha_{4B, i}$	$\alpha_{4B, m}$	$\alpha_{4B, o}$	$z_{TE, h}$	$z_{TE, s}$	ω_{Stator}	α_{mcs}	a)
29	1.143	1.046	1.147	2.029	1.657	0.100	0.849	0.399
30	1.064	1.091	1.170	2.266	1.326	0.068	0.891	0.203
31	1.061	0.985	1.170	2.196	1.458	0.112	0.795	0.879
32	1.125	0.992	0.994	2.343	1.657	0.104	0.780	0.329
33	1.069	1.054	1.068	2.324	1.326	0.079	0.837	0.097
34	1.029	1.159	1.170	2.310	1.326	0.061	0.935	0.107
35	1.035	1.159	1.170	2.181	1.326	0.069	0.913	0.044
36	1.035	1.159	1.135	2.137	1.326	0.074	0.902	0.283
37	0.995	1.159	1.146	2.137	1.326	0.076	0.894	0.088
38	0.999	1.095	1.148	2.219	1.340	0.064	0.873	0.190
39	1.026	1.133	1.166	2.283	1.409	0.070	0.886	0.189
40	0.998	1.094	1.149	2.285	1.405	0.063	0.881	0.117

Table A.6: Design points and objectives for the stator optimization cycle - the optimal configuration is marked in red: $\alpha_{4B, i}$, $\alpha_{4B, m}$, $\alpha_{4B, o}$, $z_{TE, h}$ and $z_{TE, s}$ are scaled in relation to the corresponding quantity of the reference configuration; α_{mcs} is normalized so that swirl-free flow ($\alpha = 90^\circ$) corresponds to 1; a) = Normalized area of isosurfaces with low axial velocity (blockage area) $A_{Sep}/A_{Sep, Ref, Sim}$